Université de Montréal

Nanopatterning and Functionalization of Phospholipid-Based Langmuir-Blodgett and Langmuir-Schaefer Films

par
Nathalie Y-Wa Tang

Département de Chimie
Faculté des Arts et des Sciences

Thèse présentée à la Faculté des Études Supérieures
en vue de l'obtention du grade de Philosophiae Doctor (Ph.D.)
en Chimie

Août, 2010

Université de Montréal
Faculté des études supérieures et postdoctorales

Cette thèse intitulée:

Nanopatterning and Functionalization of Phospholipid-Based Langmuir-Blodgett and Langmuir-Schaefer Films

Présentée par :
Nathalie Y-Wa Tang

a été évaluée par un jury composé des personnes suivantes :

Pr. G. Bazuin, président-rapporteur (Université de Montréal)

Pr. A. Badia, directeur de recherche (Université de Montréal)

Pr. M. Lafleur, membre du jury (Université de Montréal)

Pr. C. DeWolf, examinateur externe (Concordia University)

Pr. G. Bazuin, représentant du doyen de la FES (Université de Montréal)

Résumé

Durant les dernières décennies, la technique Langmuir-Blodgett (LB) s'est beaucoup développée dans l'approche « *bottom-up* » pour la création de couches ultra minces nanostructurées. Des patrons constitués de stries parallèles d'environ 100 à 200 nm de largeur ont été générés avec la technique de déposition LB de monocouches mixtes de 1,2-dilauroyl-*sn*-glycéro-3-phosphatidylcholine (DLPC) et de 1,2-dipalmitoyl-*sn*-glycéro-3-phosphatidylcholine (DPPC) sur des substrats de silicium et de mica. Afin d'amplifier la fonctionnalité de ces patrons, la 1-palmitoyl-2-(16-(*S*-methyldithio)hexadécanoyl)-*sn*-glycéro-3-phosphatidylcholine (DSDPPC) et la 1-lauroyl-2-(12-(*S*-methyldithio)dodédecanoyl)-*sn*-glycéro-3-phosphatidylcholine (DSDLPC) ont été employées pour la préparation de monocouches chimiquement hétérogènes. Ces analogues de phospholipide possèdent un groupement fonctionnel méthyldisulfide qui est attaché à la fin de l'une des chaînes alkyles. Une étude exhaustive sur la structure de la phase des monocouches Langmuir, Langmuir-Schaefer (LS) et LB de la DSDPPC et de la DSDLPC et leurs différents mélanges avec la DPPC ou la DLPC est présentée dans cette thèse.

Tout d'abord, un contrôle limité de la périodicité et de la taille des motifs des stries parallèles de DPPC/DLPC a été obtenu en variant la composition lipidique, la pression de surface et la vitesse de déposition. Dans un mélange binaire de fraction molaire plus grande de lipide condensé que de lipide étendu, une vitesse de déposition plus lente et une plus basse pression de surface ont généré des stries plus continues et larges. L'addition d'un tensioactif, le cholestérol, au mélange binaire équimolaire de la DPPC/DLPC a permis la formation de stries parallèles à de plus hautes pressions de surface.

La caractérisation des propriétés physiques des analogues de phospholipides a été nécessaire. La température de transition de phase de la DSDPPC de 44.5 ± 1.5 °C comparativement à 41.5 ± 0.3 °C pour la DPPC. L'isotherme de la DSDPPC est semblable à celui de la DPPC. La monocouche subit une transition de phase liquide-étendue-à-condensée (LE-C) à une pression de surface légèrement supérieure à celle de la DPPC (6 mN m^{-1} vs. 4 mN m^{-1}) Tout comme la DLPC, la DSDLPC demeure dans la phase LE

jusqu'à la rupture de la monocouche. Ces analogues de phospholipide existent dans un état plus étendu tout au long de la compression de la monocouche et montrent des pressions de surface de rupture plus basses que les phospholipides non-modifiés.

La morphologie des domaines de monocouches Langmuir de la DPPC et de la DSDPPC à l'interface eau/air a été comparée par la microscopie à angle de Brewster (BAM). La DPPC forme une monocouche homogène à une pression de surface (π) > 10 mN/m, alors que des domaines en forme de fleurs sont formés dans la monocouche de DSDPPC jusqu'à une $\pi \sim 30$ mN m^{-1}.

La caractérisation de monocouches sur substrat solide a permis de démontrer que le patron de stries parallèles préalablement obtenu avec la DPPC/DLPC était reproduit en utilisant des mélanges de la DSDPPC/DLPC ou de la DPPC/DSDLPC donnant ainsi lieu à des patrons chimiquement hétérogènes. En général, pour obtenir le même état de phase que la DPPC, la monocouche de DSDPPC doit être comprimée à de plus hautes pressions de surface.

Le groupement disulfide de ces analogues de phospholipide a été exploité, afin de (i) former des monocouches auto-assemblées sur l'or et de (ii) démontrer la métallisation sélective des terminaisons fonctionnalisées des stries. La spectrométrie de photoélectrons induits par rayons X (XPS) a confirmé que la monocouche modifiée réagit avec la vapeur d'or pour former des thiolates d'or. L'adsorption de l'Au, de l'Ag et du Cu thermiquement évaporé démontre une adsorption préférentielle de la vapeur de métal sur la phase fonctionnalisée de disulfide seulement à des recouvrements sub-monocouche.

Mots-clés : DPPC, DLPC, 1-palmitoyl-2-(16-(*S*-methyldithio)hexadecanoyl)-*sn*-glycero-3-phosphocholine, 1-lauroyl-2-(12-(*S*-methyldithio)dodecanoyl)-*sn*-glycero-3-phosphocholine, séparation de phase, Langmir-Blodgett, Langmuir-Schaefer, patronage de surface, thiolate d'or, metallisation sélective

Abstract

In the past two decades, the Langmuir-Blodgett (LB) technique has emerged as a bottom-up route to create nanostructured ultrathin films. Patterns consisting of parallel stripes, ~100 to 200 nm in width, were generated via the LB deposition of mixed monolayers of 1,2-dilauroyl-*sn*-glycero-3-phosphocholine (DLPC), and 1,2-dipalmitoyl-*sn*-glycero-3-phosphocholine (DPPC) onto silicon and mica substrates. To expand the functionality of these patterns, 1-palmitoyl-2-(16-(*S*-methyldithio)hexadecanoyl)-*sn*-glycero-3-phosphocholine (DSDPPC) and 1-lauroyl-2-(12-(*S*-methyldithio)dodecanoyl)-*sn*-glycero-3-phosphocholine (DSDLPC) were used to prepare chemically heterogeneous films. These phospholipid analogues have a methyldisulfide group attached to one of the alkyl chain ends. An extensive study of the phase structure of Langmuir, Langmuir-Shaefer and LB films of DSDPPC and DSDLPC and their mixtures with DPPC or DLPC is presented in this thesis.

Limited control over the regularity and feature size of the DPPC/DLPC stripe pattern was achieved by varying the lipid composition, deposition pressure, and substrate withdrawal speed. A higher percentage of condensed versus fluid lipid, slower deposition speed, and lower surface pressure create more continuous and wider stripes. The addition of a lineactant, cholesterol, to the DPPC/DLPC 1:1 (mol/mol) mixture allowed the formation of parallel stripes at higher surface pressure.

The gel-to-liquid crystalline transition temperature of DSDPPC was determined to be 44.5 ± 1.5 °C versus 41.5 ± 0.3 °C for DPPC by DSC and turbidity measurements. The pressure-area isotherm of DSDPPC is similar to that of DPPC. The monolayer undergoes a liquid expanded-to-condensed (LE-C) phase transition at a surface pressure slightly higher than that of DPPC (6 mN m^{-1} vs. 4 mN m^{-1}). Like DLPC, DSDLPC remains in the LE phase until the film collapse. The disulfide-modified lipids exist in a more expanded state throughout the monolayer compression and exhibit lower collapse pressures than the unmodified phospholipids.

The domain morphologies of DPPC and DSDPPC at the air/water interface were compared using Brewster Angle Microscopy. DPPC forms a homogeneous monolayer at a surface pressure (π) > 10 mN m^{-1}, while flower-like domains exist in the DSDPPC monolayers until $\pi \sim 30$ mN m^{-1}. Solid-supported DSDPPC films were prepared and characterized using various surface analysis techniques. The parallel stripe pattern previously obtained with mixtures of DPPC/DLPC was reproduced using DSDPPC/DLPC or DPPC/DSDLPC mixtures resulting in chemically-differentiated patterns. The average stripe width varied from 150 to 500 nm, depending on the lipid composition and deposition pressure.

The disulfide group of the analogues was exploited to (i) form self-assembled monolayers of phospholipids on gold and (ii) demonstrate the selective metallization of the disulfide-terminated areas of the stripe patterns. X-ray photoelectron spectroscopy (XPS) confirmed that the monolayer-bound disulfides react with Au vapor to form a gold-thiolate species. Thermally evaporated Au, Ag and Cu exhibit preferential absorption onto the modified lipids only at submonolayer coverages.

Keywords: DPPC, DLPC, 1-palmitoyl-2-(16-(*S*-methyldithio)hexadecanoyl)-*sn*-glycero-3-phosphocholine, 1-lauroyl-2-(12-(*S*-methyldithio)dodecanoyl)-*sn*-glycero-3-phosphocholine, phase separation, Langmir-Blodgett, Langmuir-Schaefer, surface patterning, gold-thiolates, selective metallization

List of Used Symbols and Abbreviations

A_{lim}	Limiting area
A_{onset}	Onset area
AFM	Atomic force microscopy
ATR-IR	Attenuated total reflection infrared spectroscopy
BAM	Brewster angle microscopy
BE	Binding energy
C	Condensed
CVD	Chemical vapor deposition
$d_{LB\ film}$	Film thickness
DCC	*N,N'*-Dicyclohexyl carbodiimide
L-α-DLPC	1,2-Dilauroyl-*sn*-glycero-3-phosphocholine
DMAP	4-Dimethylaminopyridine
L-α-DPPC	1,2-Dipalmitoyl-*sn*-glycero-3-phosphocholine
DSC	Differential scanning calorimetry
DSDLPC	1-Lauroyl-2-(12-(S-methyldithio)dodeanoyl)-*sn*-glycero-3-phosphocholine
DSDPPC	1-Palmitoyl-2-(16-(*S*-methyldithio)hexadecanoyl)-*sn*-glycero-3-phosphocholine
DSPC	1,2-Distearoyl-*sn*- glycero-3-phosphocholine
EUVL	Extreme ultraviolet lithography
FEGSEM	Field emission gun scanning electron microscopy
GIXRD	Grazing incidence X-ray diffraction
ΔH	Enthalpy of transition
Δh	Step height difference
l_{lipid}	Molecular length of phospholipid
L_α	Liquid crystalline phase
L_β	Lamellar gel
LB	Langmuir-Blodgett

LE	Liquid-expanded
LHGPC	1-Lauroyl-2-hydroxy-*sn*-glycero-3-phosphocholine
LS	Langmuir-Schaefer
LUV	Large unilamellar vesicle
μCP	Microcontact printing
Δm	Resolved mass difference
m	Target ion mass
ML	Monolayer
MLVs	Multilamellar vesicles
NIL	Nanoimprint lithography
OMCVD	Organometallic chemical vapor deposition
π	Surface pressure
π-A	Surface pressure-area
P_β	Ripple phase
PDMS	Polydimethylsiloxane
PHGPC	1-Palmitoyl-2-hydroxy-*sn*-glycro-3-phosphocholine
PMMA	Poly(methylmethacrylate)
PS	Polystyrene
P2VP	Poly(2-vinylpyridine)
PVD	Physical vapor deposition
R	Mass resolution
RSH	*n*-Alkylthiols
RSSR	*n*-Alkyldisulfides
SAMs	Self-assembled monolayers
SEM	Scanning electron microscopy
τ	Turbidity
T_m	Main phase transition temperature
T_p	Pre-transition temperature
TEM	Transmission electron microscopy
TOF-SIMS	Time of flight secondary ion mass spectroscopy

ν_{as}	Antisymmetric stretching frequency
ν_{s}	Symmetric stretching frequency
χ_{chol}	Molar fraction of cholesterol
χ_{DPPC}	Molar fraction of DPPC
XPS	X-ray photoelectron spectroscopy

Table of Content

List of Tables

List of Figures

List of Schemes

Acknowledgments

First, I would like to say thank you to Antonella Badia, my thesis supervisor, for her mentoring, her passion and her encouragement that helped me bring my work to completion. I truly feel honored to have been a member of her group where I have met incredible people, my lab mates, who have been like a second family to me. Thank you for your everyday continued support.

I would like to acknowledge the Fonds québécois de la recherche sur la nature et les technologies for a doctoral research scholoarship and the Faculté des études supérieures et postdoctorales de l'Université de Montréal, for an accelerated transfer from M.Sc to Ph.D scholarship and an end of doctoral studies scholarhip.

My special thanks to the individuals in the department of Chemistry and affiliated institutions, who have provided me with their expertise throughout my research. Not to be forgotten, I must thank the computer technicians, the glass blower and the machine shop wizards who have " saved the day" on countless occasions!

A very special thank you to Dr. Violeta Toader who synthesized the functionalized lipids, to Line Mongeon for the FEGSEM imaging, to Suzie Pouling for the XPS and TOF-SIMS analysis, and to the members of Prof. Lafleur's groups for their help with DSC and UV-Vis measurements.

To Mohini, Eric, and Jackie, I would like to send my sincerest gratitude for their precious help during the final days before my submission. Thank you to my friends who have always been there for me, who have always been willing to help, especially near the end of my research. Your moral support and your encouragements have been limitless.

Lastly, I would like to say thank you to my family, my mom and dad, my brother Fred, my best friend Yannie, and my husband Vissal. You have pushed me to go further and to never give up. You were there every step of the way. I thank you for your patience, your understanding, and your unconditional love. You have given me the strength I needed to complete this thesis.

Chapter 1 General Introduction

1.1 Research Overview

The focus of this thesis is the use of both natural and ω-modified lipids to modify and pattern surfaces. Lipids are an ideal choice of molecules to use because they are biocompatible. Thin film patterns of phospholipids with nanoscale features can be generated from binary mixtures based on phase separation and the Langmuir-Blodgett (LB) film deposition technique. The main goal of this work is to use modified lipids to generate these patterns. To this end, the phase properties in vesicles and in Langmuir films of modified lipids are compared to the unmodified lipids, and the optimal conditions to obtain these patterns are investigated. In the general introduction, the role of lipids in membranes and the structures they can form is presented. To motivate our choice of methyldisulfide group tag on the modified lipid, an introduction to gold-thiolate bonds is given. The last section is an overview of current top-down and bottom-up patterning methods, with a focus on the LB technique.

1.2 Phospholipids and Langmuir Monolayers

Lipids are versatile molecules used in various applications from the basic understanding of lipid-lipid interactions in membranes to biosensors. Enduring efforts in lipid research stem from the fact that lipids are the core component of all biological membranes. Membranes are complex structures composed of a lipid bilayer embedded with a variety of biomolecules and represent one of the most outstanding examples of Nature's self-assembled structures. Many key biochemical processes occur at the surface of biomembranes, such as cell signalling, endocytosis, molecular recognition, ion transport, charge transfer reactions, etc. Membranes also act as permeable barriers between the interior cell content and the outside environment. A schematic representation of a plasma membrane is shown in Figure 1.1.

Lipids are naturally occurring small amphiphilic molecules with a hydrocarbon moiety at one end and a polar group at the other end. Lipids can self-organize into micellar rods, micelles, bilayers, and vesicles (Figure 1.2A-D) in aqueous media, into other structures such as inverted aggregates in non-polar solvents (Figure 1.2E), and as monolayers at the air/water (A/W) interface (Figure 1.2F).

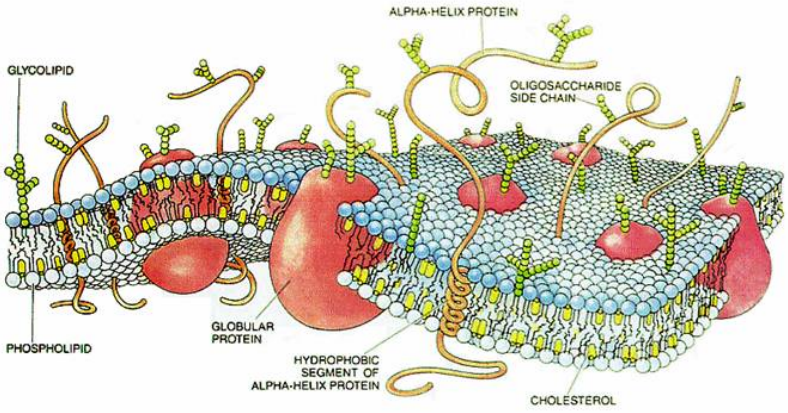

Figure 1.1 Schematic representation of a plasma membrane (reproduced from ref. 1).

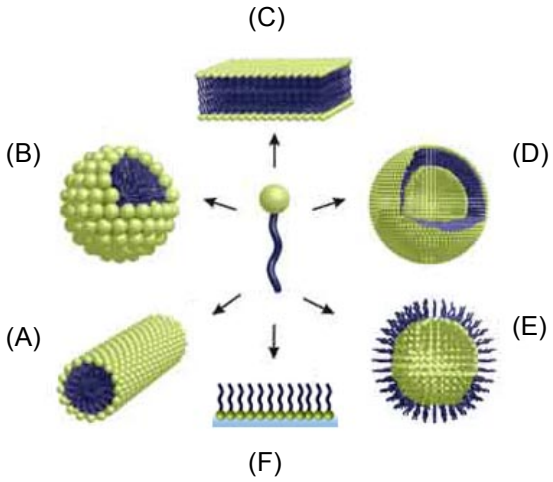

Figure 1.2 Lipid self-assembled structures (A) micellar rods, (B) micelles, (C) bilayers, (D) vesicles, (E) inverted aggregates, and (F) monolayers (inspired from ref. 2).

Lipids are divided into subcategories such as fatty acids, glycerolipids, phospholipids, sphingolipids, sterol lipids, and more. Researchers seek to better understand the structure of biological membranes and biomembrane processes by studying lipid-lipid and lipid-protein interactions in model lipid monolayers and bilayers. Monolayers can easily be studied using the Langmuir film technique.[3] A lipid molecule has a hydrophilic headgroup and a hydrophobic tail, hence the only possible orientation it can adopt at the A/W interface is the one where the polar (hydrophilic) head is in the water and the hydrophobic portion extends preferably away from the water surface (Figure 1.3A). In the Langmuir film technique, lipid molecules are spread at the A/W interface from solvent. After the solvent evaporates, the lipids are compressed by laterally moving barriers while the surface pressure is monitored with a Wilhelmy plate. A two-dimensional phase diagram surface pressure/area isotherm (π-A) is generated. The lipid monolayer can undergo several phase transitions as it is compressed. A typical phospholipid isotherm is shown in Figure 1.3B. The molecules are first found in a gas-analogous (G) state in which the molecules are far apart and do not interact with each other. As the monolayer is compressed and the lipid molecules begin to interact with each other, the surface pressure starts to rise. This first inflection point is termed the onset molecular area (A_{onset}), which is the area occupied by each molecule before they start influencing each other. The monolayer is then in a liquid-expanded (LE) state. Upon further compression, the monolayer enters a region of condensed/liquid coexistence. At this transition, the hydrocarbon chains begin to order themselves and the lipid molecules form solid-like condensed domains that are dispersed into a matrix of liquid-expanded molecules. The LE-C (liquid-expanded to condensed) phase transition depends on temperature and pressure. Further compression results in the complete condensation of the monolayer into a condensed (C) phase so that its compressibility is now low. There is a steep rise in the surface pressure as the molecular area is decreased. Some systems can undergo another phase transition at high surface pressure where the tilted hydrocarbon chains untilt. As the film is compressed even further, it eventually collapses.

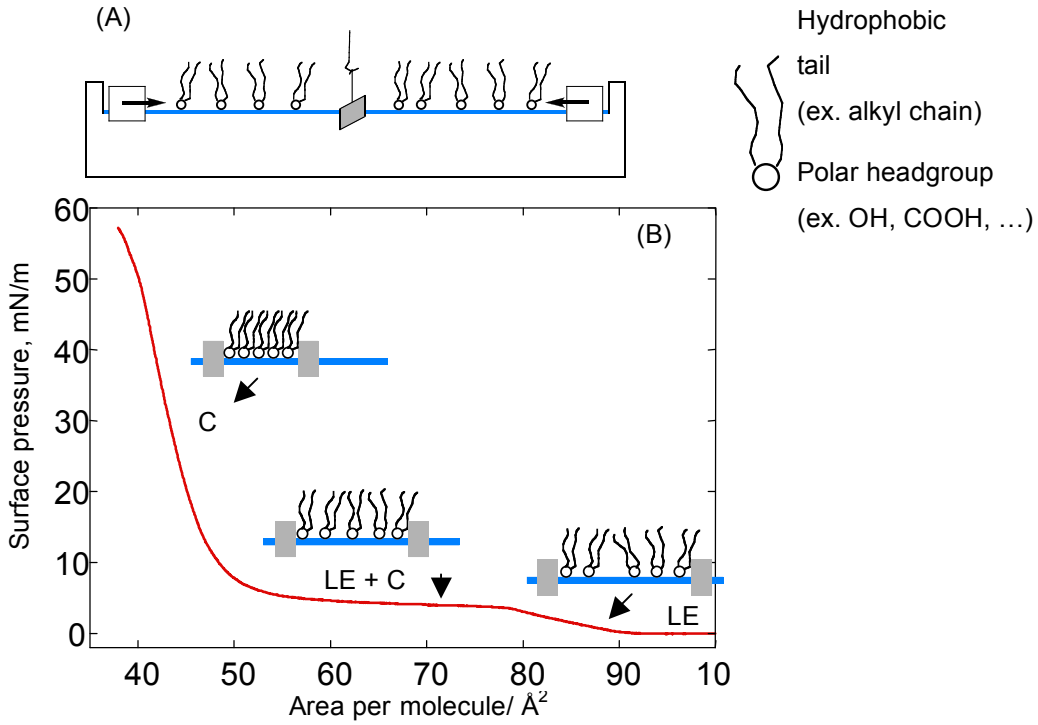

Figure 1.3 (A) Arrangement of amphiphilic molecules at the A/W interface and (B) an example of a surface pressure-area (π-*A*) isotherm illustrating the phase states of the film.

The molecular structure of these monolayer films at the A/W interface can be studied by Brewster angle microscopy (BAM),[4-6] grazing incidence X-ray diffraction (GIXD),[7,8] infrared reflection spectroscopy,[9] synchrotron X-ray diffraction[10] and fluorescence microscopy[10-12] (which requires doping of the monolayer with a fluorescent probe).

1.3 Pattern Formation at the Air/Water Interface

Patterns form in the monolayer at phase the coexistence region. These lateral structures mainly arise from a competition two forces: line tension between lipid domains

and the surrounding liquid phase and electrostatic interactions of the molecules within domains.[13-17] Electrostatic interactions favour elongated or dendritic shapes, while line tension promotes circular domains. Spherical, stripe, dendritic and spiral condensed domains of lipid have been characterized by BAM and fluorescence microscopy (Figure 1.4).

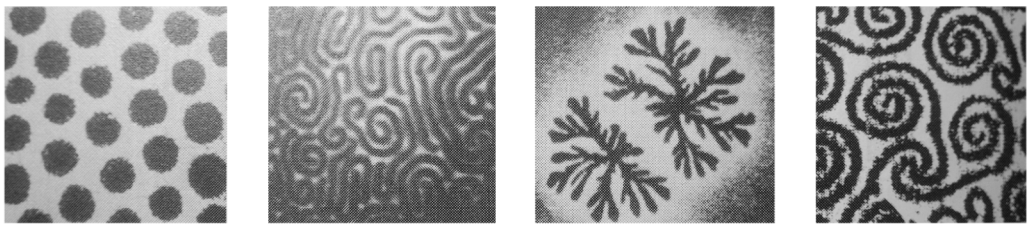

Figure 1.4 Examples of lateral structures in phase-separated lipid monolayers (image reproduced from ref. 18).

Chirality also plays a role in the shape of the condensed domains formed. One enantiomer will confer a certain handedness to the domains, while the other forms domains of the opposite handedness. Nandi *et al.* observed handedness in the dipalmitoylphosphatidylcholine domains of pure L or D enantiomers, and when mixed together, the chirality is lost and rod-like domains are seen (Figure 1.5).[19] McConnell[14] proposes that long-range dipolar forces combined with intermolecular chiral forces determine the domain shapes of chiral lipids.

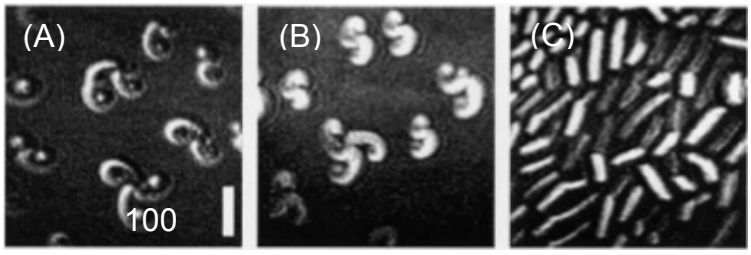

Figure 1.5 Brewster angle microscopy (BAM) images of (A) D, (B), L, and (C) racemic mixture of dipalmitoylphosphatidylcholine condensed phase domains (image reproduced from ref. 19).

The phospholipids mainly used in this work are 1,2-dilauroyl-*sn*-glycero-3-phosphocholine (DLPC), and 1,2-dipalmitoyl-*sn*-glycero-3-phosphocholine (DPPC) (Figure 1.6). The naturally occurring L enantiomer of each lipid was used. They have two long saturated aliphatic chains with a zwitterionic phosphocholine headgroup and they only differ in the number of carbons in their alkyl chains. Their respective gel-to-liquid crystalline phase transition temperatures (T_m) are -1 and 41 °C.[20] At room temperature, DPPC exists in a gel phase while DLPC exists in a fluid phase. When mixed together to form giant unilamellar vesicles or Langmuir monolayer films, their different physical states cause them to phase separate due to a chain mismatch, with DPPC forming solid-like condensed domains dispersed in a fluid matrix of DLPC.[21-23] Aqueous multilamellar dispersions of DPPC/DLPC exhibit a region of solid/fluid phase coexistence between DPPC mole factions (χ_{DPPC}) of ~0.25 and ~0.80 at T = 20°C.[20] Saturated chain phospholipids were chosen over unsaturated ones to prevent the formation of oxidized products at the A/W interface.[24-27]

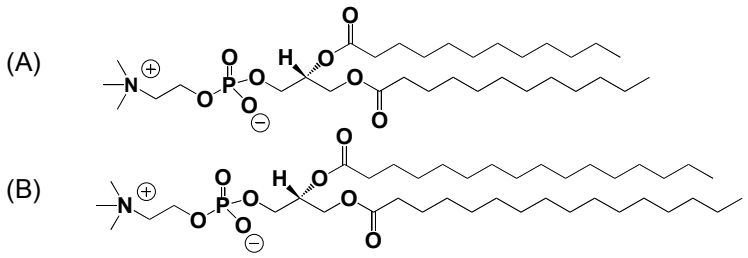

Figure 1.6 Chemical structures of (A) DLPC, and (B) DPPC.

1.4 The Langmuir-Blodgett and Langmuir Schaefer Technique

Langmuir monolayers can be transferred from the A/W interface onto a solid substrate by the Langmuir-Blodgett (LB) or Langmuir-Schaefer (LS) deposition techniques (Figure 1.7). LB film deposition involves raising or lowering a substrate vertically through the floating monolayer. LS film deposition involves pushing a substrate positioned horizontally and parallel to the A/W interface through the film. This latter approach exerts less disruptive forces on the monolayer than the LB method.

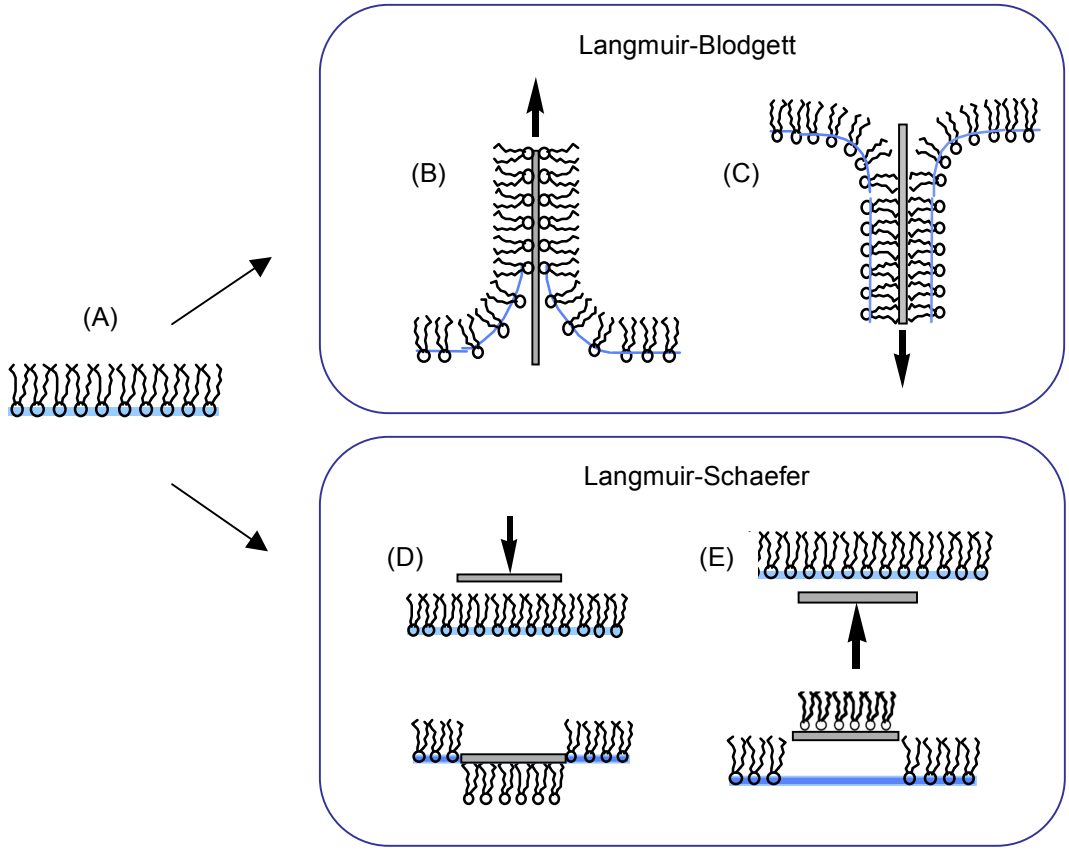

Figure 1.7 Schematic illustration of (A) a monolayer film at the A/W interface, and film transfer onto a substrate by (B) LB upward deposition, (C) LB downward deposition, (D) LS deposition with substrate above the interface, and (E) LS deposition with substrate under the A/W interface.

The Langmuir film technique was first developed to study insoluble monomolecular films at the A/W interface,[3] but more recently, the LB technique has been used to create nanopatterns. The LB technique offers many advantages for film preparation and for micro- and nanofabrication: it enables the deposition of amphiphilic materials over macroscopic substrate areas (typically several square centimeters), precise control of the deposited film thickness and molecular density, the build-up of multilayer structures with varying layer composition and the deposition of a large variety of surfactants on different kinds of solid

substrates, including curved surfaces.[28] The LB technique is also a unique tool to prepare thin films with optical, electronic, and magnetic properties. One of the latest applications of LB films is found in surface patterning. The topologically or chemically structured mesopatterns generated by the lateral phase separation of molecules can be used as etch masks and templates for area-selective deposition of biomolecules or nanoparticle (further discussed in section 1.7). Many techniques are suitable for the characterization LB or LS films on solid support, such as atomic force microscopy (AFM), scanning electron microscopy (SEM), transmission eletronic microscopy (TEM), ellipsometry, time-of-flight secondary ion mass spectrometry (TOF-SIMS), X-ray photoelectron spectroscopy (XPS), infrared reflection spectroscopy, Raman, ultra-violet and visible spectroscopy (UV-Vis), GIXD, and contact angle measurements.

LB and LS films find uses in many fields of research. In the life sciences, the interfacial properties of enzymes, viruses and proteins as well as their interactions with lipid membranes can be studied.[29] Biomolecules can be immobilized into a lipid matrix, which mimics biomembranes, and provides a platform for biosensing devices.[30]

1.5 Self-Assembled Monolayers of Alkanethiolates

Another way to prepare monomolecular films is the use of alkanethiols that form self-assembled monolayers (SAMs) on the surface of various metals such as gold, silver, copper, palladium, platinum, germanium, and mercury.[31-34] The affinity of the thiol for the substrate, combined with intermolecular forces, drive the self-assembly of the molecules into a well-ordered monolayer. The thickness of the SAMs formed typically ranges from 1 to 3 nm and their presence can drastically alter the surface properties of the metal or metal oxide.[34]

The structure of self-organizing molecules consists of a chemical functionality or “head-group” that has an affinity for the substrate, a spacer component capable of

intermolecular interactions, and a terminal group which confers interfacial properties to the monolayer (Figure 1.8).

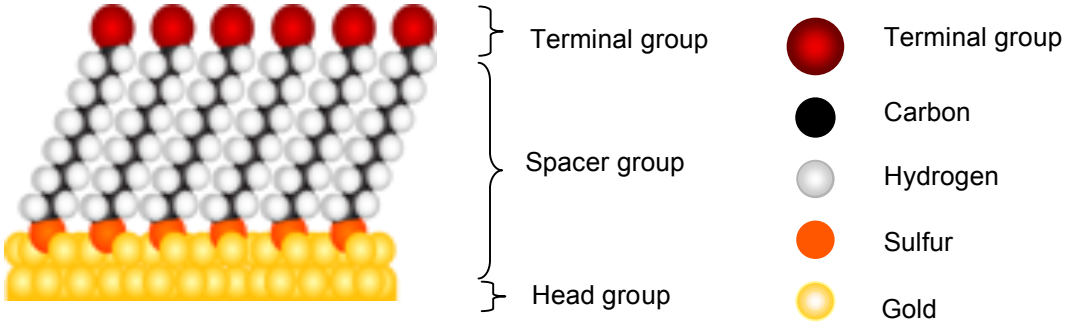

Figure 1.8 Schematic representation of a self-assembled monolayer of ω-functionalized alkanethiolates on gold (reproduced from ref. 35).

The preparation of SAMs is simple and consists of a clean substrate immersed into a saturated solution (10^{-3} M) of an *n*-alkanethiol (RSH) or alkydisulfide (RSSR) in organic solvent. The proposed reaction of alkanethiols or alkyldisulfides with gold is that of an oxidative addition of the S-H or S-S bond to gold, producing a gold(I)-thiolate species (Scheme 1.1).[32] The Au-S bond is largely covalent with some ionic character, and its homolytic bond strength has been measured to be 170-210 kJ mol^{-1}.[36-38]

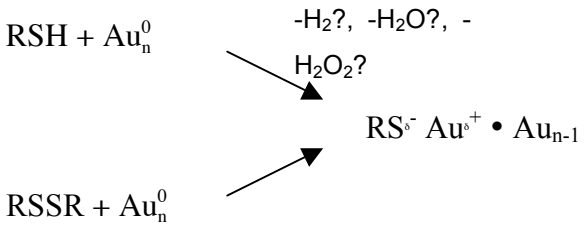

Scheme 1.1 Proposed reaction of alkylthiols or alkyldisulfides with gold.

The density and packing of the SAM depend on many factors such as the underlying crystal structure of the gold film,[39-41] the nature of the molecule and its purity,[42] the immersion solvent,[43-45] and incubation time[42,46].

1.6 ω-Functionalized Phospholipids

Phospholipids are ideal molecules to form biomimetic solid-supported monolayers, which can be used for biosensing.[30,47,48] On a solid substrate, monolayers of lipids are only physisorbed, making them weakly bound structures. Ihalainen and Peltonen devised the use of a phospholipid analogue, 1-palmitoyl-2-(16-(*S*-methyldithio)hexadecanoyl)-*sn*-glycero-3-phosphocholine (DSDPPC)[49-53] to covalently bind a binary monolayer onto gold using the LS deposition method. DSDPPC is an analogue of DPPC with a methyldisulfide modification at one of the tail ends. Its structure is given in Figure 1.9.

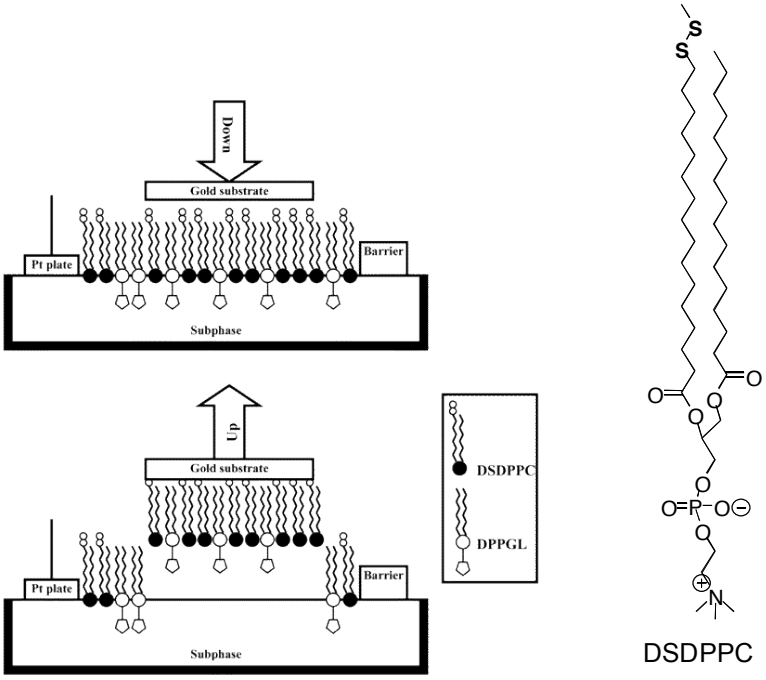

Figure 1.9 Schematic representation of a covalently bound LS binary monolayer on gold and chemical structure of DSDPPC (image reproduced from ref. 49).

This functionalized lipid allows for a strong anchoring of the molecule on a gold surface via Au-S bonding, leaving the phospholipid heads exposed. Most of the interactions of biomolecules with lipids occur at the phosphocholine head region of the lipid. Hence, a DSDPPC monolayer on gold can provide a robust platform for investigating the interaction of biomolecules such as proteins and enzymes with phospholipids.

By varying the film deposition technique, physisorbed DSDPPC monolayers with the methyldisulfide functionality exposed at the surface can also be obtained. For example, the conventional LB deposition (Figure 1.7B) on mica or Si/SiO_x results in a monolayer where the phosphocholine head group interacts electrostatically with the hydrophilic mica and the alkyl chains are exposed at the surface of the substrate (Figure 1.10A). To obtain a

monolayer with the alkyl chain interacting with the substrate (Figure 1.10B), the Langmuir-Schaefer method (Figure 1.7D) can be used to transfer the monolayer onto a substrate.

The disulfide group is a very versatile functional group with affinities for metals, proteins, and antibodies, providing an easy way to tailor the surface for different applications. DSDPPC and 1-lauroyl-2-(12-(*S*-methyldithio)dodecanoyl)-*sn*-glycero-3-phosphocholine (DSDLPC) containing 16 and 12 carbons respectively in their hydrocarbon chains, are disulfide modified phospholipids used in this research project.

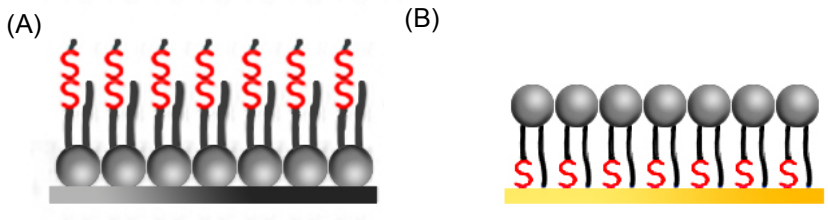

Figure 1.10 Schematic represention of (A) a DSDPPC monolayer physisorbed on mica or Si/SiO_x with exposed methyldisulfide groups, and (B) a DSDPPC monolayer covalently bound to gold.

1.7 Nanopatterning Techniques

The invention of the scanning probe microscope[54-55] in 1981 propelled the field of nanotechnology into a new era. This new microscope allowed one to "see" and "manipulate" matter at the nanoscale. The synthesis and characterization of new types of nanomaterials has exploded in the last three decades. The current fascination for nanoscale materials is due to the novel physical and chemical properties that these can exhibit. Nanopatterned surfaces are integral to both current and emerging technologies. The development of nanostructures can help towards the understanding of fundamental phenomena such as metal/organic interactions at the nanoscale, nucleation and growth of

crystals and nanomaterials, and the spatial alignment of molecules. Solid-supported nanostructures are central to the advancement of many fields of research such as organic molecular electronics, plasmonics, tissue engineering, biosensing, chemical sensing, and many more.

Constant effort is directed towards the fabrication of nanopatterned surfaces. Numerous methods have been developed each with their pros and cons. The following techniques are termed "top-down" because they involve carefully using tools to carve or shape material. Photolithography and electron beam lithography are mostly used in the semiconductor industry. Features of 45 nm are produced routinely using lithography.[56] Pushing the limit beyond a resolution of 20 nm can be achieved using extreme ultraviolet lithography[57] or e-beam lithography[58], but these require complex instrumentation and are expensive. Nanoimprint lithography (NIL) is another technique to pattern surfaces involving molding and embossing.[59] A rigid mold (itself patterned using conventional photolithography) is pressed against a polymer film that is heated above its glass transition temperature. After cooling, the polymer retains the shape of the mold. Structures, as small as 5 nm, can be obtained. The resolution of NIL greatly depends on the quality of the mold, which is very expensive to produce. The material's ability to mold the features of the master can also affect the nanopattern. Another widely used technique to create nanoscale features is microcontact printing (μCP), a method developed by George Whitesides and coworkers.[60] A stamp made of polydimethylsiloxane (PDMS) is coated with a solution of molecules, typically alkanethiols, and brought into contact with a suitable substrate. The molecules act as the ink and transfer from the PDMS stamp onto the substrate.[34] Features as small as 30 nm can be obtained. Large and curved areas can be patterned. Again, the resolution of the pattern depends on the master (produced using lithography methods) used to create the stamp. Diffusion of the molecules can deform the pattern and the molecules and substrate need to be carefully chosen. To transfer from the stamp to the substrate, the molecules need to preferentially absorb to the substrate. All the methods described above require the use of photo- or electron beam lithography to create a mask, a master or patterned substrates.

Lithography-free methods such as scanning probe microscopy (SPM) can also be used for nanopatterning. The cantilever tip of the atomic force microscope can be used as a "pen" and inked with alkanethiol to pattern a surface (dip pen nanolithography),[61] or it can be used to remove molecules from the surface. The drawback of SPM lithography is mainly its serial nature, making it hard to pattern large areas.

Over the past two decades, other lithography-free methodologies based on large-scale self-assembly have been developed to pattern solid surfaces at low cost.[62,63] Block copolymers are the most widely used molecules to form self-assembled structures. These molecules are long polymeric chains that have two or more blocks that are incompatible. Nanopatterns arise from phase separation[64] of the different segments of the block copolymers into microdomains. Block copolymers can self-assemble to form spheres, cylinders, gyroids, lamellae, or more complex shapes. Extensive reviews on polymers for templating have been published.[65-67] The following are two examples of polymer self-assembly for the directed deposition of metals.

Buriak *et al.*[68] used a monolayer of a triblock copolymer polystyrene-block-poly(2-vinylpyridine)-block-poly(ethylene oxide) (PS-*b*-P2VP-*b*-PEO) to generate a monolayer template to create metallic structures on silicon. The PS-*b*-P2VP-*b*-PEO forms cylindrical micelles when spin-coated on silicon (Figure 1.11A). The P2VP core block is selective towards gold ions while PEO corona attracts Ag ions. Metal ions undergo spontaneous reduction via galvanic displacement with silicon. The loaded triblock copolymer self-assembles onto a silicon surface and a pattern of metallic structures is produced (Figure 1.11B and C).

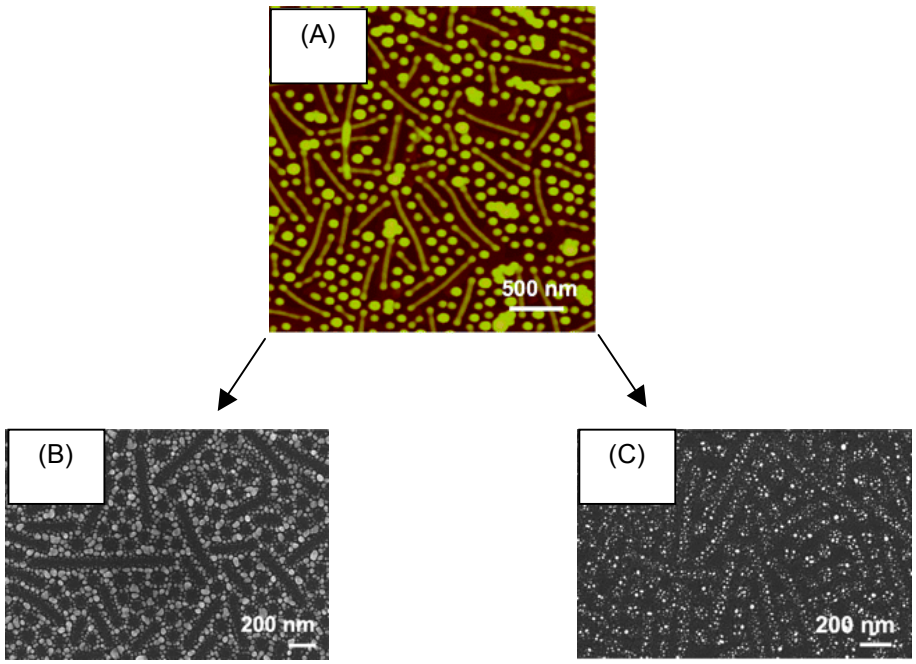

Figure 1.11 (A) AFM image of self-assembled PS-*b*-P2VP-*b*-PEO triblock copolymer on Si(100) wafer, and SEM image of (B) Au and (C) Ag nanostructures on the polymer template (reproduced from ref. 68).

Nanosphere lithography[70-74] (NSL) is also becoming a very promising technique to produce metallic nanostructures. Polystyrene latex beads of mono dispersed size are spin-coated[75] or dip-coated[76] onto a substrate and they generate a hexagonally close-packed pattern on the substrate (Figure 1.12). Beads ranging from 200 to 600 nm have been used. Metal is then thermally evaporated onto this pattern, which serves as a mask. The beads are

simply removed by sonication in an organic solvent leaving a pattern of metal nanostructures. Various parameters can be tuned to obtain metal nanostructures ranging from 20 to 1000 nm in size.

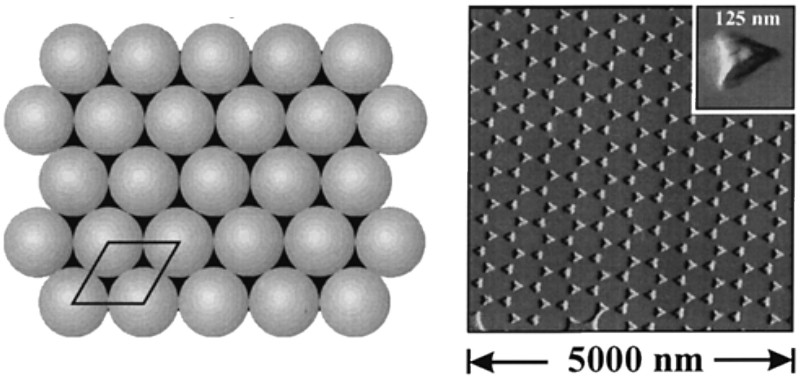

Figure 1.12 (A) Schematic representation of hexagonal packing of polystyrene beads and (B) AFM image of Ag nanostructures formed from beads of 400 nm in diameter (image reproduced from ref. 71).

1.8 Surface Patterning using Langmuir Films

LB technology is a well-established "bottom-up" method for preparing (ultra-)thin films that are highly structured in the vertical and/or lateral directions.[77-81] Several reports have demonstrated the potential of the LB technique for preparing solid-supported films that are chemically or physically differentiated on the micron to submicron scale. Laterally patterned LB films are typically generated by the transfer onto substrates of two-dimensional arrays of domains formed at the A/W interface by the pressure-induced, lateral phase separation of immiscible molecules or units, such as amphiphilic diblock copolymers[65,82-84] and mixtures of long-chain fatty acids[85-87] or lipids[4,88,89]. Alternatively, the vertical transfer process itself can produce a regular surface pattern from a homogeneous monolayer precusor.[79,81] The latter type of LB patterning results from oscillations of the water meniscus height on the withdrawing substrate that are triggered by

solid surface-mediated changes in the molecular density or composition of the monolayer film at the three-phase contact line (air/aqueous subphase/solid substrate).[90-97] These oscillations switch the monolayer deposition between one phase and another, yielding patterns of parallel stripes or bands. Several chemical systems (e.g., phospholipids,[98-100] arachidic acid/cadmium arachidate,[101] lipid/lipopolymer mixture,[102] metal nanoparticles,[97,103] phospholipid/polymerization initiator mixture,[104] and organic semiconductors[105,106]) have been successfully patterned by exploiting the dewetting instabilities caused by contact line interactions, suggesting the controlled manipulation of the moving front during vertical film transfer or dip-coating as a versatile method for producing linear surface patterns of materials. The appropriate choice of LB transfer parameters (transfer speed, surface pressure, temperature) and monolayer composition should open new opportunities for generating high density surface patterns from amphiphilic (macro-)molecules without the restrictive need for a lateral pre-organization of nanostructures at the A/W interface.

It is important to point out that the patterns generated using the LB approach typically exhibit variability in the feature widths and spacings. Thus, while this type of patterning may not produce the level of perfection required for technological applications, as is also the case for pattern/array formation using the self-assembly of other materials such as block copolymers and nanospheres,[107] it nonetheless constitutes a readily accessible, simple, and high-throughput way to generate surface templates that are sufficiently ordered for fundamental or proof-of-concept research, such as the spatially selective metallization studies described in this thesis.

Chi *et al.* demonstrated the formation of periodic arrays of phospholipid stripes (~800 nm wide) separated by empty channels (~200 nm wide) using the wetting instabilities caused by the substrate-mediated condensation of a DPPC monolayer.[98] Badia *et al.* subsequently reported the preparation of stripe patterns using the LB transfer of a phase-separated binary mixture of phospholipids of different hydrocarbon chain lengths.[81] The stripe patterns result from the initial self-association of like lipids (hydrophobic match) at the A/W interface during monolayer compression to give condensed domains of one

lipid that are dispersed in a fluid matrix of the second lipid, followed by the self-organization and coalescence of the lipid domains at the three-phase contact line during LB deposition. The mean stripe widths could be tuned from ~300 nm down to ~60 nm by varying the phospholipid composition and transfer pressure.[81] Applications of the phospholipid stripes to the selective adsorption of proteins,[108] fabrication of patterned bilayer membranes,[109] and enzymatic lithography[110] have been demonstrated. What distinguishes the phospholipid stripe patterns generated by Chi *et al.* and Badia *et al.* from the domain motifs of ribbons, rods, strands, fingerprints (Figure 1.13A), ripples, wires or spaghetti[83,87,88,111,112] more typically observed in Langmuir monolayers is their highly parallel and undeviating nature (Figure 1.13B).

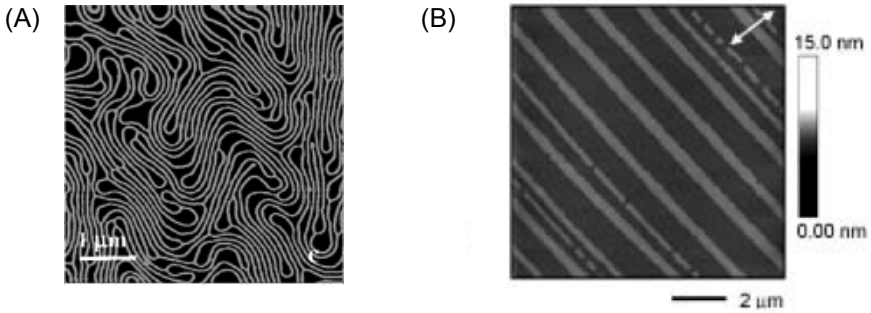

Figure 1.13 (A) Fingerprints nanopattern of polystyrene-*b*-poly(4-vinylpyridine) (reproduced from ref. 83) and, (B) AFM image of highly parallel stripes of phospholipid film (reproduced from ref. 81). Both films were deposited the by LB film deposition method.

1.9 Present Work

The generation of chemically-differentiated patterns would expand the templating possibilities of the mixed phospholipid monolayers. The challenge lies in using a functionalized lipid that will let the mixed monolayer transfer to surfaces in stripes.[103] The original patterns were produced with the condensed-phase-forming DPPC and fluid-phase-forming dilauroylphosphatidylcholine (DLPC).[113]

The objectives of this doctorate research are to:

- improve the regularity of the DPPC/DLPC stripe pattern and stripe widths by varying the experimental conditions and using a lineactant (cholesterol);
- investigate the physical properties of the ω-methyldisulfide-terminated analogues, DSDPPC and DSDLPC, in vesicle and monolayer form;
- form monolayers of the phospholipid analogues that exhibit a parallel stripe morphology;
- achieve the selective deposition of metals onto the methyldisulfide functional groups of the functionalized lipids by physical vapor deposition.

This thesis is divided into six chapters:

An overview of various nanopatterning techniques with a focus on the Langmuir-Blodgett film technique used as a nanopatterning tool is presented in Chapter One.

Chapter Two reports our attemp at controlling the uniformity and feature size of the DPPC/DLPC nanopatterns. A variation of the deposition speed, phospholipid composition, surface pressure at which the film is collected for the A/W interface, and the addition of a lineactant, cholesterol, give rise to a variety of nanostructures.

In Chapter Three, the phase behaviour of the phospholipid analogues is characterized, followed by the fabrication and characterization of single-component ω-methyldisulfide phospholipid films at the A/W interface, as well as solid-supported films

prepared by the LB and LS deposition techniques. The interfacial behaviour of the analogues is compared with that of the unmodified DPPC and DLPC.

Chapter Four presents the π-*A* isotherms, film morphologies at the A/W interface as characterized by BAM, and film morphologies of solid-supported LB and LS films of mixed monolayers of natural and modified DPPC and DLPC.

In Chapter Five, an investigation of the adsorption of metal vapor onto monolayers and mixed monolayers comprised of disulfide functionalized lipids is presented. Several surface analysis techniques (XPS, FEGSEM, AFM phase imaging, and AFM topography imaging) are used to examine the hybrid organic/inorganic nanopatterned monolayer films.

Chapter Six presents the general conclusions that can be drawn from this work and an outlook on future work is proposed.

1.10 References

(1) http://en.wikivisual.com/index.php/Cell_membrane. August 2010.

(2) http://www.vcbio.science.ru.nl/en/fesem/applets/amphiphiles/. August 2010.

(3) Petty, M. C. *Langmuir-Blodgett Films. An Introduction*; Cambridge University Press: Cambridge, 1996.

(4) Sanchez, J.; Badia, A. *Chem. Phys. Lipids* **2008**, *152*, 24.

(5) Meunier, J. *Colloids Surf. A* **2000**, *171*, 33.

(6) Hoenig, D.; Moebius, D. *J. Phys. Chem.* **1991**, *95*, 4590.

(7) DeWolf, C.; Leporatti, S.; Kirsch, C.; Brezesinski, G. *Chem. Phys. Lipids* **1999**, *97*, 129.

(8) Vollhardt, D.; Fainerman, V. B. *Adv. Colloid Interface Sci.* **2010**, *154*, 1 and references therein.

(9) Wang, X.; Zheng, S.; He, Q.; Brezesinski, G.; Möhwald, H.; Li, J. *Langmuir* **2004**, *21*, 1051.

(10) Kjaer, K.; Als-Nielsen, J.; Helm, C. A.; Laxhuber, L. A.; Möhwald, H. *Phys. Rev. Lett.* **1987**, *58*, 2224.

(11) Knobler, C. M. *Science* **1990**, *249*, 870.

(12) Lipp, M. M.; Lee, K. Y.; Waring, A.; Zasadzinski, J. A. *Biophys. J.* **1997**, *72*, 2783.

(13) Möhwald, H. *Annu. Rev. Phys. Chem.* **1990**, *41*, 441.

(14) McConnell, H. M. *Ann. Rev. Phys. Chem.* **1991**, *42*, 171.

(15) Keller, D. J.; Korb, J. P.; McConnell, H. M. *J. Phys. Chem.* **1987**, *91*, 6417.

(16) Vanderlick, T. K.; Möhwald, H. *J. Phys. Chem.* **1990**, *94*, 886.

(17) Seul, M.; Andelman, D. *Science* **1995**, *267*, 476.

(18) Mouritsen, O. G. *Life as a Matter of Fat*; Springer-Verlag Berlin Heidelberg: New York, 2005.

(19) Nandi, N.; Vollhardt, D. *Acc. Chem. Res.* **2007**, *40*, 351.

(20) Marsh, D. *CRC Handbook of Lipid Bilayers*; CRC Press, Inc.: Boca Raton, FL, 1990.

(21) Bagatolli, L. A.; Gratton, E. *Biophys. J.* **2000**, *79*, 434.

(22) Bagatolli, L. A.; Gratton, E. *Biophys. J.* **2000**, *78*, 290.

(23) Sanchez, J.; Badia, A. *Thin Solid Films* **2003**, *440*, 223.

(24) Abousalham, A.; Fotiadu, F.; Buono, G.; Verger, R. *Chem. Phys. Lipids* **2000**, *104*, 93.

(25) Lai, C. C.; Yang, S. H.; Finlayson-Pitts, B. J. *Langmuir* **1994**, *10*, 4637.

(26) Benvegnu, D. J.; McConnell, H. M. *J. Phys. Chem.* **1993**, *97*, 6686.

(27) Coban, O.; Popov, J.; Burger, M.; Vobornik, D.; Johnston, L. J. *Biophys. J.* **2007**, *92*, 2842.

(28) Yuan, J.; Fischer, T. M. *Langmuir* **2007**, *23*, 3603.

(29) Maget-Dana, R. *Biochim. Biophys. Acta* **1999**, *1462*, 109.

(30) Girard-Egrot, A. P.; Marquette, C. A.; Blum, L. J. *Int. J. Nanotechnology* **2010**, *7*, 735.

(31) Bigelow, W. C.; Pickett, D. L.; Zisman, W. A. **1946**, *1*, 513.

(32) Ulman, A. *Chem. Rev.* **1996**, *96*, 1533.

(33) Poirier, G. E. *Chem. Rev* **1997**, *97*, 1117.

(34) Love, J. C.; Estroff, L., A.; Kriebel, J., K.; Nuzzo, R., G.; Whitesides, G., M. *Chem Rev* **2005**, *105*, 1103.

(35) Lennox, B. http://lennoxlab.chem.mcgill.ca/, August 2010.

(36) Bain, C. D.; Whitesides, G. M. *Angew. Chem. Int. Ed. Engl.* **1989**, *28*, 506.

(37) Xu, J.; Li, H.; Zhang, Y. *J. Phys. Chem.* **1993**, *97*, 11497.

(38) Ulman, A. *MRS Bulletin* **1995**, *20*, 46.

(39) Delamarche, E.; Michel, B.; Biebuyck, H. A.; Gerber, C. *Adv. Mater.* **1996**, *8*, 719.

(40) Chiang, S. *Chem. Rev.* **1997**, *97*, 1083.

(41) Yang, Y. W.; Fan, L. J. *Langmuir* **2002**, *18*, 1157.

(42) Bain, C. D.; Troughton, E. B.; Tao, Y. T.; Evall, J.; Whitesides, G. M.; Nuzzo, R. G. *J. Am. Chem. Soc.* **1989**, *111*, 321.

(43) Ishida, T.; Mizutani, W.; Azehara, H.; Sato, F.; Choi, N.; Akiba, U.; Fujihira, M.; Tokumoto, H. *Langmuir* **2001**, *17*, 7459.

(44) Dannenberger, O.; Wolff, J. J.; Buck, M. *Langmuir* **1998**, *14*, 4679.

(45) Yamada, R.; Sakai, H.; Uosaki, K. *Chem. Lett.* **1999**, *28*, 667.

(46) Bensebaa, F.; Voicu, R.; Huron, L.; Ellis, T. H.; Kruus, E. *Langmuir* **1997**, *13*, 5335.

(47) Cornell, B. A.; Braach-Maksvytis, V. L.; King, L. G.; Osman, P. D.; Raguse, B.; Wieczorek, L.; Pace, R. J. *Nature* **1997**, *387*, 555.

(48) Sackmann, E. *Science* **1996**, *271*, 43.

(49) Ihalainen, P.; Peltonen, J. *Langmuir* **2002**, *18*, 4953.

(50) Runquist, E. A.; Helmkamp Jr, G. M. *Biochim. Biophys. Acta* **1988**, *940*, 10.

(51) Selinger, Z.; Lapidot, Y. *J. Lipid Res.* **1966**, *7*, 174.

(52) Ihalainen, P.; Peltonen, J. *Langmuir* **2003**, *19*, 2226.

(53) Ihalainen, P.; Peltonen, J. *Sensor Actuat. B-Chem.* **2204**, *102*, 207.

(54) Binnig, G.; Rohrer, H.; Gerber, C.; Weibel, E. *Phys. Rev. Lett.* **1982**, *49*, 57.

(55) Binnig, G.; Quate, C. F.; Gerber, C. *Phys. Rev. Lett.* **1986**, *56*, 930.

(56) Willson, C. G.; Roman, B. J. *ACS Nano* **2008**, *2*, 1323.

(57) Wu, B.; Kumar, A. *J. Vac. Sci. Technol. B* **2007**, *25*, 1743.

(58) Tseng, A. A.; Kuan, C.; Chen, C. D.; Ma, K. J. *IEEE Trans. Electron. Packag. Manuf.* **2003**, *26*, 141.

(59) Schift, H. *J. Vac. Sci. Technol. B* **2008**, *26*, 458.

(60) Kumar, A.; Whitesides, G. M. *Appl. Phys. Lett.* **1993**, *63*, 2002.

(61) Salaita, K.; Wang, Y.; Mirkin, C. A. *Nature Nanotech.* **2007**, *2*, 145.

(62) Gates, B. D.; Xu, Q.; Love, J. C.; Wolfe, D. B.; Whitesides, G. M. *Annu. Rev. Mater. Res.* **2004**, *34*, 339.

(63) Gates, B. D.; Xu, Q.; Stewart, M.; Ryan, D.; Willson, C. G.; Whitesides, G. M. *Chem. Rev.* **2005**, *105*, 1171.

(64) Leibler, L. *Macromolecules* **1980**, *13*, 1602.

(65) Cox, J. K.; Yu, K.; Constantine, B.; Eisenberg, A.; Lennox, R. B. *Langmuir* **1999**, *15*, 7714.

(66) Lopes, W. A. *Phys. Rev. E* **2002**, *65*, 031606.

(67) Li, H.; Huck, W. T. S. *Curr. Opin. Solid State Mater. Sci.* **2002**, *6*, 3.

(68) Aizawa, M.; Buriak, J. M. *Chem. Mater.* **2007**, *19*, 5090.

(69) Meli, M.-V.; Badia, A.; Grütter, P.; Lennox, R. B. *Nano Lett.* **2001**, *2*, 131.

(70) Huang, W.; Qian, W.; El-Sayed, M. A. *Nano Lett.* **2004**, *4*, 1741.

(71) Haynes, C. L.; Van Duyne, R. P. *J. Phys. Chem. B* **2001**, *105*, 5599.

(72) Russell, B. K.; Mantovani, J. G.; Anderson, V. E.; Warmack, R. J.; Ferrell, T. L. *Phys. Rev. B* **1987**, *35*, 2151.

(73) Deckman, H. W.; Dunsmuir, J. H.; Garoff, S.; McHenry, J. A.; Peiffer, D. G. *J. Vac. Sci. Technol. B* **1988**, *6*, 333.

(74) Bullen, H. A.; Garrett, S. J. *Nano Lett.* **2002**, *2*, 739.

(75) Hulteen, J. C.; Van Duyne, R. P. *J. Vac. Sci. Technol. A* **1995**, *13*, 1553.

(76) Hulteen, J. C.; Treichel, D. A.; Smith, M. T.; Duval, M. L.; Jensen, T. R.; Van Duyne, R. P. *J. Phys. Chem. B* **1999**, *103*, 3854.

(77) Motschmann, H.; Möhwald, H. Langmuir-Blodgett Films. In *Handbook of Applied Surface and Colloid Chemistry*; Holmberg, K., Ed.; John Wiley & Sons, Ltd, 2001; pp 629.

(78) Lenhert, S.; Li, Z.; Mueller, J.; Wiesmann, H. P.; Erker, G.; Fuchs, H.; Chi, L. *Adv. Mater.* **2004**, *16*, 619.

(79) Chen, X.; Lenhert, S.; Hirtz, M.; Lu, N.; Fuchs, H.; Chi, L. *Acc. Chem. Res.* **2007**, *40*, 393.

(80) Tao, A. R.; Huang, J.; Yang, P. *Acc. Chem. Res.* **2008**, *41*, 1662.

(81) Badia, A.; Moraille, P.; Tang, N. Y. W.; Randlett, M.-E. *Int. J. Nanotechnol.* **2008**, *5*, 1371.

(82) Zhu, J.; Eisenberg, A.; Lennox, R. B. *J. Am. Chem. Soc.* **1991**, *113*, 5583.

(83) Lu, Q.; Bazuin, C. G. *Nano Lett.* **2005**, *5*, 1309.

(84) Seo, Y.-S.; Kim, K. S.; Galambos, A.; Lammertink, R. G. H.; Vancso, G. J.; Sokolov, J.; Rafailovich, M. *Nano Lett.* **2003**, *4*, 483.

(85) Qaqish, S. E.; Paige, M. F. *Langmuir* **2007**, *23*, 10088.

(86) Overney, R. M.; Meyer, E.; Frommer, J.; Guentherodt, H. J.; Fujihira, M.; Takano, H.; Gotoh, Y. *Langmuir* **1994**, *10*, 1281.

(87) Kimura, H.; Watanabe, S.; Shibata, H.; Azumi, R.; Sakai, H.; Abe, M.; Matsumoto, M. *J. Phys. Chem. B* **2008**, *112*, 15313.

(88) Seul, M.; Chen, V. S. *Phys. Rev. Lett.* **1993**, *70*, 1658.

(89) Dufrêne, Y. F.; Barger, W. R.; Green, J.-B. D.; Lee, G. U. *Langmuir* **1997**, *13*, 4779.

(90) Graf, K.; Riegler, H. *Colloids Surf. A* **1998**, *131*, 215.

(91) Kovalchuk, V. I.; Bondarenko, M. P.; Zholkovskiy, E. K.; Vollhardt, D. *J. Phys. Chem. B* **2003**, *107*, 3486.

(92) Lenhert, S.; Gleiche, M.; Fuchs, H.; Chi, L. *ChemPhysChem* **2005**, *6*, 2495.

(93) Riegler, H.; Spratte, K. *Thin Solid Films* **1992**, *210/211*, 9.

(94) Spratte, K.; Chi, L. F.; Riegler, H. *Europhys. Lett.* **1994**, *25*, 211.

(95) Spratte, K.; Riegler, H. *Langmuir* **1994**, *10*, 3161.

(96) Raudino, A.; Pignataro, B. *J. Phys. Chem. B* **2007**, *111*, 9189.

(97) Huang, J.; Kim, F.; Tao, A. R.; Connor, S.; Yang, P. *Nature Mater.* **2005**, *4*, 896.

(98) Gleiche, M.; Chi, L. F.; Fuchs, H. *Nature* **2000**, *403*, 173.

(99) Pignataro, B.; Sardone, L.; Marletta, G.; C, M. S. E. *Mater. Sci. Eng. C* **2002**, *22*, 177.

(100) Chen, X.; Lu, N.; Zhang, H.; Hirtz, M.; Wu, L.; Fuchs, H.; Chi, L. *J. Phys. Chem. B* **2006**, *110*, 8039.

(101) Mahnke, J.; Vollhardt, D.; Stöckelhuber, K. W.; Meine, K.; Schulze, H. J. *Langmuir* **1999**, *15*, 8220.

(102) Purrucker, O.; Förtig, A.; Lüdtke, K.; Jordan, R.; Tanaka, M. *J. Am. Chem. Soc.* **2005**, *127*, 1258.

(103) Huang, J.; Tao, A. R.; Connor, S.; He, R.; Yang, P. *Nano Lett.* **2006**, *6*, 524.

(104) Brinks, M. K.; Hirtz, M.; Chi, L.; Fuchs, H.; Studer, A. *Angew. Chem., Int. Ed.* **2007**, *46*, 5231.

(105) Li, L.; Gao, P.; Schuermann, K. C.; Ostendorp, S.; Wang, W.; Du, C.; Lei, Y.; Fuchs, H.; Cola, L. D.; Müllen, K.; Chi, L. *J. Am. Chem. Soc.* **2010**, *132*, 8807.

(106) Liu, N.; Zhou, Y.; Wang, L.; Peng, J.; Wang, J.; Pei, J.; Cao, Y. *Langmuir* **2009**, *25*, 665.

(107) Xia, Y.; Rogers, J. A.; Paul, K. E.; Whitesides, G. M. *Chem. Rev.* **1999**, *99*, 1823.

(108) Moraille, P.; Badia, A. *Angew. Chem., Int. Ed.* **2002**, *41*, 4303.

(109) Moraille, P.; Badia, A. *Langmuir* **2003**, *19*, 8041.

(110) Moraille, P.; Badia, A. *J. Am. Chem. Soc.* **2005**, *127*, 6546.

(111) Qaqish, S. E.; Paige, M. F. *Langmuir* **2008**, *24*, 6146.

(112) Kim, Y.; Pyun, J.; Fréchet, J. M. J.; Hawker, C. J.; Frank, C. W. *Langmuir* **2005**, *21*, 10444.

(113) Moraille, P.; Badia, A. *Langmuir* **2002**, *18*, 4414.

Chapter 2 Controlling the Features of the Stripe Pattern

2.1 Introduction

The formation of a pattern of parallel stripes of pure DPPC by substrate-induced condensation was first reported by Spratte *et al.*[1] and further developed by Chi, Fuchs, and coworkers[2]. DPPC films were transferred onto a substrate using the LB technique at surface pressures below the LE-C phase transition pressure of DPPC. Stripes form parallel to the three-phase contact line (i.e., perpendicular to direction of pulling) during the vertical transfer process. An alternating pattern is obtained consisting of DPPC stripes with widths of about 800 nm separated by bare substrate channels of 200 nm (Figure 2.1). Variation of the film transfer parameters (surface pressure and substrate withdrawal speed) produces different patterns such as grids and vertical lines of condensed DPPC.

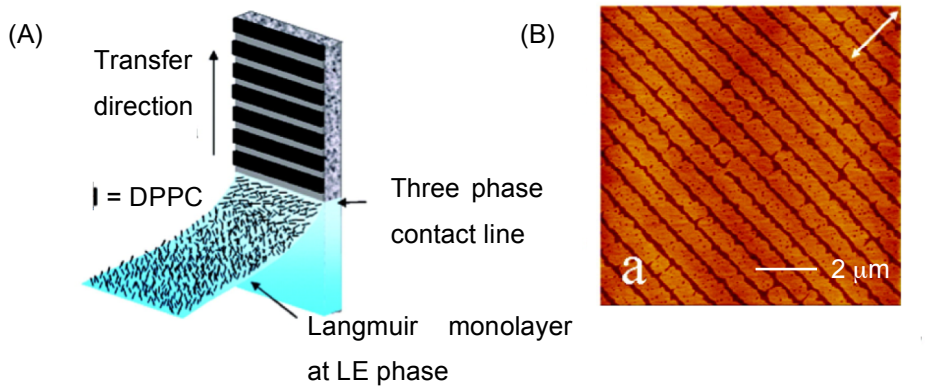

Figure 2.1 (A) Schematic representation of substrate-induced condensation formation of a stripe pattern by LB, and (B) AFM image of DPPC film transferred at 3 mN m^{-1}, at a substrate withdrawal of 60 mm min^{-1}, at T = 22.5 °C. The white arrow indicates the direction of substrate pulling (reproduced from ref. 2).

Fuchs *et al.* also investigated the addition of a second component to the DPPC: 1,2-di(2,4-octadecadienoyl)-*sn*-glycero-3-phosphocholine (DOEPC) at mole fractions ranging from 0.1 to 0.33, and the addition of cholesterol.[3] DOEPC is an unsaturated lipid that remains in a LE phase, while cholesterol is a lipid that has a condensing effect on phosphocholines. The authors report patterns with smaller periodicities (30 to 60 % reduction) than that of pure DPPC when either molecule is added. These studies suggest that the stripe pattern can be controlled to a certain extent by varying the lipid composition and LB transfer conditions.

The DPPC/DLPC stripe pattern explored in this thesis is not formed due to the substrate-mediated condensation of phospholipid because the mixed monolayer film is transferred at a surface pressure above the LE-C phase transition of the mixture and condensed domains already exist at the A/W interface (Figure 2.2A) Instead, a cycle of phase nucleation and depletion gives rise to parallel lines of DPPC surrounded by a DLPC matrix (Figure 2.2B).

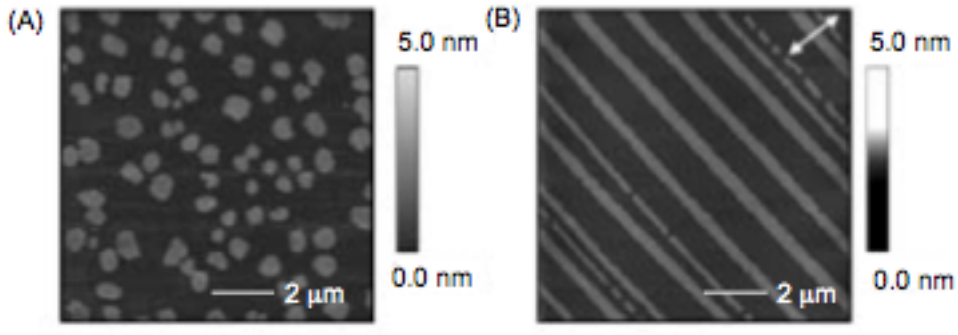

Figure 2.2 AFM images of DPPC/DLPC 1:1 (mol:mol) transferred onto mica at 15 mN m^{-1} and T = 20.0 °C by (A) LS and (B) LB deposition where the arrow indicates the direction of substrate withdrawal (reproduced from ref. 4).

Moraille and Badia proposed that at surface pressures above the LE-C transition pressure, the mixed monolayer is phase separated into an array of circular or elliptical DPPC-rich domains dispersed in a DLPC-rich background matrix.[5] The DPPC domains can be aligned and/or distorted by sheer forces during the vertical transfer process and coalesce to form a condensed DPPC band or stripe at the three-phase contact line. The build-up of solid DPPC near the contact line leads to a cycle where the contact angle and meniscus height change due to differences in the interfacial energy between the solid-like DPPC and liquid-like DLPC phases. A depletion phase containing DLPC and broken DPPC stripes is deposited and the meniscus height fluctuates again (Figure 2.3). The entire process is cyclical because the substrate motion is continuous during the LB transfer. This phenomenon is often referred to as stick-slip or nucleation-depletion.

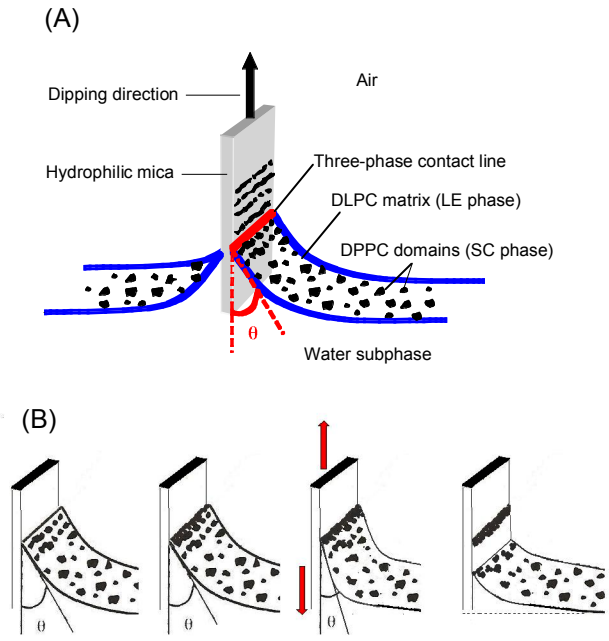

Figure 2.3 Schematic representation of (A) nucleation-depletion mechanism of stripe formation and (B) meniscus oscillation during substrate withdrawal.

By varying the lipid composition and film transfer pressure, the average stripe width could be varied from ~ 60 to ~ 300 nm. A feature of the DPPC/DLPC pattern produced is that wider continuous stripes are periodically interspersed among a more closely interspaced series of narrower broken stripes and there is a large distribution of the stripe widths (± 50%) and stripe spacings (± 40%). For fundamental or technological applications a more regular pattern is desirable. Understanding the effect of the experimental conditions on the formation of the stripe pattern is an important prerequisite to identifying strategies to control its feature dimensions and regularity.

In this Chapter, the morphologies of DPPC/DLPC monolayers at the A/W interface (monolayer precursor) are inferred by AFM imaging of LS films. We examine how variations of the experimental conditions, such as the film transfer pressure, substrate withdrawal speed, and mole fraction of DPPC (χ_{DPPC}) alter the features of the stripe pattern. Moraille and Badia previously investigated the effect of the film transfer speed and surface pressure on the stripe pattern formed by the LB deposition of DPPC/DLPC monolayers of $\chi_{DPPC} = 0.25$.[5] The authors found that an increased deposition speed leads to thinner broken stripes, and films deposited at higher surface pressures contain large microscopic flower-like domains interspersed between thinner broken lines. This chapter is a continuation of the Moraille and Badia study.[5] Films with χ_{DPPC} of 0.90, 0.75, and 0.50 are examined and the effect of surface pressure and film transfer speed is investigated. The effect of the lineactant cholesterol (chol) on the morphology of DPPC/DLPC 1:1 (mol/mol) is also reported.

2.2 Experimental Section

2.2.1 Materials

1,2-Dipalmitoyl-*sn*-glycero-3-phosphocholine (DPPC) and 1,2-dilauroyl-*sn*-glycero-3-phosphocholine (DLPC) both the natural L isomer, were obtained as powders from Avanti Polar Lipids, Inc. (Alabaster, AL) and used without further purification (chemical purity > 99%). Cholesterol (chol, 99+%) was purchased from Sigma Aldrich in

powder form and used without purification. Ruby muscovite mica (ASTM Grade 2) was purchased from B&M Mica Co., Inc. (Flushing, NY) and cleaved before use.

2.2.2 Preparation of LS and LB Films of Binary and Ternary Mixtures

A standard KSV 3000 LB trough (KSV Instruments Ltd. Helsinki, Finland) with a surface area of 768 cm^2 was used. The trough is equipped with a platinum Wilhelmy plate sensing device (KSV Instruments, Helsinki, Finland) and connected to an Isotemp 1006D circulation bath (Fisher Scientific). The subphase temperature was maintained at 20.0 ºC (± 0.5 ºC).

Solutions of DPPC, DLPC, DPPC/DLPC, and DPPC/DLPC/chol of 1 mM were prepared using spectrograde chloroform. Ternary mixtures of DPPC/DLPC/chol were prepared by keeping the molar ratio of DPPC/DLPC constant at 1:1. For example, the composition of a 5% chol solution is 47.5:47.5:5 DPPC/DLPC/chol. Monolayers were formed by spreading 100 μL of the appropriate solution on the water surface of the standard LB trough. The solvent was allowed to evaporate for 15 min. The phospholipid molecules were symmetrically compressed at a rate of 1 $Å^2$ $molecule^{-1}$ min^{-1}. The films were transferred onto mica by LS or LB deposition after 20 min stabilization once the desired pressure was reached. For LS deposition, the mica was held in place in a custom made stainless steel holder and placed under the film. The subphase was removed by suction until the film settled onto the mica. For LB deposition, a mica substrate (~25 x 30 mm) is suspended vertically placed in the subphase, and withdrawn at different pulling speeds from the subphase up through the floating monolayer.

2.2.3 AFM Imaging

Several scanning probe microscopes from Veeco Metrology Inc. (Santa Barbara, CA) were used interchangeably to image the samples under ambient conditions: a Dimension 3100 scanning probe microscope (Nanoscope V), an EnviroScope atomic force microscope (Nanoscope IIIa) equipped with a Quadrex Extender module or a Dimension 5000 (Nanoscope V). Height and phase contrast images were simultaneously acquired in

intermittent-contact ("tapping") mode using a damping of 70%-85% of the free oscillation amplitude of silicon probes (type PPP-NCH, Nanosensors) of nominal spring constant of 42 N m^{-1}, resonance frequency 330 kHz, and tip radius of curvature < 10 nm. Images were captured at scan rates of 1 - 1.5 Hz with 512 × 512 pixels per image regardless of the image size.

2.3 Results and Discussion

2.3.1 Effect of Surface Pressure on the Morphology of DPPC/DLPC Monolayers Transferred to Mica by LB versus LS Technique

In order to gain control over the morphology of the stripe pattern, a better understanding of the stripe formation is needed. A starting point would be to identify the kinds of structures that are present at the A/W interface and that form the highly parallel stripe pattern during LB deposition. A series of AFM images of DPPC/DLPC 50:50 (mol/mol) monolayers collected from the A/W interface using the LB technique, at various surface pressures (indicated by arrows on the π-*A* isotherm in Figure 2.4), are presented in Figure 2.5. All the films transferred between 10 mN m^{-1} and 32 mN m^{-1} exhibit a stripe pattern or some variation of it. At 10 mN m^{-1}, the stripes are thin and broken by vertical channels. A more regular pattern of continuous stripes is obtained when the film is transferred at 15 mN m^{-1}, just below the LE-C phase transition surface pressure (Figure 2.5 B).

Film deposition at surface pressures above the LE-C phase transition pressure (π = 20 mN m^{-1} and 25 mN m^{-1}) results in wider stripes, interspaced by narrowed broken stripes (Figures 2.5C and D) with flower-shaped domains coexisting with the stripe pattern. The morphology of films transferred at 30 mN m^{-1} constitute very large flower-like domains (~40 μm in diameter) interconnected with continuous or broken thin stripes (Figure 2.5E).

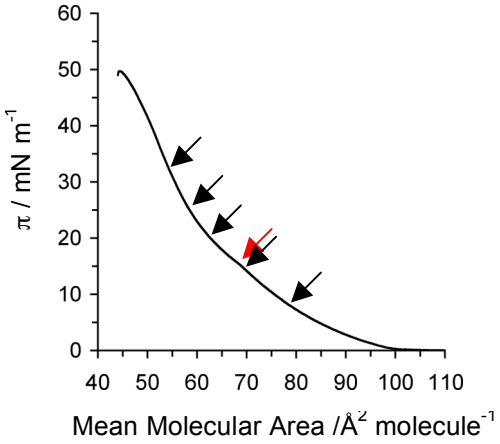

Figure 2.4 π-*A* isotherm of DPPC/DLPC 50:50 (mol/mol). Black arrows are indicative of π at which LB or LS films were collected and the red arrow identifies the LE-C phase transition.

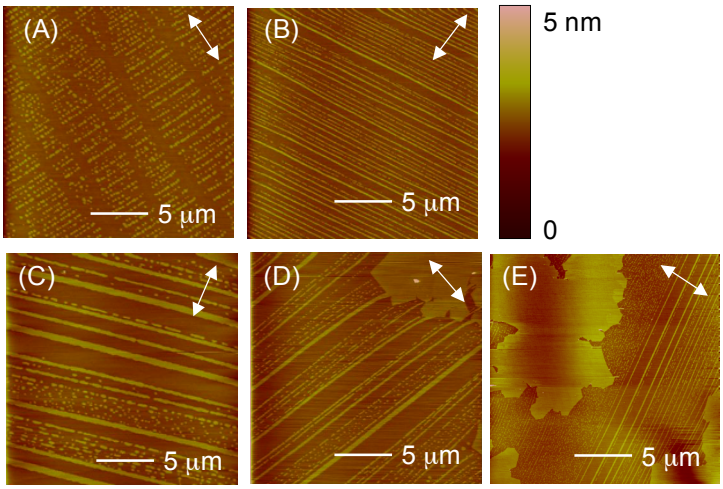

Figure 2.5 DPPC/DLPC 50:50 monolayer deposited at a rate of 5 mm min^{-1} on mica by LB at (A) 10 mN m^{-1}, (B) 15 mN m^{-1}, (C) 20 mN m^{-1}, (D) 25 mN m^{-1}, and (E) 30 mN m^{-1}. The white arrows indicate the direction of substrate withdrawal.

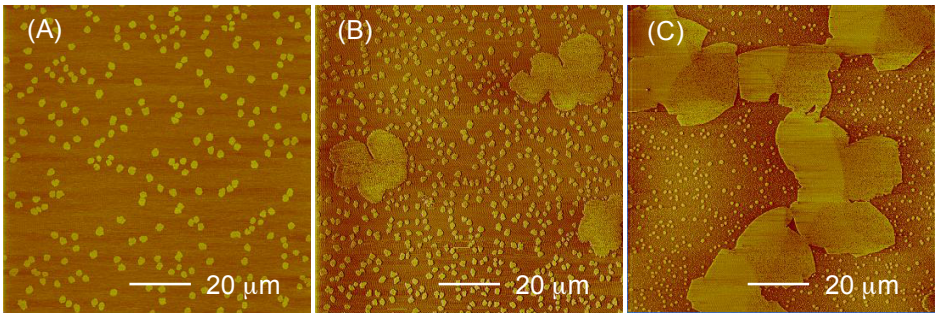

Figure 2.6 AFM images of DPPC/DLPC 50:50 monolayer deposited on mica by LS at (A) 10 mN m^{-1}, (B) 15 mN m^{-1}, and (C) 32 mN m^{-1}. Phase images are shown instead of height because of better image quality.

BAM is ideal to directly visualize the film morphology at the A/W interface. However, due to the lateral resolution of BAM ~ 2 μm, only large flower-like domains were observed at the A/W interface.[6] AFM imaging was used to detect the presence of nanoscopic structures of the monolayer films that were transferred onto mica, at different surface pressures, using the LS deposition method, in order to minimize deformation of the domain structure (Figure 2.6). When the film is compressed to π = 10 mN m^{-1} and transferred by LS, small condensed domains in the range of 3 to 5 μm in diameter exist (Figure 2.6A). These domains are too small to yield continuous parallel stripes during the LB transfer but are deformed into thin broken lines (Figure 2.5A vs. 2.6A). To obtain continuous lines, the film requires a compression to 15 mN m^{-1} where, by LS deposition, a mixture of circular domains of ~ 3 μm in diameter coexist with larger flower like domains of ~ 30 μm in diameter (Figure 2.5B vs 2.6B). In a film compressed to 32 mN m^{-1}, the small circular domains that were formed at 15 mN m^{-1} by LS shrink in size and number, giving place to much larger condensed domains that make up > 50% of the film surface at the A/W interface. When this film is transferred onto mica by LB, the big flower-like domains

remain and the small circular ones are elongated into broken or continuous stripes (Figure 2.5C vs. Figure 2.6C).

A critical domain size of about 30 μm seems to be the limit to obtain nucleation of DPPC domains into stripes. Domains with diameter greater than about 30 μm are larger then the cycle of nucleation-depletion and miniscus oscillation and transfer as is onto the substate.

2.3.2 Effect of the Mole Fraction of DPPC, Film Transfer Pressure and Film Transfer Speed on the Morphology of the Stripe Pattern

Based on the morphology of the stripe pattern obtained with DPPC/DLPC 50:50 mixtures, films transferred by LB at surface pressures below or near the LE-C phase transition give features without large flower-like domains. In the following section, we examine the morphology of films with different DPPC mole fractions (χ_{DPPC}) transferred by LB onto mica at various speeds and at surface pressures below or near the LE-C. The isotherms of DPPC/DLPC mixtures with different concentrations of DPPC are presented in Figure 2.7. The LE-C transitions manifest themselves as a plateau or kink in the π-*A* isotherms. The LE-C transition shifts to higher surface pressure as the mole fraction of DPPC diminishes. Table 2.1 summarizes the surface pressures at which the LE-C phase transition occurs as a function of χ_{DPPC}.

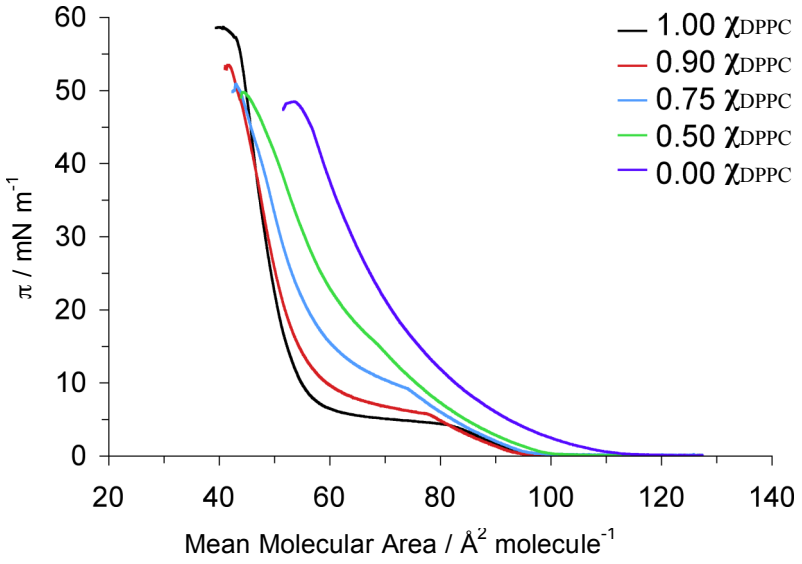

Figure 2.7 Isotherm of DPPC/DLPC monolayers at 20 °C of 1.00, 0.90, 0.75, 0.50 and 0.00.

Table 2.1 Chosen deposition pressures at which films of various DPPC mole fraction were transferred corresponding to their respective π_{LE-C} and below.

χ_{DPPC}	π_{LE-C} (mN m^{-1})	π below LE-C (mN m^{-1})
1.00	4	-
0.90	6	2
0.75	10	4
0.50	16	8

The π **below** the LE-C transition chosen for each mixture is given in Table 2.1. The films were transferred onto mica at deposition rates of 5 or 40 mm min^{-1}. The resulting morphologies are presented in Figure 2.8. At a film transfer rate of 5 mm min^{-1}, the stripes are the widest and spaced more closely at high DPPC content (χ_{DPPC} = 0.90). These become

thinner, more spaced apart and broken as χ_{DPPC} diminishes. At higher deposition speed (40 mm min^{-1}), condensed lines are broken or thinner than the corresponding film transferred at 5 mm min^{-1}. At χ_{DPPC} of 0.50, no continuous lines (only aligned circular domains) were observed at either deposition speeds at $\pi <$ LE-C transition pressure. As the film is transferred at π below the LE-C condensed phase transition, the mechanism of stripe formation is likely that of substrate-mediated condensation combined with meniscus oscillations during the LB transfer, as reported by Fuchs *et al.*[3] for single-component DPPC monolayers. As the authors increased the film transfer velocity from 1 to 60 mm min^{-1}, the initially wide stripes become thinner until an array of broken lines is obtained. The authors also state that the extent of the substrate mediate effect is decreased with the addition of a second component that remains in the LE phase. The same trend is observed in the DPPC/DLPC binary mixtures transferred below the LE-C transition. Higher transfer speed results in narrow broken stripes and a decrease in DPPC content also narrows the width of the stripes. These findings confirm that the stripes obtained using mixtures of DPPC/DLPC transferred at π below the LE-C transition pressure are generated by the substrate-mediated condensation.

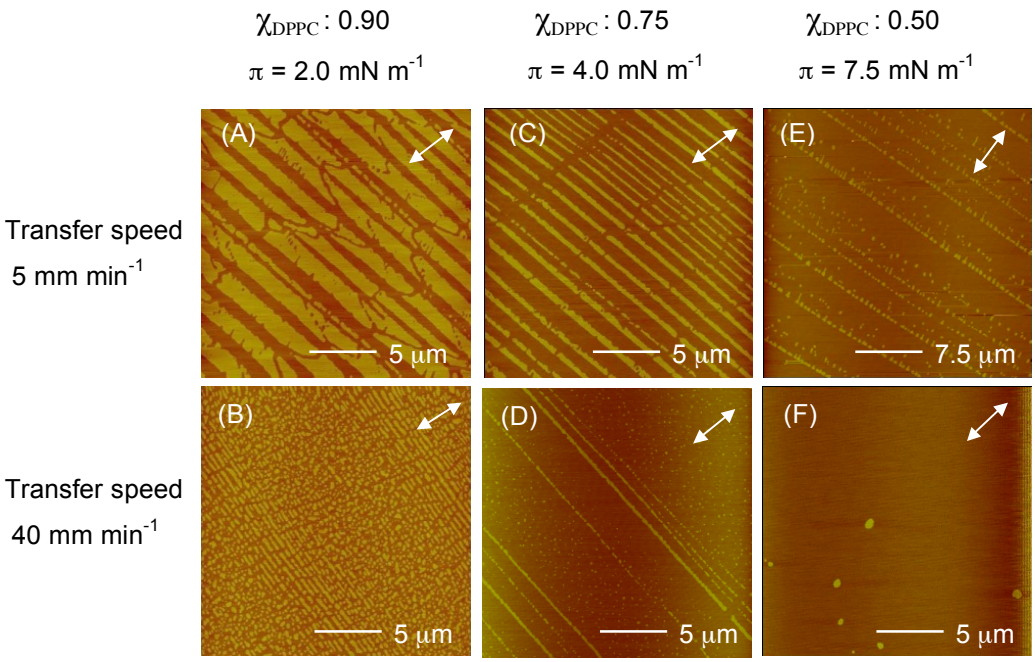

Figure 2.8 AFM images of DPPC/DLPC films formed using various χ_{DPPC} and different film transfer speeds collected at a surface pressure below (about mid-way) to the π of the LE-C phase transition. The white arrows indicate the direction of substrate withdrawal.

Patterns deposited **near** or **at** the LE-C transition using different χ_{DPPC} and different deposition speeds are shown in Figure 2.9. At χ_{DPPC} of 0.90, vertical trenches appear in the pattern at transfer speeds of 1 and 5 mm min^{-1} but are absent at transfer speeds faster than 20 mm min^{-1}. This phenomenon was also observed by Chen *et al.*[4] when LB films of pure DPPC films were transferred at 3 mN m^{-1} and speeds slower than 40 mm min^{-1}. They attributed the formation of vertical lines to a fingering instability.[7] Using DPPC/DLPC mixtures, the most periodic and continuous line patterns are obtained with χ_{DPPC} of 0.75 at a transfer speed of 5 mm min^{-1} or χ_{DPPC} of 0.50 with a transfer speed of 1 mm min^{-1} (Figures

2.9E and 2.9G). The widths of the lipid stripes obtained under the various conditions are given in Table 2.2. The pattern with the widest continuous stripes is obtained with a mixture of χ_{DPPC} of 0.75 transferred at 1 mm min^{-1}.

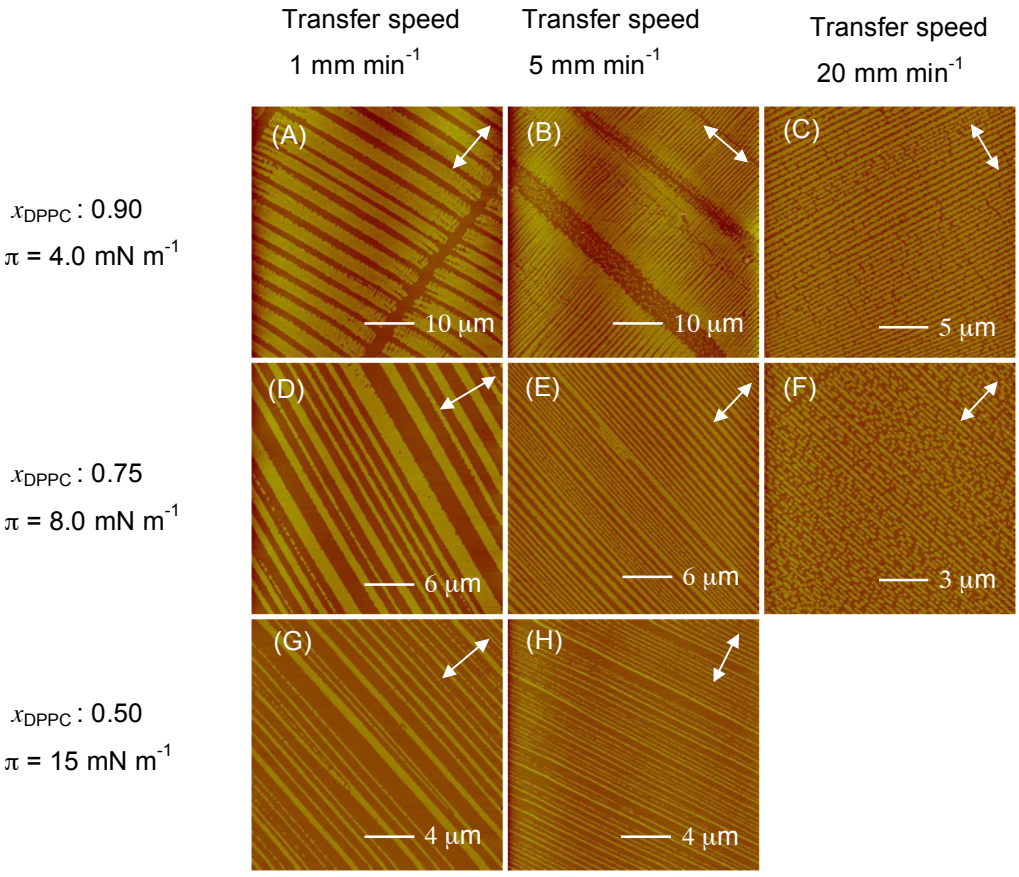

Figure 2.9 AFM images of DPPC/DLPC films of various χ_{DPPC} deposited onto mica by the LB technique and different substrate pulling speeds. The monolayers were collected from the A/W interface at a π at or near the LE-C phase transition. The white arrows indicate the direction of substrate withdrawal.

Table 2.2 Average phospholipid stripes widths of patterns formed at or near the LE-C phase transition pressures for χ_{DPPC} of 0.90, 0.75 and 0.50 deposited on mica by the LB technique at different film transfer speeds.

	Line widths at transfer speed of 1 mm min^{-1} (μm)	Line widths at transfer speed of 5 mm min^{-1} (μm)	Line widths at transfer speed 20 mm min^{-1} (μm)
χ_{DPPC}: 0.90	2.2 ± 0.6	0.6 ± 0.2	0.4 ± 0.1
χ_{DPPC}: 0.75	1.0 ± 0.4	0.3 ± 0.1	-
χ_{DPPC}: 0.50	0.3 ± 0.1	0.2 ± 0.1	-

* Line width averages calculated from at least 60 measurements, 20 measurements per image, 3 different images.

The effect of the deposition speed on the stripe pattern is the same for all χ_{DPPC} at the surface pressures studied. In each case, a slow deposition speed results in more continuous and/or wider stripes and fewer dots between the stripes (Figure 2.10). This behaviour validates the mechanism of phase nucleation and depletion proposed by Moraille and Badia.[5] The results obtained suggest that at slower speed, ample time is given to the nucleation-depletion cycle to occur, resulting in the formation of wider stripes.

The effect of χ_{DPPC} is also the same for all substrate withdrawal speeds and surface pressures examined. As the χ_{DPPC} decreases, the lines become narrower and/or broken and/or more circular domains appear. For example, the line widths for films collected at 1 mm min^{-1} near the LE-C phase transition pressure decrease from 2.2 μm to 0.3 μm when the χ_{DPPC} is reduced from 0.90 to 0.5.

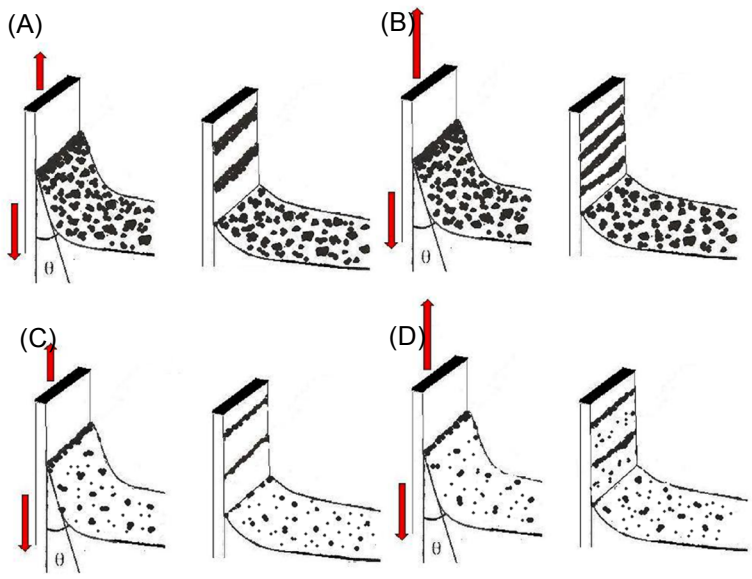

Figure 2.10 Schematic representation of the effect of the film transfer speed on the formation of the stripes. (A) Slow and (B) fast deposition speed of a film containing many DPPC-rich condensed domains; (C) slow and (D) fast deposition speed of a film containing fewer DPPC-rich condensed domains.

2.3.3 Effect of Cholesterol on the Morphology of 50:50 (mol/mol) DPPC/DLPC Films Obtained by the LB and LS Deposition Techniques

Cholesterol is a molecule that belongs to the lipid family but does not possess the usual long alkyl chains attached to a polar head. The chemical structure of cholesterol is shown in Figure 2.11. It has a steroid ring structure as the hydrophobic group and a simple alcohol (-OH) group as the hydrophilic part. Cholesterol is a lipid found in lipid membranes and plays a role in the bilayer stability and fluidity. When mixed with lipids containing saturated and unsaturated diacyl chains, it promotes the formation of a liquid- ordered phase which is characterized by translational disorder and rapid diffusion within the plane

of the bilayer, but with a high chain conformational order. [8-12] At 5 mN $m^{-1} < \pi < 10$ mN m^{-1}, pure DPPC monolayers exhibit a phase transition, where there is phase coexistance.[13] When cholesterol is added in a mole fraction above 33%, the phase separation is suppressed and a single homogeneous liquid-ordered phase is observed.[10] Cholesterol has a condensing effect on the LE phase of phospholipids and has little effect on the condensed phase of phospholipids. In DPPC/chol binary mixtures, cholesterol has a larger condensing effect at surface pressures below the phase transition pressure, and a smaller condensing effect at surface pressures above the phase transition pressure.[14] This condensing effect is also observed in DLPC/chol mixtures but is independent of surface pressure. Ternary mixtures of DPPCDLPC/chol vesicles were also examined by fourier-transform infrared-spectroscopic,[16] confocal fluorescence microscopy,[17] and by spin-label electron spin resonance[18]. In these ternary mixtures, regions of the phase diagram show coextistance of liquid ordered phase and liquid expanded phase. In giant unilamellar vesicles (GUVs) of DPPC/DLPC/chol, cholesterol mediates the solubility of DPPC into the fluid, increasing the percent coverage of the fluid phase.[19] As seen in section 2.3.1, the optimal domain size by LS to obtain the stripe pattern by LB is ~ 30 μm. To expand the surface pressure range at which the line pattern can be formed, cholesterol is added as a third component in the DPPC/DLPC mixture and films collected at 32 mN m^{-1} are examined. At 32 mN m^{-1}, DPPC/DLPC monolayers exhibit a morphology composed of large condensed domains (larger than 50 μm). Adding cholesterol might reduce the size of these domains to about 30 μm to obtain a film morphology dominated by the parallel line pattern. In this section, we study the effect of cholesterol in mole fraction (χ_{chol}) of 0.02, 0.05, 0.10 and 0.15 on the monolayer behaviour of a DPPC/DLPC (1:1 mol/mol) mixture and on the morphology of the film deposited by LS and LB at 32 mN m^{-1}.

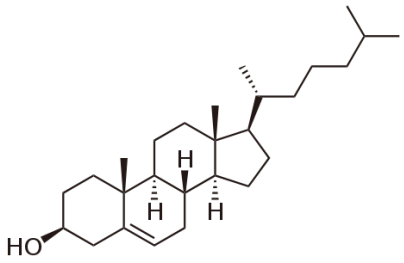

Figure 2.11 Chemical structure of cholesterol

The isotherms of ternary mixtures of DPPC/DLPC/chol are given in Figure 2.12. As the mole fraction of cholesterol is increased from 0 to 0.15, the π-A isotherms are shifted to smaller molecular areas, indicative of a more condensed state and the LE-C phase transition occurs at higher surface pressure before completely disappearing at χ_{chol} higher than 0.1.

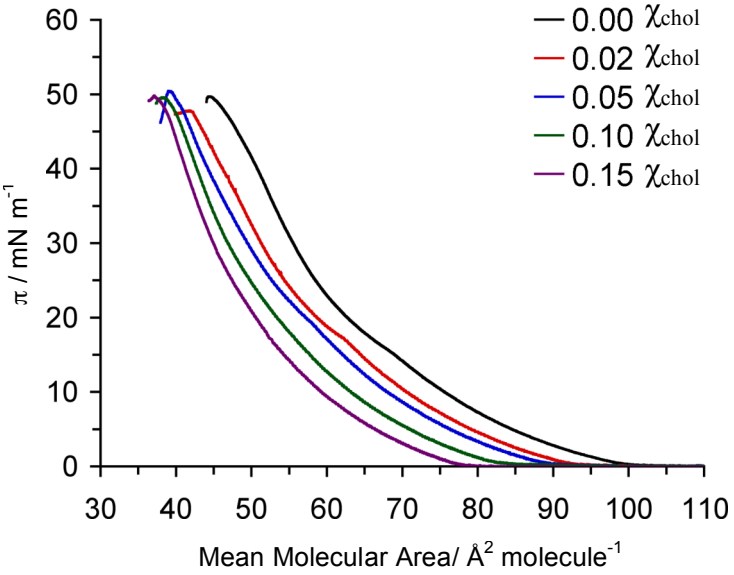

Figure 2.12 π-*A* Isotherms of DPPC/DLPC 1:1 (mol:mol) mixtures with various χ_{chol}.

	Mean Molecular area, Mma ($Å^2$ molecule^{-1}) at π = 32 mN m^{-1}
0 (100% DPPC)	48
0 χ_{chol} (100% DLPC)	63
0 (DPPC/DLPC 1 :1)	54
0.02 χ_{chol} (DPPC/DLPC 1:1)	50
0.05 χ_{chol} (DPPC/DLPC 1:1)	48
0.10 χ_{chol} (DPPC/DLPC 1:1)	46
0.15 χ_{chol} (DPPC/DLPC 1:1)	44

Table 2.3 Mean molecular area of DPPC, DLPC and DPPC/DLPC (1 :1) with various χ_{chol} at a surface pressure of 32 mN m^{-1}.

The morphology of films transferred on mica by LS and LB at 32 mN m^{-1} are presented in Figure 2.13. As little as χ_{chol} of 0.02 is sufficient to break up the larger flower domains of the LS films (Figures 2.13A and B) and produce to an extensive network of dendritic structures with almost no isolated dots. The branching of the condensed domains after the addition of cholesterol is also observed in GUVs[14], and is thought to result from a molecular anisotropy, a specific arrangement of the molecules in the solid domains, that favor prolonged boundaries. With a χ_{chol} of 0.02, the DPPC/DLPC/chol film transferred by LB exhibits a morphology composed of chiral right-handed flower-like domains with some continuous and mostly broken lines interconnecting them. As the χ_{chol} increases to 0.05, the

dendritic structures seen in the LS films break up into smaller round condensed domains of a few tens of nanometers in diameter. This type of morphology translates into smaller flower-like domains interconnected with wider and more continuous lines when transferred on mica by LB. A χ_{chol} of 0.10 and 0.15 added to DPPC/DLPC equimolar mixture (Figure 2.13G and 2.14A) lead to a homogeneous morphology of nanoscopic domains for monolayers deposited by LS. Large micron size domains are not seen. A LB deposition of these films gives rise to channels of a lower phase similar to the ones seen in Figure 2.9A and B that are oriented parallel to the direction of pulling (i.e., perpendicular to the three phase contact line), coexisting with broken parallel rods. (Figure 2.13H and 2.14B).

. Cholesterol has been shown to have a condensing effect on all saturated phospholipids, but it is unclear whether cholesterol prefers to interact with DPPC or DLPC. At 32 mN m^{-1}, DPPC has reached a condensed state (occupies a molecular area of 48 $Å^2$ $molecule^{-1}$), while DLPC still remains in its liquid expanded state (occupies a molecular area of 63 $Å^2$ $molecule^{-1}$). The addition of cholesterol promotes a liquid ordered state which reduces the interfacial line tension between the DPPC domains and DLPC matrix. Prolonged boundaries are allowed and dendritic shaped domains are observed along with the disappearance of large flower-like domains.

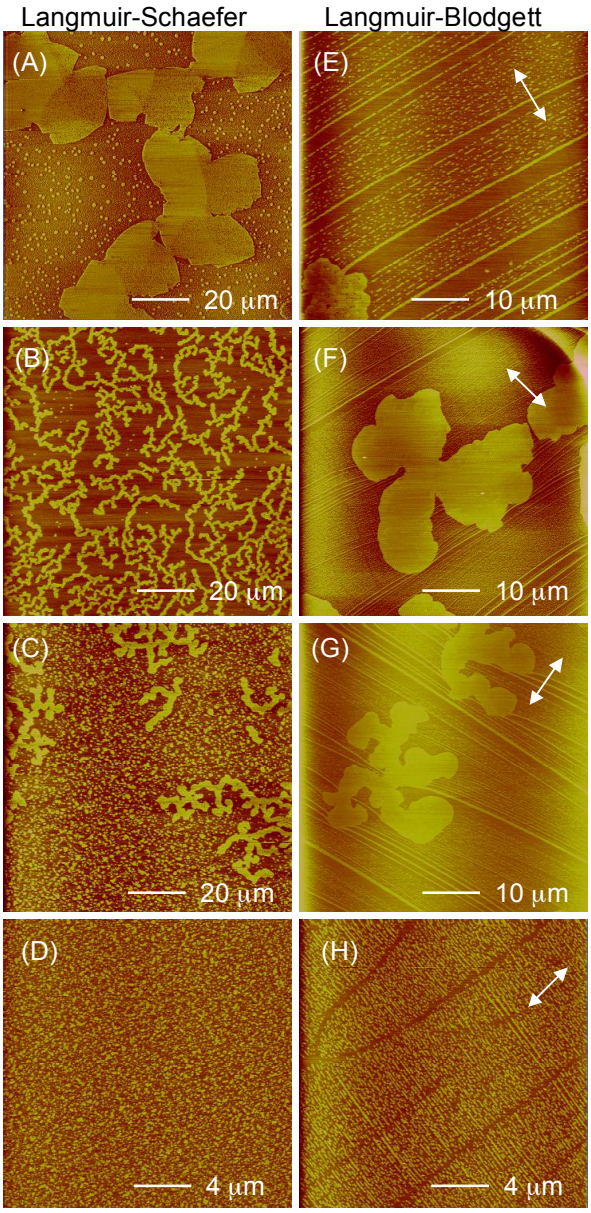

Figure 2.13 AFM height images of a DPPC/DLPC (1:1) mixture transferred at π = 32 mN m^{-1} by LS with χ_{chol} of (A) 0.00, (B) 0.02, (C) 0.05, (D) 0.10 and transferred by LB with χ_{chol} of (E) 0.00, (F) 0.02, (G) 0.05, (H) 0.10. The white arrows indicate the direction of substrate withdrawal. Note: (A) phase image is shown due to better image quality than height image.

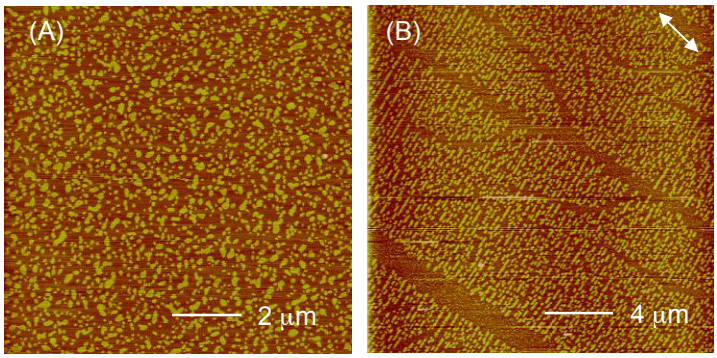

Figure 2.14 AFM height images of DPPC/DLPC (1:1) mixtures transferred at π = 32 mN m^{-1} with χ_{chol} of 0.15 (A) by LS and (B) by LB.

2.4 Conclusions

The two parameters that mainly govern the features of the parallel stripe are the domain size of the condensed phospholipid formed at the A/W interface and the speed at which the film is transferred onto the substrate by the LB technique. Morphologies at the A/W interface that give rise to continuous parallel stripes by LB transfer at 5 mm min^{-1} with little or no round condensed domains are comprised of a mixture of round domains of two different sizes, ~ 3 and 30 μm in diameter. For $0.90 \leq \chi_{DPPC} \leq 0.50$, the stripe widths could be varied from 150 to 500 nm by changing the phospholipid composition and film transfer pressure.

The addition of cholesterol drastically changed the morphology of the films. Cholesterol changes the packing behaviour of DPPC/DLPC mixtures by favouring long boundaries, but did not create circular domains in the size range of 30 μm. At a surface pressure of 32 mN m^{-1} and an equimolar mixture of DPPC/DLPC, patterns consisting of only continuous stripes were not obtained. Other molar mixtures of DPPC/DLPC and lower surface pressures should be examined to determine whether the addition of a lineactant can

favour the formation of only continuous stripes under specific conditions. Langmuir monolayers consisting of condensed domains ≤ 30 μm and a specific range of area densities are prerequisites to obtaining a predominant stripe morphology. Both suggested mechanism for stripe formation are possible. The substrate-mediated condensation describes well the formation of stripes at surface pressures below the phase transition pressure and the nucleation-depletion mechanism reflects well the phenomena observed at surface pressures above the phase transition surface pressure.

2.5 References

(1) Spratte, K.; Chi, L. F.; Riegler, H. *Europhys. Lett.* **1994**, *25*, 211.

(2) Chen, X.; Lenhert, S.; Hirtz, M.; Lu, N.; Fuchs, H.; Chi, L. *Acc. Chem. Res.* **2007**, *40*, 393.

(3) Badia, A.; Moraille, P.; Tang, N. Y. W.; Randlett, M.-E. *Int. J. Nanotechnol.* **2008**, *5*, 1371.

(4) Chen, X.; Lu, N.; Zhang, H.; Hirtz, M.; Wu, L.; Fuchs, H.; Chi, L. *J. Phys. Chem. B* **2006**, *110*, 8039.

(5) Moraille, P.; Badia, A. *Langmuir* **2002**, *18*, 4414.

(6) Sanchez, J.; Badia, A. *Thin Solid Films* **2003**, *440*, 223.

(7) Lenhert, S.; Li, Z.; Mueller, J.; Wiesmann, H. P.; Erker, G.; Fuchs, H.; Chi, L. *Adv. Mater.* **2004**, *16*, 619.

(8) McIntosh, T. J.; Simon, S. A. *Annu. Rev. Biophys. Biomol. Struct.* **2006**, *35*, 177.

(9) Sugahara, M.; Uragami, M.; Yan, X.; Regen, S. L. *J. Am. Chem. Soc.* **2001**, *123*, 7939.

(10) McConnell, H. M.; Vrljic, M. *Annu. Rev. Biophys. Biomol. Struct.* **2003**, *32*, 469.

(11) Mouritsen, O. G.; Zuckermann, M. J. *Lipids* **2004**, *39*, 1101.

(12) Yuan, C.; Johnston, L. J. *J. Microsc.* **2002**, *205*, 136.

(13) McConlogue, C. W.; Vanderlick, T. K. *Langmuir* **1997**, *13*, 7158.

(14) Kim, K.; Kim, C.; Byun, Y. *Langmuir* **2001**, *17*, 5066.

(15) Tanaka, K.; Manning, P. A.; Lau, V. K.; Yu, H. *Langmuir* **1998**, *15*, 600.

(16) Silvius, J. R.; del Giudice, D.; Lafleur, M. *Biochemistry* **1996**, *35*, 15198.

(17) Feigenson, G. W.; Buboltz, J. T. *Biophys. J.* **2001**, *80*, 2775.

(18) Chiang, Y.-W.; Shimoyama, Y.; Feigenson, G. W.; Freed, J. H. *Biophys. J.* **2004**, *87*, 2483.

(19) Korlach, J.; Schwille, P.; Webb, W. W.; Feigenson, G. W. *Proc. Natl. Acad. Sci. USA* **1999**, *96*, 8461.

Chapter 3

Phase and Interfacial Behaviour of DSDPPC & DSDLPC

3.1 Introduction

1-Palmitoyl-2-(16-(*S*-methyldithio)hexadecanoyl)-*sn*-glycero-3-phosphocholine (DSDPPC) and 1-lauroyl-2-(12-(*S*-methyldithio)dodecanoyl)-*sn*-glycero-3-phosphocholine (DSDLPC) are phopholipid analogues modified with a methyldisulfide functionality in one of their alkyl chain termini. We chose to tag a methyldisulfide group onto one of the chain ends because it is well known that alkyldisulfides form well-defined self-assembled monolayers on the surface of coin metals, such as gold, by formation of a largely covalent metal-thiolate bond.[1]

Since the modification is located at the chain end, we expected that the phase properties and stripe-pattern-forming behaviour of DSDPPC and DSDLPC would be similar to those of DPPC and DLPC. Their chemical structures are shown in Figure 3.1.

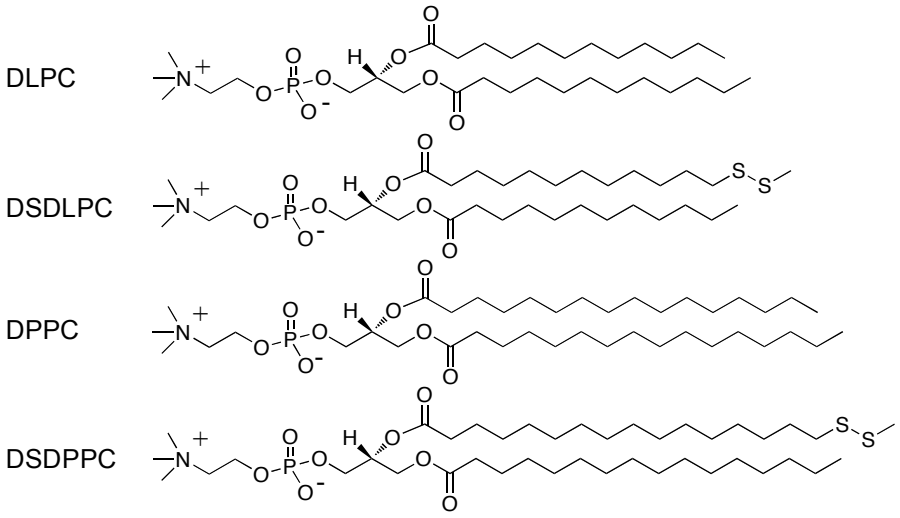

Figure 3.1 Chemical structures of DLPC, DSDLPC, DPPC and DSDPPC

3.2 Experimental Section

3.2.1 Materials

DPPC, DLPC, 1-palmitoyl-2-hydroxy-*sn*-glycero-3-phosphocholine (PHGPC) (L enantioner) and 1-lauroyl-2-hydroxy-*sn*-glycero-3-phosphocholine (LHGPC) (L enantiomer) were obtained as powders from Avanti Polar Lipids, Inc. (Alabaster, AL) and used without further purification (chemical purity > 99 %). 1-Hexadecanethiol (99 %), 16-hexadecanolide (97 %), thioacetic acid (96 %), methyl methanethiosulfonate (97 %), N,N'-dicyclohexylcarboiimide (99 %), 4-dimethylaminopyridine (≥ 99 %) and 12-hydroxydodecanoic acid (98 %) were purchased from Sigma-Aldrich Chemical Co. (St. Louis, MO).

Gold granules (99.99%) were purchased from Kitco Metals Inc. (Montreal, QC) and Ti (99.99%) granules were from Alfa Aesar. Ruby muscovite mica (ASTM Grade 2) was from B&M Mica Co., Inc. (Flushing, NY) and cleaved before use. Prime grade silicon (Si/SiO_x) type N with a resistivity of 1.000-10.000 Ω cm, thickness of 500-550 μm, and a particle per wafer pass of < 10 @ 0.3 μm (less than 10 particles greater than 0.3 μm in size found per wafer) was purchased from WaferNet Inc. (San Jose, CA). The Si/SiO_x wafers were cut into pieces that were sequentially sonicated for 5 min in the following solvents: spectrograde chloroform, spectrograde acetone and anhydrous ethanol. The Si/SiO_x pieces were dried with N_2 and exposed to a piranha solution (3:1 concentrated sulfuric acid: 30% hydrogen peroxide) for 10 min. The pieces were then dipped three times in high-purity water and kept in ethanol until use (no more than 5 h). B270 glass purchased from Esco Products, Inc., (Oak Ridge, NJ) was also used as a substrate. The glass slides were immersed in piranha for 5 min, rinsed with high-purity water, and stored in ethanol. The high-purity water (18.2 MΩ cm) used for all experiments was prepared by passing water purified by reverse osmosis through a Milli-Q Gradient System (Millipore, Bedford, MA). Its surface tension was measured to be 72.1 mN m^{-1} at 22 °C.

3.2.2 Synthesis of ω-Methyldisulfide Modified Lipids

3.2.2.1 General Methods

The synthesis of 1-palmitoyl-2-(16-(*S*-methyldithio)hexadecanoyl)-*sn*-glycero-3-phosphocholine (DSDPPC) **7** and 1-lauroyl-2-(12-(S-methyldithio)dodecanoyl)-*sn*-glycero-3-phosphocholine (DSDLPC) are outlined in Schemes 3.1 and 3.2.[2-5] The procedure given in ref. 5 was followed, with one additional step in the synthesis of DSDPPC: the synthesis of 16-hydroxyhexadecanoic acid from 16-hexadecanolide.

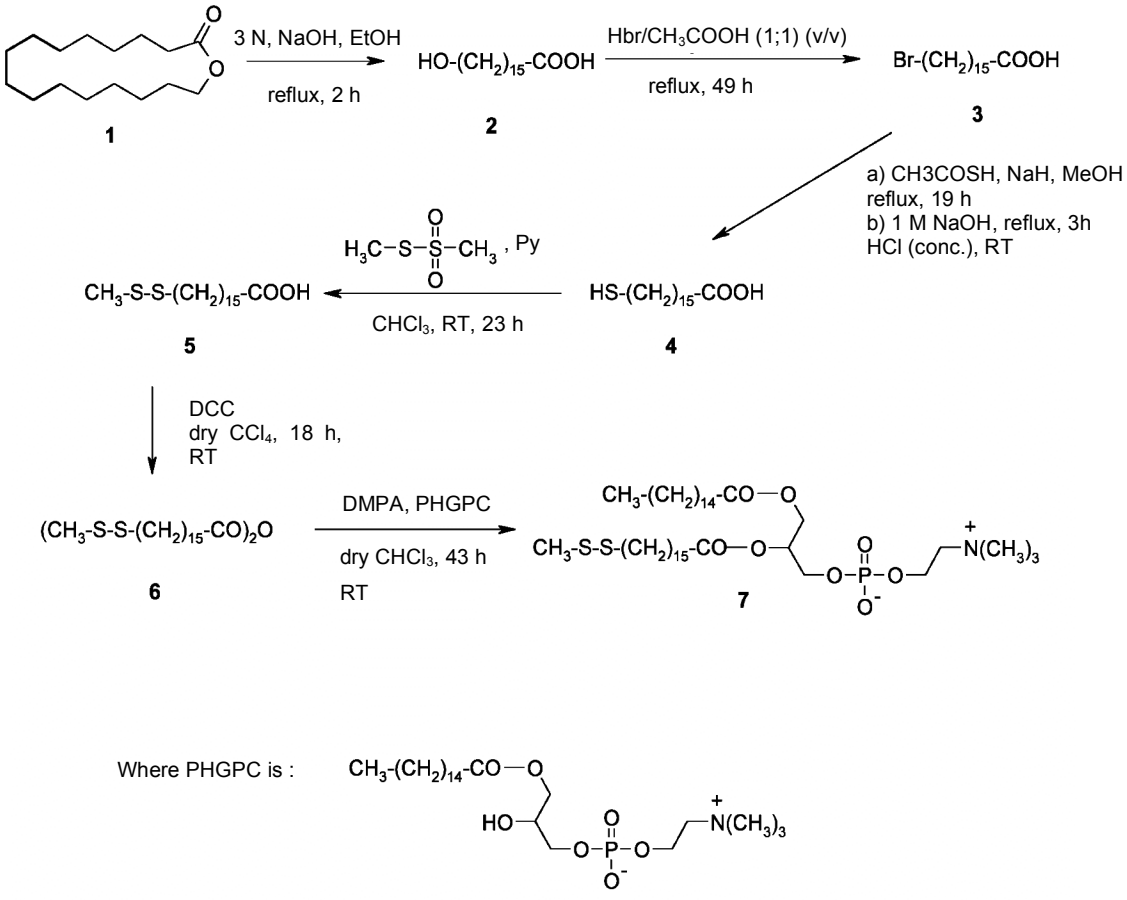

Scheme 3.1 Synthesis of DSDPPC (7)

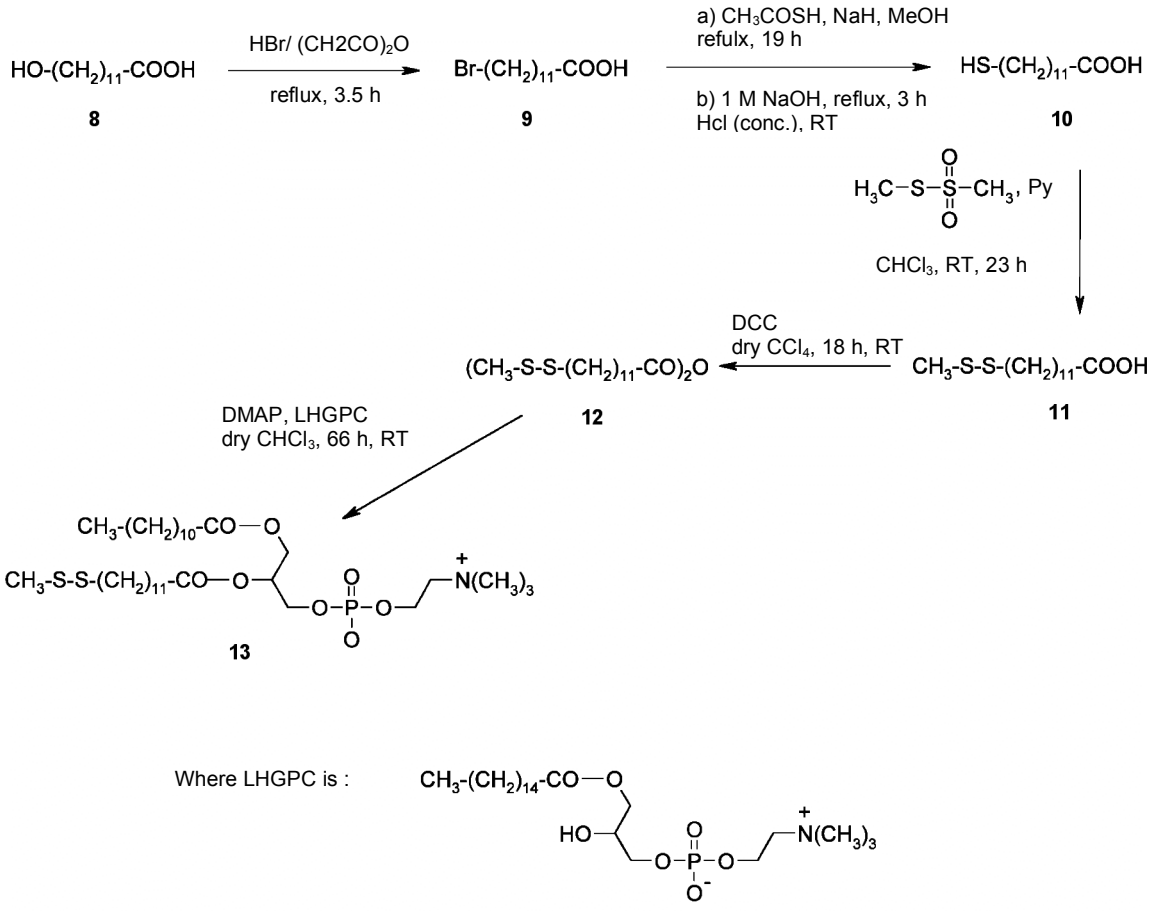

Scheme 3.2 Synthesis of DSDLPC (13)

3.2.2.2 16-Hydroxyhexadecanoic acid (2)

16-Hexadecanolide **1** (Aldrich) (8.73 g, 34.3 mmol) was dissolved in 18 mL of ethanol. To this solution, 27 mL of 3 N NaOH was added, and the reaction mixture was heated at reflux, under stirring, for 2 h. After cooling, the content of the flask was dissolved in 1:8 (v/v) mixture of ethanol and water, and neutralized with concentrated HCl. The white precipitate was separated by filtration, washed with water, and dried under vacuum. Yield = 10.5 g.

^{1}H-NMR (300 MHz, $(CD_3)_2CO$) δ (ppm): 3.51 (t, 2H, HO-CH_2-CH_2-CH_2~), 2.26 (t, 2H, ~CH_2-CH_2-CH_2-COOH), 1.65-1.4 (m, 4H, Br-CH_2-CH_2-CH_2 and ~ CH_2-CH_2-CH_2-COOH), 1.28 (s(broad), 22H, Br-CH_2-CH_2-$(CH_2)_{11}$-CH_2~).

^{13}C-NMR (75 MHz, $(CD_3)_2CO$) δ (ppm): 174.58, 62.43, 34.14, 33.74, 30.54, 30.37, 30.30, 30.28, 30.23, 30.17, 26.64, 25.62.

3.2.2.3 16-Bromohexadecanoic acid (3)

A solution of **2** (4.9 g, 0.0179 mol) was refluxed for 49 h in a 1:1 (v/v) mixture of 48% HBr and glacial acetic acid, in the absence of light. Upon cooling, the 16-bromohexadecanoic acid separated out as a white solid which was isolated by filtration and washed with water. The desired compound (5.84 g; 96.7 % yield) was obtained after recrystallization from cold hexanes.

^{1}H-NMR (300 MHz, $CDCl_3$) δ (ppm): 3.42 (t, 2H, Br-CH_2-CH_2-CH_2~), 2.36 (t, 2H, ~CH_2-CH_2-CH_2-COOH), 1.87 (m (quintet), 2H, Br-CH_2-CH_2-CH_2~), 1.65 (m, 2H, ~ CH_2-CH_2-CH_2-COOH), 1.5-1.1 (m, 22H, Br-CH_2-CH_2-$(CH_2)_{11}$-CH_2~).

^{13}C-NMR (75 MHz, $CDCl_3$) δ (ppm): 180.16, 34.38, 34.34, 33.13, 29.91, 29.87, 29.84, 29.74, 29.54, 29.35, 29.07, 28.48, 24.97.

3.2.2.4 16-Mercaptohexadecanoic acid (4)

Sodium hydride (0.9298 g, 60% w/w in mineral oil) was separated from the mineral oil in the following way: NaH was placed in a 100 mL round bottom flask and 40 mL of dry ethyl ether was added. The mixture was stirred for a few minutes and left to rest. After a few minutes, most of the ether separated from the mineral oil and was decanted away. The remaining ether was removed under reduced pressure. To the remaining NaH, 64 mL of ice-cold dry methanol was added, followed by **3** (3.3692 g, 10.04 mmol) and thiolacetic acid (1.6275 g, 21.38 mmol, 96% purity). The reaction mixture was refluxed for 19 h. After the mixture was cooled to room temperature, the thioester was hydrolyzed by adding 57 mL of 1 M NaOH (previously degassed with argon) and refluxing for 3 h, under an inert atmosphere, at room temperature (RT). The reaction mixture was cooled and poured into a

beaker containing 200 mL of water, 10 mL of concentrated HCl, and 225 mL of ethyl ether. The organic layer was separated, washed with water (2 x 100 mL), saturated NaCl solution of (100 mL), and dried over $CaCl_2$. After recrystallization from cold hexanes, 1.1829 g (41% yield) of pure material was obtained.

^{1}H-NMR (300 MHz, $CDCl_3$) δ (ppm): 2.54 (q, 2H, HS-CH_2-CH_2-CH_2~), 2.34 (t, 2H, ~CH_2-CH_2-CH_2-COOH), 1.64-1.58 (m, 4H, (HS-CH_2-CH_2-CH_2 and ~CH_2-CH_2-CH_2-COOH)(overlapped), 1.35 (t, 1H, HS-CH2-CH2~), 1.28 (s, (broad), 22H, HS-$(CH_2)_2$-$(CH_2)_{11}$-CH_2~).

^{13}C-NMR (75 MHz, $CDCl_3$) δ (ppm): 179.88, 34.29, 34.12, 29.95, 29.89, 29.81, 29.73, 29.54, 29.46, 29.36, 29.25, 24.98.

3.2.2.5 16-(*S*-methyldithio)hexadecanoic acid (5)

To a solution of **4** (1.1743 g, 4.07 mmol) in 13 mL $CHCl_3$, 0.647 mL (d=1.227, 6.10 mmol) of methyl methanethiosulfonate followed by pyridine (Py) (0.5 mL) were added. The reaction mixture was stirred at room temperature (RT) for 23 h protected from light. The chloroform was removed under reduced pressure and the residue was washed twice with cold ethanol. The solids were dissolved in hexanes at room temperature and, after recrystallization, 1.0978 g (80.6% yield) of pure material was separated.

^{1}H-NMR (300 MHz, $CDCl_3$) δ (ppm): 2.71 (t, 2H, CH_3-S-S-CH_2-CH_2~), 2.41 (s, 3H, CH_3-S-S-CH_2-CH_2~), 2.35 (t, 2H, ~CH_2-CH_2-CH_2-COOH), 1.57-1.72(m, 4H, (~S-CH_2-CH_2~ and ~CH_2-CH_2-CH_2-COOH), 1.26 (s (broad), 22H, ~S-$(CH_2)_2$-$(CH_2)_{11}$-CH_2~).

3.2.2.6 16-(*S*-methyldithio)hexadecanoic acid anhydride (6)

N,N-dicyclohexylcarbodiimide (DCC) (0.33607 g, 1.63 mmol) was dissolved separately in 5 mL of CCl_4 and was added in one portion to a solution of **5** (1.09 g, 3.25 mmol)(dried over P_2O_5) dissolved in 32 mL of CCl_4 (fresh distilled) under argon. The reaction mixture was stirred for 18 h at room temperature, protected from light. The byproduct, *N,N*-dicyclohexyl urea, was removed by filtration, and the solution was

concentrated under reduced pressure to give 1.05 g (98% yield) of **6** as a white solid. The product was characterized by IR spectroscopy that revealed the presence of the peaks characteristic to the anhydride ($\nu_{(C=O)}$ = 1740 cm^{-1} and 1810 cm^{-1}) and the absence of that characteristic to the parent carboxylic group ($\nu_{(C=O)}$ = 1698 cm^{-1}). The product was dried over P_2O_5 and stored in the freezer protected from light.

3.2.2.7 1-Palmitoyl-2-(16-(*S*-methyldithio)hexadecanoyl)-*sn*-glycero-3-phosphocholine (7)

1-Palmitoyl-2-hydroxy-*sn*-glycero-3-phosphocholine (PHGPC) (Avanti Polar Lipids) (0.3896 g, 0.79 mmol) (dried under reduced pressure for a couple of hours) was suspended in 41 mL of dry chloroform. 4-Dimethylaminopyridine (DMAP) (Aldrich) (0.3542 g, 2.89 mmol) and **6** (0.9444 g, 1.45 mmol) were added to the mixture. The reaction mixture was stirred under an inert atmosphere, in the dark. After 44 h, the reaction mixture was transferred to a separatory funnel and diluted with 18 mL of chloroform. Then, 41 mL of MeOH and 24 mL of 0.1 M HCl were added, and the lower phase was separated. The upper phase was extracted two more times with chloroform (20 mL). The organic layers were combined and the solvent was removed under reduced pressure. The product was precipitated with an acetone/ chloroform mixture (95:5) (v/v) and purified by column chromatography. (SiO_2, chloroform, chloroform/MeOH 9:1 (v/v), and chloroform/MeOH/NH_3 1:1:0.1 (v/v/v). 0.3099 g (49% yield) of pure material was obtained.

^{1}H-NMR (300 MHz, $CDCl_3$) δ (ppm): 5.23 (m, 1H, $CHCH_2OP$), 4.36-4.4 (m, 3H, $POCH_2CH_2$ and CH_2CHCH_2OP), 3.93-4.2 (m, 2H, $CHCH_2OP$), 3.88 (m, 2H, $POCH_2CH_2$), 3.47 (s, 9H, $N+(CH_3)_3$), 2.71 (t, 2H, $SSCH_2$), 2.41 (s, 3H, CH_3SS), 2.3 (q, 4H, $OOCCH_2$), 1.72-1.54 (m, 6H, $SSCH_2CH_2$ and $OOCCH_2CH_2$), 1.25 (s, 46H, ~CH_2~), 0.89 (t, 3H, $CH_3(CH_2)_{14}$~); MS (m/z, FAB+) found 812.52924, calcd for $C_{41}H_{82}N_1O_8P_1S_2$ 812.52922. Anal. Found: C, 57.32; H, 9.75; N, 1.63; S, 7.79. Calcd for $C_{41}H_{82}N_1O_8P_1S_2$: C, 60.63; H, 10.18; N, 1.72; S, 7.90.

3.2.2.8 12-Bromododecanoic acid (9)

A slight modification was done during the synthesis of 12-bromododecanoic acid compared to the synthesis of 16-bromohexadecanoic acid (**3**) for time optimization, acetic anhydride was used as a solvent instead of acetic acid.[6] During the reaction, acetic anhydride hydrolyses to acetic acid, and this insitu formation of acetic acid speeds up the reaction for a total time of 3.5 h instead of 49 h. Acetic anhydride (50 mL) was added cautiously to 48% hydrobromic acid (14 mL) followed by 12-hydroxydodecanoic acid (10) (13.34 g, 0.0616 mol). The reaction mixture was refluxed for 3.5 hours. Upon cooling, the content of the flask was poured into a large amount of water A white precipitate was formed. Ethyl ether was added and the precipitate was extracted into the organic phase. The ether layer was separated and the aqueous one was extracted one more time with ethyl ether. The combined organic layers were washed with water, dried over $MgSO_4$. The solvent was removed under reduced pressure giving 15.62 g of the desired compound (yield = 0.907) that was used for the next step without further purification.

1H-NMR (300 MHz, CDCl3) δ (ppm): 3.41 (t, 2H, Br-CH2-CH2-CH2~), 2.35 (t, 2H, ~CH2-CH2-CH2-COOH), 1.85 (m (quintet), 2H, Br-CH2-CH2-CH2~), 1.62 (m, 2H, ~ CH2-CH2-CH2-COOH), 1.5-1.1 (m, 14H, Br-CH2-CH2-(CH2)7-CH2~).

13C-NMR (75 MHz, CDCl3) δ (ppm): 180.34, 34.35, 33.10, 29.73, 29.68, 29.65, 29.5, 29.32, 29.04, 28.45, 24.94

3.2.2.9 12-(*S*-methyldithio)dodecanoic acid anhydride (12)

The same procedure as described for **4**, **5** and **6** was used for the synthesis of **10**, **11** and **12** by using the dodecanoic acid instead of hexadecanoic acid.

3.2.2.10 1-Lauroyl-2-(12-(*S*-methyldithio)dodecanoyl)-*sn*-glycero-3-phosphocholine (DSDLPC) (13)

1-Lauroyl-2-hydroxy-*sn*-glycero-3-phosphocholine (0.9808 g, 1.82 mmol) (dried under reduced pressure for a couple of hours) was suspended in 42 mL of dry chloroform. 4-Dimethylaminopyridine (0.4447 g, 3.64 mmol) and **12** (0.400 g, 0.91 mmol) were added

to the mixture. The reaction mixture was stirred under an inert atmosphere, in the dark. After 66 h, the reaction mixture was transferred to a separatory funnel and diluted with 22 mL of chloroform. Then, 50 mL of MeOH and 30 mL of 0.1 M HCl were added, and the lower phase was separated. The upper phase was extracted two more times with chloroform (20 mL). The organic layers were combined, and the solvent removed under reduced pressure. The solid residue was purified by column chromatography. (SiO_2, chloroform, chloroform/MeOH 9:1 (v/v) and chloroform/MeOH/NH_3 1:1:0.1 (v/v/v). 0.4007 g (31% yield) of pure material was recovered.

^{1}H-NMR (300 MHz, $CDCl_3$) δ (ppm): 5.2 (m, 1H, $CHCH_2OP$), 4.2-4.41 (m, 3H, $POCH_2CH_2$ and CH_2CHCH_2OP), 4.0-4.2 (m, 1H, CH_2CHCH_2OP), 3.94 (m, 2H, $CHCH_2OP$), 3.81 (m, 2H, $POCH_2CH_2$), 3.37 (s, 9H, $N+(CH_3)_3$), 2.704 (t, 2H, $SSCH_2$), 2.407 (s, 3H, CH_3SS), 2.28 (q, 4H, $OOCCH_2$), 1.72-1.50 (m, 6H, $SSCH_2CH_2$ and $OOCCH_2CH_2$), 1.25 (s, 30H, ~CH_2~), 0.88 (t, 3H, $CH_3(CH_2)_{14}$~)

3.2.3 Preparation of Vesicles and Determination of Phase Transition Temperature

3.2.3.1 Turbidity Measurements

Solutions of 1 mg/ml of DPPC and DSDPPC were prepared in MilliQ water. Multilamellar vesicles (MLVs) were prepared by 5 freeze/thaw cycles (freeze in liquid nitrogen, thaw at 50-60 °C for 10 min in water bath without stirring followed by vortexing). The viscous solutions were then diluted to 0.3 mg mL^{-1} to fill a 1 cm path cuvette. A Varian spectrophotometer (Cary UV-Vis 1 BIO) with a variable temperature cell holder was used. The absorbance at 450 nm was recorded as the temperature was ramped from 25 to 55 °C at a rate of 0.1 °C min^{-1}. The turbidimetric phase transition temperatures, the pre-transition temperature (T_p) and the main phase transition temperature (T_m), are defined as the inflection points in the absorbance versus temperature profiles.

3.2.3.2 Differential Scanning Calorimetry (DSC)

Thermograms were recorded from 25 ºC to 52 ºC at a heating rate of 20 ºC h^{-1} (0.33 ºC min^{-1}) with a prescan equilibration time of 30 min using a Microcal VP-DSC. The vesicles were prepared from a 1 mg mL^{-1} solution by 5 freeze/thaw cycles (same as for the turbidity measurements). The transition temperatures were determined at the peak maximum. The Bartlett assay was used to determine the concentration of phospholipids in the vesicles. The enthalpy of transition (ΔH) was calculated using the following equation:

$$\Delta H = \mathrm{K}A$$

where K is the calorimentric constant, specific to each instrument, and A is the area under the curve measured with a simple linear baseline correction.

Bartlett assay for phospholipid quantification[7]

The following reagent were prepared: 100 mL of 3.2 mM monopotassium phosphate (KH_2PO_4), 1 mL of 0.1 g mL^{-1} of sodium metabisulfite ($Na_2S_2O_5$), 10 mL of 0.02 g/mL of ammonium molybdate ($H_8MoN_2O_4$) and 1 mL of 0.1 g/mL of ascorbique acid ($C_6H_8O_6$). From the KH_2PO_4 stock solution, serial dilution were performed to obtain the following concentrations of: 0, 0.4, 0.8, 1.6, 3.2 μmol mL^{-1}. Three aliquots of 20 μL were taken from each vesicle suspension and pipetted into pyrex tubes (6 tubes). 20 μL of each standard solution was pipetted into pyrex tubes (5 tubes). To all the tubes containing the standard solutions and vesicle suspension, 120 μL of sulfuric acid was added and the tubes were vortexed. Then 20 μL of hydrogen peroxide was added and the tubes were vortexed once again. The tubes were heated at 200 °C for 10 min., followed by cooling to room temperature. 1340 μL of milliQ water was added into each tube and the samples were vortexed. 40 mL of sodium metabisulfide solution (0.1 g/mL) was added to each tube, vortexed, and heated at 100 °C for 5 min. After cooling to room temperature, 400 μL of ammonium molybdate was added to each tube and vortexed, followed by the addition of 40 μL of ascorbic acid solution and vortexed. The tubes were heated at 100 °C for exactly 10

min. A blue color developed in the standard solutions and vesicle suspension samples. After cooling to room temperature, the absorbance of each solution/suspension was measured at 820 nm using a Varian spectrophotometer (Cary UV-Vis 1 BIO). From the standards absorbance measurements, a calibration curve was constructed, and the phosphorus content of each vesicle suspension was determined from the calibration curve.

3.2.4 Preparation of Substrate for Solid-Supported Films

3.2.4.1 Metal Vapor Deposition by Resistive Thermal Evaporation

A VE-90 thermal evaporator equipped with a quartz crystal deposition monitor (Thermionics Vacuum Products, Port Townsend, WA) and a rotating sample stage was used to prepared gold substrates. First, a titanium adhesion layer of 1.2 nm thickeness was evaporated at a rate of 0.1 Å s^{-1} onto clean silicon or B270 glass, followed by a 48 nm or 70 nm thick gold layer deposited at a rate of 0.3 Å s^{-1}. The metal evaporation process was initiated once a base pressure of < 5.5 x 10^{-7} Torr was attained and there was no cooling or heating of the substrates.

3.2.5 Preparation of Phospholipid Films

3.2.5.1 LB and LS Film Deposition

A KSV 3000 standard trough (surface area of 768 cm^2, aspect ratio of width:length of 3.1) equipped with a Pt Wilhelmy plate sensing device (KSV Instruments, Helsinki, Finland) was used to record π-*A* monolayer isotherms and carry out Langmuir-Blodgett (LB) or Langmuir-Schaefer (LS) film transfer. The subphase temperature was maintained at 20.0 ºC (± 0.5 ºC) using an Isotemp 1006D circulation bath (Fisher Scientific). The subphase volume used was 1.25 L. Solutions of DPPC, DLPC, DSDPPC and DSDLPC of 1 mM concentration were prepared using spectrograde chloroform. Monolayers were formed by spreading 90 - 100 μL of lipid solution on the water surface of the trough and the solvent was allowed to evaporate for 15 min. The phospholipid molecules were

symmetrically compressed at a rate of 1 $Å^2$ $molecule^{-1}$ min^{-1} up to the desired deposition pressure. After a barrier stabilization time of about 20 min, the monolayer films were deposited onto mica or Si/SiO_x at a constant surface pressure by LB or LS deposition. In the LB deposition, the mica or Si/SiO_x was pulled vertically upward from the water subphase through the A/W interface at a rate of 5 mm min^{-1}. Transfer ratios between 1 and 1.3 were obtained. For films prepared on gold by LB, the gold slides were vertically lowered from air through the A/W interface at a rate of 0.5 mm/min and remained in the water subphase until they were removed for an analysis. Films of DSDPPC were also prepared on gold by the LS method. The gold surface, which lies parallel to and above the A/W interface, is brought into contact horizontally with the floating monolayer for a period of time, pushed through the A/W interface, and kept in the water subphase until an analysis was performed.

3.2.5.2 Self-Assembled Monolayers (SAMs)

Gold substrates were immersed into a solution of 1 mM of DSDPPC or hexadecanethiol in anhydrous ethanol for 1 or 20 h. After incubation, the SAMs were rinsed with 100% ethanol and dried under a stream of nitrogen (N_2).

3.2.6 Characterization Techniques

3.2.6.1 Brewster Angle Microscopy (BAM)

Imaging at the A/W interface was performed using an I-Elli2000 imaging ellipsometer (Nanofilm Technologies GmbH, Göttingen, Germany), equipped with a 50 mW Nd:YAG laser (λ = 532 nm) combined with a 702 BAM balance (area of 700 cm^2, length : 70 cm, aspect ratio of 7) from Nima Technology Ltd. (Coventry, England). A volume of 90 or 100 μL of lipid solution (1 mM in chloroform) was spread at the A/W interface, and a wait time of 15 min was applied before starting the barrier compression.

Monolayers were symmetrically compressed at a rate of 4 mm min^{-1} (1 $Å^2$ $molecule^{-1}$ min^{-1}).

3.2.6.2 AFM Imaging

AFM imaging was performed as described in Section 2.2.3.

3.2.6.3 Spectroscopic Ellipsometry

DSDPPC were deposited on Si/SiO_x at 18 mN m^{-1} (or 16 mN m for DPPC) and all four lipids (DPPC, DSDPPC, DLPC, DSDLPC) were also deposited on Si/SiO_x at 32 mN m^{-1} for the ellipsometric measurements. All measurements were performed in air at an incident angle of 75° and a wavelength range of 370–1000 nm on a multiwavelength ellipsometer equipped with a quartz tungsten-halogen lamp and rotating compensator (Model M-2000V, J.A. Woollam Co, Inc., Lincoln, NE). The plots of amplitude ratio (ψ) and phase difference (Δ) versus wavelength (λ) were fit using a three-layer Si/SiO_x phospholipid model as previously described.[8] The phospholipid monolayers were modeled as transparent Cauchy layers and values of A = 1.44, B = 0.0045, and C = 0 (n = 1.456 and k = 0) were used for the Cauchy dispersion equation:[9-11]

$$n(\lambda/\mu m) = A + B/\lambda^2 + C/\lambda^4 \qquad \text{(Eq. 3.1)}$$

3.2.6.4 X-ray Photoelectron Spectroscopy (XPS)

The X-ray photoelectron spectra were obtained using an ESCALAB 3 MKII spectrometer (VG Scientific) equipped with a MgKα source. A take-off angle of 70° from the surface was used. The survey spectra were recorded with a power of 206 W (12 kV, 18 mA), a 100 eV pass energy, and steps of 1.0 eV. The high-resolution scans were acquired with a pass energy of 20 eV and steps of 0.05 eV. The size of the area analyzed was 2 mm x 3 mm. The spectra were referenced to C1s at 286.6 eV. A Shirley background was applied to the high-resolution spectra and the peaks were fit using a symmetric Voigt function with a variable Lorenzian-Gaussian ratio. The S2p spectra were fit using doublets,

each doublet peak having a FWHM of 1.45, a spin-orbit splitting of 1.18 eV, and a height ratio ($S2p_{3/2}/S2p_{1/2}$) of 2:1.

3.2.6.5 Reductive Desorption of SAMs

The reductive desorption of alkylthiolates was performed using a three electrode teflon cell equipped with a Pt wire counter electrode and a Ag/AgCl (3 M NaCl, Bioanalytical Systems) reference electrode in 0.1 M KOH solution. Gold slides modified with DSDPPC or hexadecanethiolate SAMs served as the working electrode. The 0.1 M KOH electrolyte solution was purged with nitrogen before the electrochemical measurements. The cyclic voltammograms (CVs) were acquired using an Epsilon potentiostat (Bioanalytical Systems, Inc., West Lafayette, IN) at a potential scan rate of 20 mV s^{-1}.

3.2.6.6 Attenuated Total Reflection Infrared Spectroscopy (ATR-IR)

The ATR-IR spectra were obtained on a VARI GART spectrometer from Harrick using a germanium crystal and polarized light. For each spectrum, 512 scans were performed using a spectral resolution of 4 cm^{-1}. The substrate used for the ATR-IR measurements was Au (70 nm)/Ti (1.2 nm)/B270 glass slide (2 x 2.5 cm). The monolayer-covered Au slide was pressed against the germanium crystal for the spectral acquisition.

3.3. Results and Discussion

3.3.1 Comparison of the Vesicle Phase Behaviour

Two different techniques were used to determine the phase transition temperatures of DPPC and DSDPPC vesicles: DSC and UV-Vis absorption. In DSC, the temperature is increased at a specific rate and the heat required to maintain the reference and sample at each temperature is monitored. When a transition occurs, more or less heat will be needed to maintain the temperature depending on the process being endothermic or exothermic. For example, melting is endothermic and will require more heat to increase its temperature at the same rate as the reference, which translates into a peak. The peak maximum is the phase transition temperature. UV-Vis turbidity measurements can also be used to determine the phase transition temperature of lipid vesicles. Light scattering of the lipid dispersion is a function of the refractive index of the lipid. When DPPC undergoes a gel(S)-to-liquid crystalline phase transition, a sharp change in refractive index occurs and hence the turbidity decreases.[12] Turbidity is defined by:

$$\tau l = \ln I_0/I \qquad \text{(Eq. 3.2)}$$

where I is the intensity of the transmitted light, I_0 is the intensity of the incident light, l is the length of the light path and τ is turbidity. Turbidity is therefore an apparent absorbance.

DPPC undergoes two well-documented thermotropic phase transitions.[13] At the pre-transition (lower temperature), the DPPC bilayer passes from a lamellar gel (L_{β}) phase to a ripple (P_{β}) phase. At higher temperature, DPPC undergoes a main transition from the P_{β} phase to the liquid crystalline (L_{α}) phase involving melting of the acyl chains. The pre-transition (T_p) and main transition (T_m) temperatures of DPPC and DSDPPC measured by DSC and UV-Vis turbidity are compared in Figure 3.2. The phase transition temperatures obtained using both methods are summarized in Table 3.1.

No pre-transition was detected for DSDPPC by DSC or turbidity. The T_m of DSDPPC is 2-4 ºC higher then that of DPPC. The absence of a pre-transition suggests a restriction in cooperative disordering due to the molecular assymmetry caused by the methyldisulfide group and its bulkiness. The main transition enthalpy (ΔH) of DSDPPC (41.9 kJ mol^{-1}) was found to be larger than that of DPPC (31.0 kJ mol^{-1}). The higher ΔH of DSDPPC compared to DPPC can be due to either a more ordered and/or stable liquid crystalline phase through intermolecular interactions, presumably through -$SSCH_3$ groups, or a less stable lamellar gel phase due to the bulkier –$SSCH_3$ group and assymetric chains. According to Langmuir isotherms of DSDPPC, the molecules occupy a larger area than DPPC throughout the compression suggesting that a more disordered lamellar gel phase is more probable. The enthalpy of the DPPC phase transition is well within the range of literature values. The enthalpy values for the main transition of DPPC vary depending on the vesicle preparation method that will result in unilamellar vesicles or multilamellar vesicles of various sizes. The ionic strength of the buffer in which the vesicles are prepared will also affect the enthalpy.

We did not perform DSC or turbidity measurements of DLPC vesicles because the reported T_m of DLPC (T_m = - 1 °C)[13] is below the freezing point of water and would require the use of different experimental conditions than those of DPPC and DSDPPC (i.e., use of lower freezing point salt solution). We, however, expect the T_m of DSDLPC to be similar to that of DLPC.

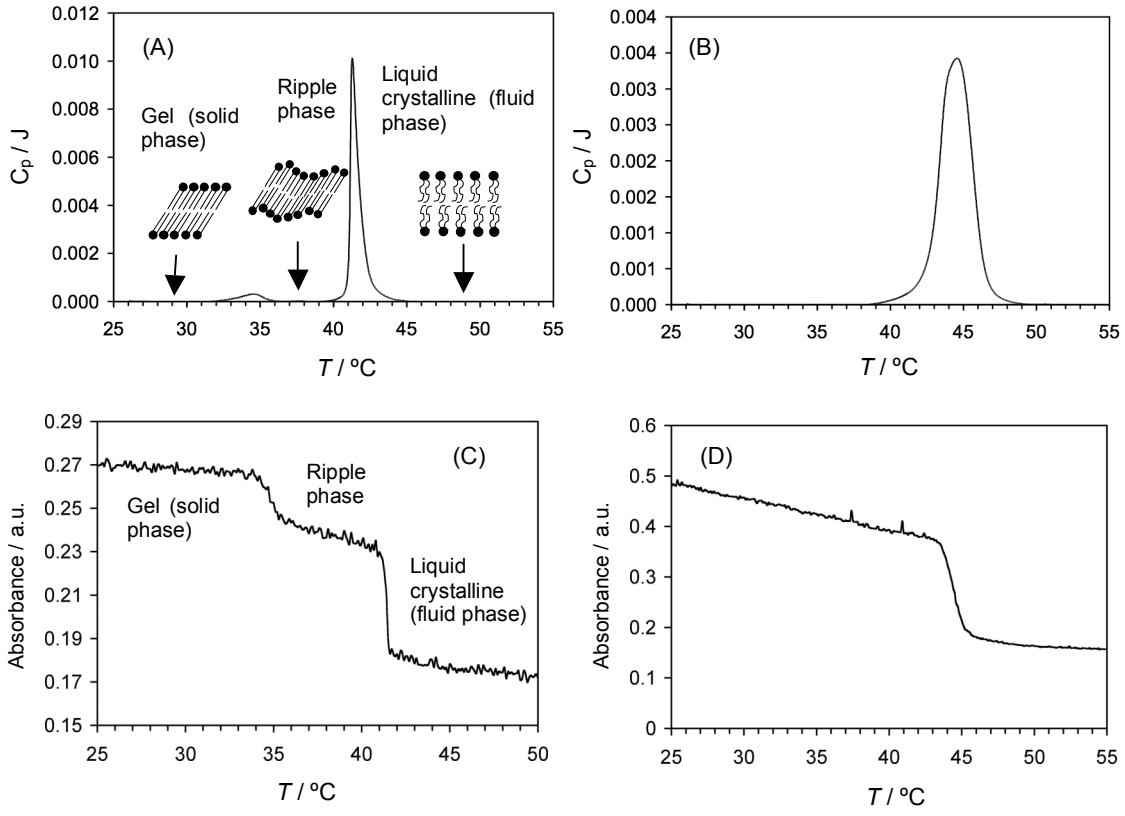

Figure 3.2 DSC and turbidometric thermograms of DPPC (A, C) and DSDPPC (B, D).

Table 3.1 Transition temperatures of DPPC and DSDPPC determined by DSC and UV-Vis absorption.

Method	T_p (ºC)	T_m (ºC)	ΔH (kJ mol^{-1})
DSC (ULVs) DPPC (n=1)	34.3	41.4	31.0
Literature[10]	34.9 ± 0.6	41.1 ± 0.5	35 ± 4
DSDPPC (n=1)	-	43.4	41.9
Turbidity – MLV DPPC (n=3)	35.2 ± 0.2	41.6 ± 0.2	
DSDPPC (n=1)	-	45.6	

3.3.2 Langmuir Monolayer Phase Properties

The π-*A* isotherms of the modified and unmodified dialkylphosphatidylcholines at 20 °C are shown in Figures 3.3 and 3.5. Overall, the molecular packing densities of DSDPPC and DSDLPC monolayers in the condensed and fluid phases, respectively, are significantly different from those of DPPC and DLPC. The functionalized analogues adopt more expanded states at the A/W interface due to the bulkier $–SSCH_3$ versus $–CH_3$ group. First, the onset area (A_{onset}) of DSDPPC (121 ± 2 $Å^2$ $molecule^{-1}$) is larger than that of DPPC (92 ± 1 $Å^2$ $molecule^{-1}$) (Figure 3.3). Second, the mean limiting area (A_{lim}), extrapolated from the linear portion of the isotherm before the collapse, is 69 ± 3 $Å^2$ $molecule^{-1}$ for DSDPPC and 52 ± 1 $Å^2$ $molecule^{-1}$ for DPPC. The larger onset and limiting areas for DSDPPC suggest that the longer $-SSCH_3$ terminated chain of the DSDPPC causes its packing to be less ordered than DPPC. Both DPPC and DSDPPC undergo a liquid-expanded-to-condensed (LE-C) transition, as demonstrated by the characteristic plateaus. The onset of this phase transition occurs at higher surface pressure for DSDPPC (~ 6 mN m^{-1}) compared to DPPC (~ 4 mN m^{-1}). The DPPC transition is very sharp (flat plateau) while the DSDPPC transition occurs over a larger range of surface pressures (sloping plateau). These differences in the LE-C phase transition behaviour are consistent with the DSDPPC adopting a more disordered state then DPPC at the A/W interface. Third, DSDPPC exhibits a second distinct plateau at ~25 ± 2 mN m^{-1}. The assignment of this plateau to the start of film collapse will be discussed further in section 3.3.3 and 3.3.4 below. Under our experimental conditions, the collapse pressure of DPPC occurs at 57 ± 1 mN m^{-1}.

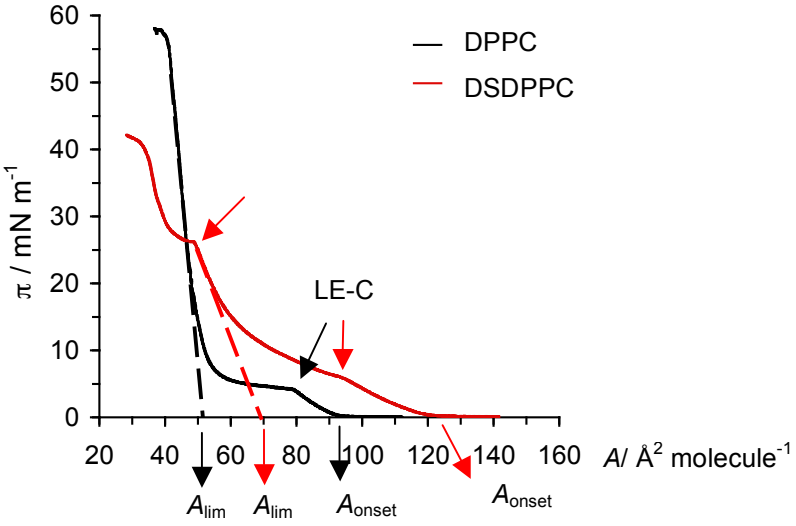

Figure 3.3 Isotherms of pure DPPC and DSDPPC at 20.0 °C, using the KSV3000 standard trough.

In general at higher surface pressures, the transition observed is one in which the alkyl chains of the amphiphile untilt (tilted to untilted phase transition), and usually appears as a break in the isotherm (change of slope) rather than a shoulder.[14] A shoulder or a plateau-like kink at high surface pressure can be indicative of a monolayer-to-multilayer phase transition.[15]

The isotherm of DSDPPC was also recorded by Ihalainen *et al.*[5] (Fig. 3.4A). A comparison between the DSDPPC isotherms shows similar molecular area onset and similar collapse pressures. But significant differences are noted. First, we detect the LE-C transition at a lower surface pressure (6 vs 10 mN m^{-1}) than the transition recorded by Ihalainen, which occurs at a higher surface pressure. Second, the transition observed at 25 mN m^{-1}, is absent in their isotherm. Many reasons can explain these differences such, as different purity level of DSDPPC and different Langmuir film experimental conditions. Both reasons can contribute to the differences observed. DSDPPC was synthesized by both

laboratories since it is not commercially available. Under the same experimental conditions, DPPC isotherms (from the same source, Avanti Polar Lipids) should be reproducible. The DPPC isotherm recorded by Ihanalainen is compared to the one obtained in this work and differences are noted (Fig. 3.4B). Hence, we can infer that the LB experimental conditions such as room temperature and humidity, subphase level, compression speed are different in each research lab. The DPPC isotherm presented in Inhalainen's paper (Fig. 3.4B) exhibits a much lower LE-C transition (~ 2.5 mN m^{-1}).

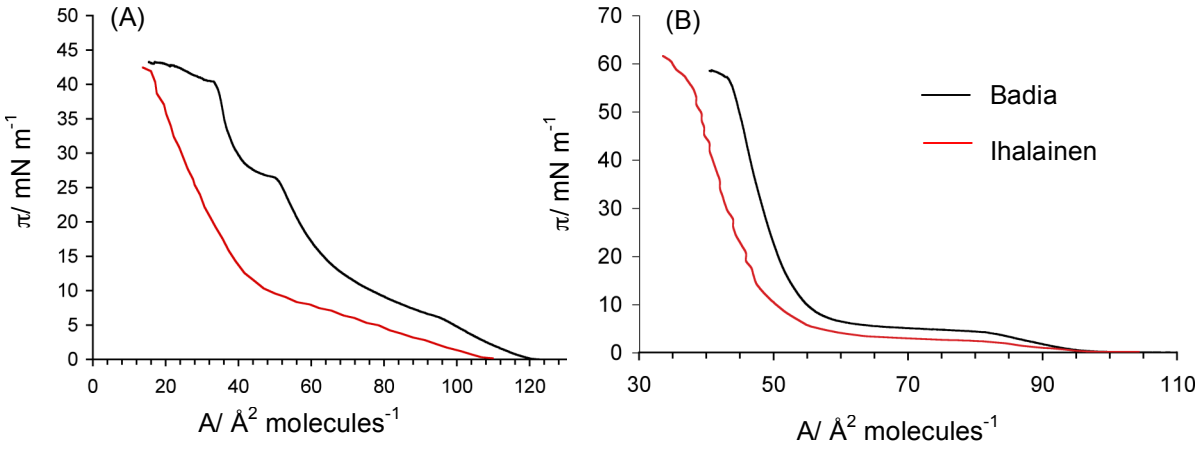

Figure 3.4 Isotherm comparison of (A) DSDPPC and (B) DPPC at 20.0 ± 0.4 ºC from Inhalainen and Badia's research group (reproduced from ref. 5)

The onset area of DSDLPC is larger than that of DLPC. As in the case of DSDPPC, the DSDLPC monolayer (Figure 3.4) exists in a significantly more expanded state than DLPC at any given surface pressure, except between 35 and 40 mN m^{-1}, where the molecular area of DSDLPC is smaller or equal to that of DLPC. At their collapse pressure, the molecular areas of DSDLPC and DLPC are 53 and 54 $Å^2$ $molecule^{-1}$ respectively. Compared to its unmodified analogue, DSDLPC has a lower collapse pressure.

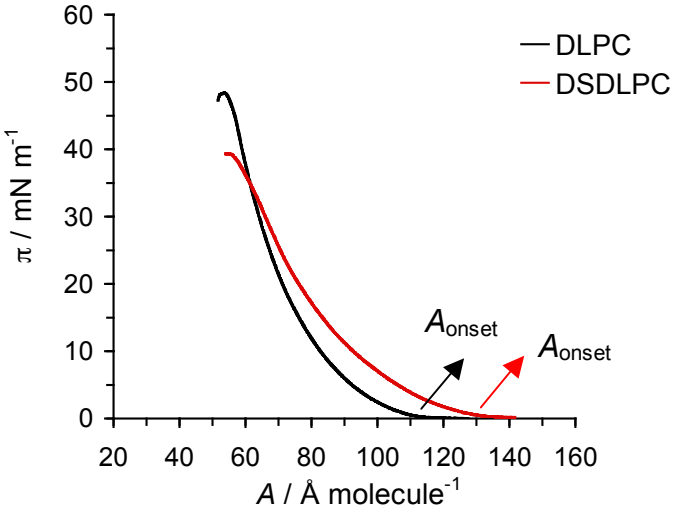

Figure 3.5 Isotherms of DLPC and DSDLPC at 20.0 °C

Table 3.2 Summary of DPPC, DSDPPC, DLPC and DSDLPC isotherm characteristics

	A_{onset} (Å^2 molecule^{-1})	Collapse pressure (mN m^{-1})	Molecular area at collapse (Å^2 molecule^{-1})
DPPC (n=3)	92 ± 1	57 ± 1	38 ± 2
DSDPPC (n=5)	121 ± 2	25 ± 2	49 ± 1
DLPC (n=2)	108 ± 1	48 ± 1	54 ± 1
DSDLPC (n=3)	134 ± 1	40 ± 1	53 ± 1

3.3.3 Visualization at the Monolayer A/W Interface Using BAM

Brewster angle microscopy (BAM) uses polarized light to visualize the domain structures formed in real-time at the A/W interface, allowing one to better characterize Langmuir films on the micron scale before their deposition onto solid substrates.[16,17] The film transfer process itself can alter the shape of the domains formed at the A/W interface and it is therefore important to correlate the phase structure of the LB films with those of the precursor Langmuir monolayers. The series of images acquired during monolayer compression are presented in Figures 3.6 and 3.7.

For DPPC (Figure 3.6), domains start to form at pressures slightly below the LE-C transition pressure (i.e. image acquired at 2.9 mN m^{-1}) and grow in number and size as the film is compressed through the transition region. The DPPC domains consisting of interlocked spirals (triskel-shaped) are very homogeneous in size (i.e. image acquired at 5.9 mN m^{-1}). DPPC has a chiral center and two enantiomers exist. The L-enantiomer was used exclusively here, giving rise to triskelians whose arms twist counter-clockwise. At $\pi \geq 10$ mN m^{-1}, a continuous film of condensed phase is observed by BAM. The BAM images presented in Figure 3.6 for DPPC are consistent with those already published.[18]

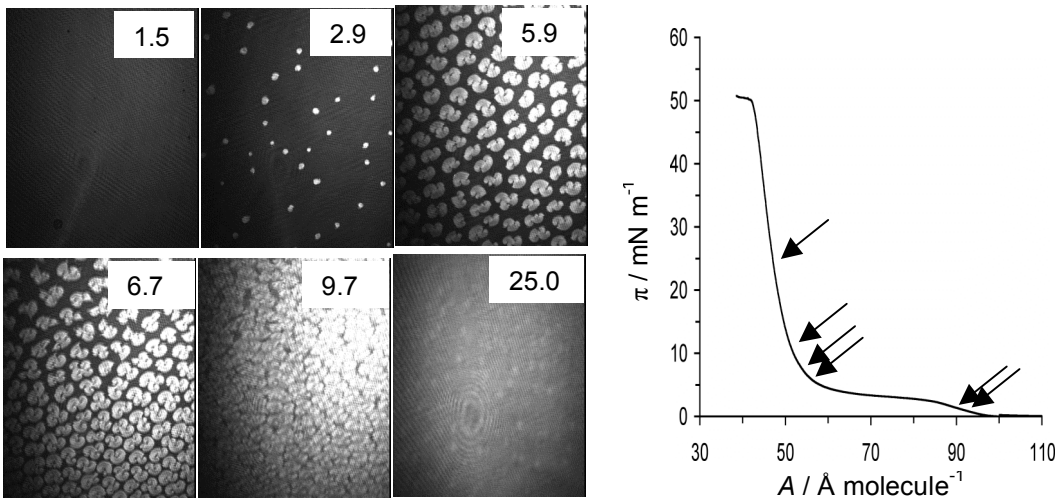

Figure 3.6 BAM images and corresponding π-*A* isotherm of DPPC acquired at 20 °C on a pure water subphase. The arrows in the π-*A* isotherm correspond to the surface pressure of the images shown on the left.

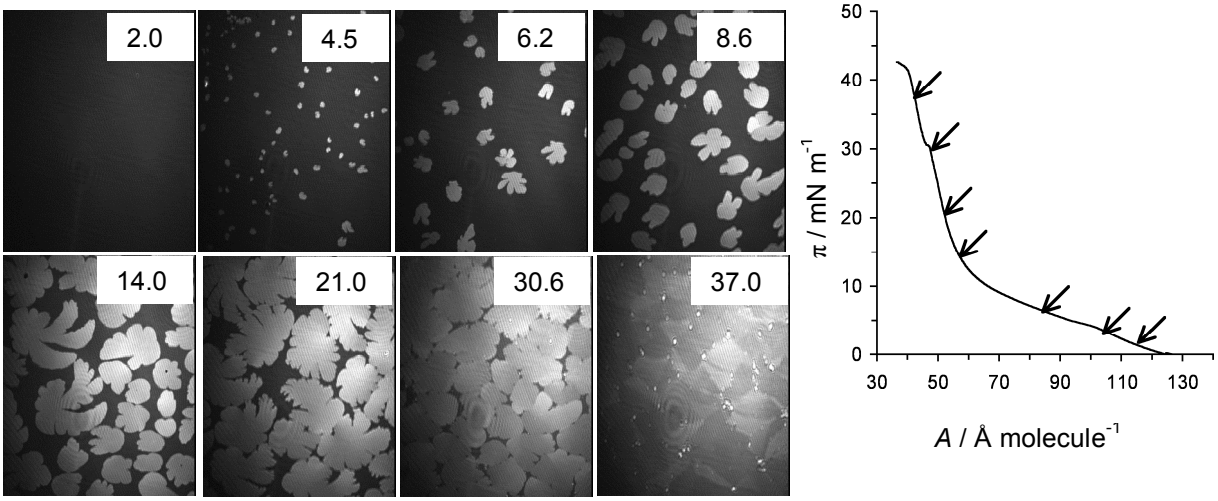

Figure 3.7 BAM images and corresponding π-*A* isotherm of DSDPPC acquired at 20 ºC on a pure water subphase. The arrows in the π-*A* isotherm correspond to the pressures of the images shown on the left.

The morphology of pure DSDPPC (L-enantiomer) monolayers (Figure 3.7) is different from that of DPPC. Again, domains of condensed phase appear just below the LE-C transition pressure (i.e., image at 4.5 mN m^{-1}). The domain shape resembles branched flowers. These flower-like domains grow in size over a large range of surface pressure, from the onset of the LE-C (π = 5 mN m^{-1}) transition up to a surface pressure of about 20 mN m^{-1}. The effect of intermolecular chiral forces is not as pronounced in the DSDPPC condensed phase compared to the DPPC condensed domains. In the BAM image collected at 14 mN m^{-1} in Figure 3.7, only two big domains show left handedness. This can be explained either by the presence of impurities or steric hindrance from the bulky -$SSCH_3$ groups diminishing intermolecular chiral forces. After 20 mN m^{-1}, the domains only seem to be pushed together until they all come into contact and collapse near a surface pressure of 30 mN m^{-1}. The halt in domain growth suggest that at 20 mN m^{-1}, all the DSDPPC molecules are part of a condensed domains and each domain reached a favorable equilibrium which prevents them from fusing together. It is only around the collapse, in a very narrow range of pressure, that a homogenous condensed film is formed. After the collapse, which occurs at $\pi \sim$ 30 mN m^{-1}, aggregates start forming (2D-3D transition) along domain edges (e.g. image acquired at 37.0 mN m^{-1}). The BAM image of the DSDPPC monolayer compressed to 37 mN m^{-1} (Figure 3.7) exhibits contrast in reflectivity between the large domains. This contrast is not due to a difference in thickness but reflects an anisotropy in the molecular tilt orientation of the phospholipids.[16,18] At best, the lateral resolution of our BAM instrument is 2 μm, which is not sufficient to resolve the structure at domain boundaries. We therefore turned to AFM imaging of LB films to investigate the internal structure of the aggregates formed at film collapse.

3.3.4 Langmuir-Blodgett (LB) and Langmuir-Schaefer (LS) Films

LB and LS films of the phospholipids were investigated using different surface analytical techniques. Phospholipid monolayers were deposited onto Si/SiO_x or mica substrate to further characterize the physical properties of the films. These conventional

films were prepared by vertical (LB) deposition. The substrate was pulled out of the subphase through the compressed film floating at the A/W interface. In this geometry, the phosphocholine head groups are in contact with the substrate and their alkyl tails are exposed to air (Figure 3.8A). LB, LS, and self-assembled (SA) films of DSDPPC were also prepared on Au substrates to obtain a covalently bound film equivalent to the monolayers of alkylthiolates on Au. By LB, the Au substrate (suspended in air above the A/W interface) was dipped vertically into the subphase through the floating film. By LS, the Au substrate was positioned parallel to the A/W interface and was brought into contact with the compressed film. The resulting geometry of the films deposited on Au are represented in Figure 3.8B.

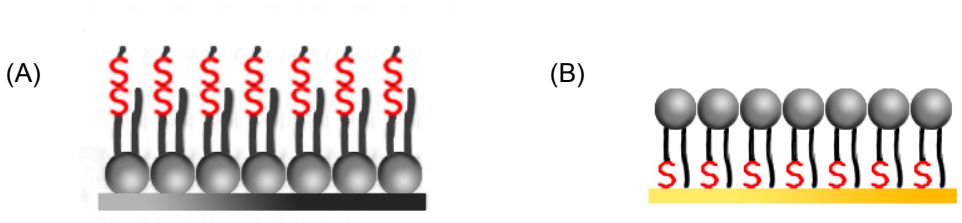

Figure 3.8 Schematic representation of (A) LB films on Si/SiO_x or mica and (B) films deposited on Au by LS, LB or SA.

3.3.4.1 AFM Imaging

AFM images further substantiate that the kink at 26 mN m^{-1} in the π-*A* isotherm of DSDPPC is a collapse and not a phase transition. Before the kink, at π = 25 mN m^{-1} (Figure 3.9A), only two height levels are visible, corresponding to that of condensed domains and remaining fluid phase. The height difference between the condensed phase and fluid phase is 0.7 nm. When the film was collected at π above 32 mN m^{-1} (Figure 3.9B), thicker aggregates, such as the ones observed by BAM at the A/W interface are present. Line sections across the aggregates clearly show steps whose height are multiples of 3 nm, a value corresponding to the thickness of one DSDPPC layer. The phase contrast over the multilayer aggregates is different from that of the monolayer thick condensed phase (Figure

3.9D). DSDPPC seems to buckle and fold to form aggregates.[19-22] Folding is a phase transition from monolayer to multilayers, which is also considered the collapse of the monolayer film. The collapse pressure is sensitive to many trough experimental conditions such as the wetting of the compressing barriers, leakage of the subphase under the barriers or at the trough edges, impurities and temperature.[22,23] These experimental parameters are difficult to control leading to variation in collapse pressures in our DSDPPC and DPPC monolayers. For example, the collapse pressure of the DSDPPC film during our BAM experiments, using a Nima trough, occured at higher surface pressures than during our isotherm measurements done on the standard KSV3000 trough.

The collapse mechanism of pure DPPC films compared to pure DSDPPC film is very different. At collapse, DPPC films do not form multilayer aggragates (Fig. 3.6) and the surface pressure does not keep on rising. These two evidences suggest a collapse through loss of material either through leakage or in form of soluble vesicles.[23,24] DSDPPC films, on the other hand, folds into insoluble multilayers aggregates. This type of collapse is not well understood, and has not been studied much. Pocivavsek *et al.*[22] compared the collapse behaviour of four lipid-lipid and lipid-peptide mixtures and show that the collapse mechanism depends on the in-plane rigidity of the monolayer. This suggests that DSDPPC condensed films are more rigid and have a solid-like response to stress than DPPC condensed films, which is less rigid with a liquid-like response. To gain further insight in the formation and nature of the DSDPPC folding multilayers, compression-expansion monolayer experiments using BAM is proposed. The reversibility or irreversibility of DSDPPC multilayers would be determined.

The AFM images of the monolayer-thick condensed phase (Figure 3.9B) shows a homogeneous height, which further supports the fact that contrast observed in BAM (Figure 3.7) at π = 37 mN m^{-1} is due to molecular tilt anisotropy.[16,18,25,26]

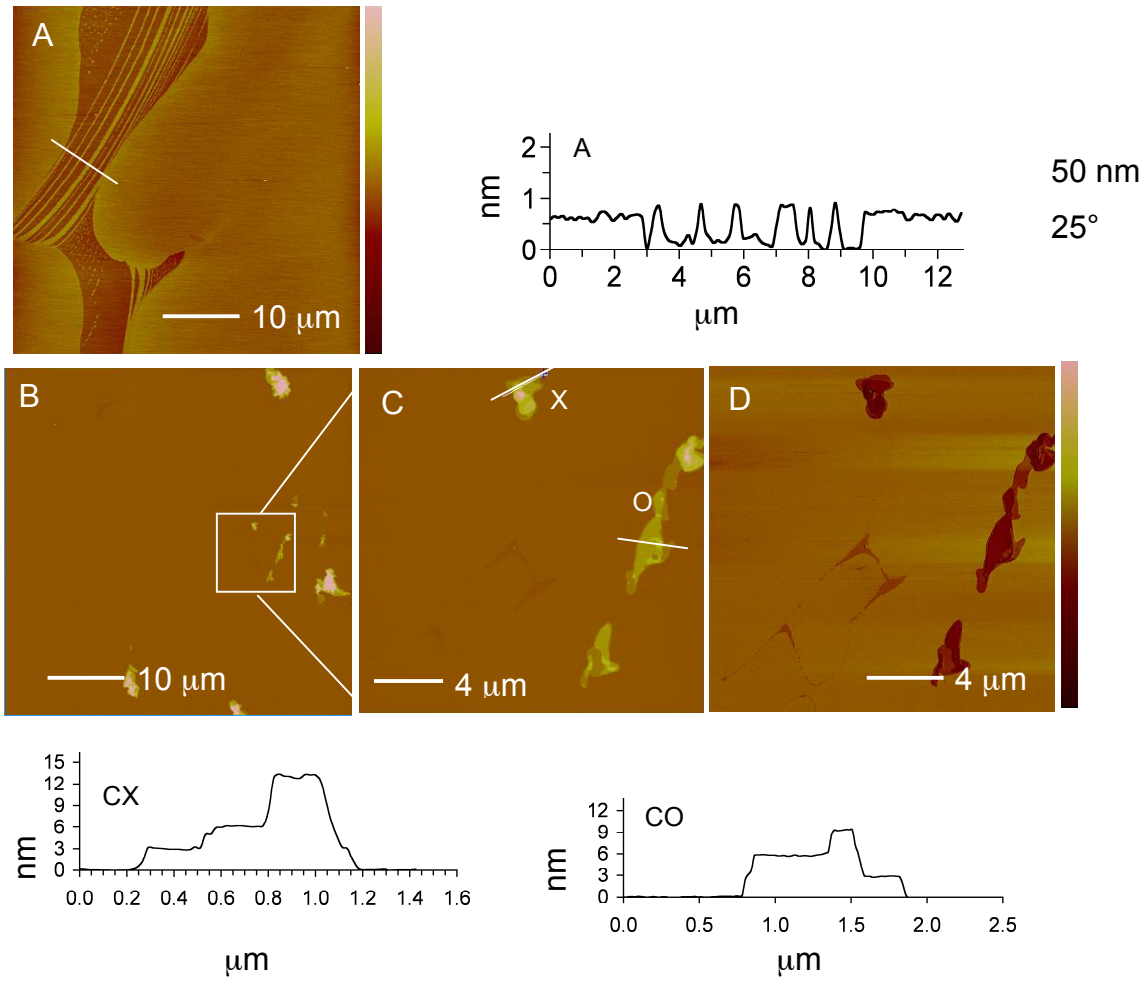

Figure 3.9 AFM images (topography) of DSDPPC films collected at (A) 25 mN m^{-1} and (B) 32 mN m^{-1} by the LB method. Line sections across (A) LE-C phases and (C) condensed and collapsed phases. A zoom of the boxed area in (B) was imaged in (C) topography and (D) phase modes.

3.3.4.2 Ellipsometry Measurements

Film thicknesses measured by ellipsometry also support the fact that the second kink observed in the π-*A* isotherms of DSDPPC is due to film collapse (Table 3.3).

Table 3.3 Film thicknesses ($d_{\text{LB film}}$), of Si/SiO_x-supported phospholipid monolayers from ellipsometry.

thickness	lipid[a] (Å)	π = 16 mN m^{-1} (Å)	π = 32 mN m^{-1} (Å)
DPPC	27.2	19.9 ± 0.1	24.6 ± 0.3 25.1 (T = 23 °C, 40 mN m^{-1})[13]
DSDPPC	32.5	23.3 ± 0.1[b]	33.1 ± 0.4
DSDPPC by SA on Au[b]	28.5	23.6 ± 3.6[c]	—
DLPC	22.2	—	16.9 ± 0.04
DSDLPC	27.5	—	15.0 ± 0.04

[a] calculated from eq. 3.3
[b] π =18 instead of 16 mN m^{-1}
[c] not measured at 18 mN m^{-1}, monolayers self-assembled from solution do not have a measured π.

The extended molecular lengths (l_{lipid}) (i.e., all-trans lipid chains) of the phospholipids were calculated using the formula:[27]

$$l_{\text{lipid}} = l_{\text{chain}} + l_{\text{headgroup}} = (n \text{ x } 1.265 \text{ Å} + 1.5 \text{ Å}) + 8 \text{ Å} \qquad \text{(Eq. 3.3)}$$

where n is the number of CH_2's in the alkyl chain (i.e., n = 10 for DLPC and n = 14 for DPPC). The headgroup diameter was obtained from X-ray reflectiviy and lipid volume data.[28-30] To estimate the extended molecular lengths of assymmetric DSDPPC and DSDLPC, only the longest chain was considered. DSDPPC's functionalized chain contains 15 CH_2s (15 x 1.265 Å = 18.98 Å) followed by a H_2C-S (1.73 Å)[31], a S-S (2.02 Å)[32] and terminated by a S-CH_3 (1.80 Å)[31], which adds up to a chain length of 24.53 Å. The estimated extended length of DSDPPC is 32.53 Å once the length of the headgroup is added. The same method was used to calculate the length of DSDLPC (Table 3.3).

The tilt angle from the A/W interface normal of condensed DPPC monolayers was measured to be 30° by synchrotron X-ray reflectivity at π = 40 mN m^{-1} and T = 23 °C.[28,30] We derived an alkyl chain tilt of 25° for DPPC transferred on Si/SiO_x at π = 32 mN m^{-1} and T = 20 °C from the inverse cosine of the ratio of the ellipsometric thickness (24.6 Å) to the extended molecular length (27.2 Å). An entirely extended DSDPPC monolayer should not exceed 32.5 Å. Due to its assymetry and $–SSCH_3$ group, DSDPPC film thickness is expected to be smaller than 32.5 Å, because of the lack of Van der Waals forces at the functionalized chain end. At π = 18 mN m^{-1}, $d_{\text{LB film}} < l_{\text{lipid}}$ because condensed and LE phases of DSDPPC coexist and DSDPPC molecules are most likely pack in a tilted configuration. The film thickness of 33.1 Å obtained for monolayers transferred at 32 mN m^{-1} is larger than the estimated all-trans extended length of DSDPPC and reflects the presence of multilayer aggregates, since ellipsometry measurements are an average thickness over several cm^2. As seen in the AFM images (Fig. 3.9B), DSDPPC begin to form multilayers at surface pressures above the second kink in the π-*A* isotherm. The film thicknesses of the fluid DLPC and DSDLPC are smaller than their calculated all-trans extended lengths.

3.3.4.3 X-Ray Photoeletron Spectroscopy Characterization

The DSDPPC monolayers were transferred onto Si/SiO_x (Figure 3.8A) and gold (Figure 3.8B) substrates by the LB technique for X-ray photoelectron spectroscopy (XPS) analysis. Compared to the physisorbed films supported on Si/SiO_x, the phospholipids are covalently attached to the gold (Figure 3.8B). We also prepared a hexadecanethiol monolayer on gold (n-C_{16}SAu SAM) by passive incubation as a reference sample. The XPS survey spectra of the DSDPPC films and n-C_{16} SAu SAM are shown in Figure 3.10.

The elements present in DSDPPC that are not found in the n-C_{16}SAu SAM spectrum are phosphorus 2p (135 eV), nitrogen 1s (404 eV) and oxygen 1s (532 eV), confirming the presence of DSDPPC on the surface of the substrate (gold or Si/SiO_x). Peaks for the S2p (circled at 162 eV on Figure 3.9) and S2s (231 eV) are visible in the survey spectra of all three films.

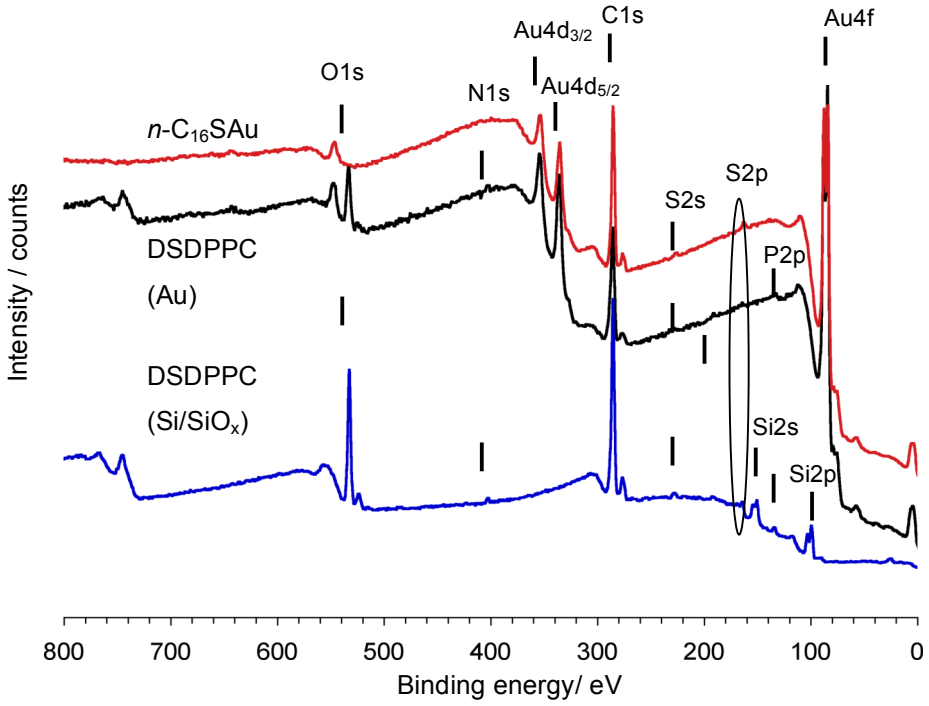

Figure 3.10 XPS survey spectra of DSDPPC on Si/SiO_x, DSDPPC on Au, and *n*-C_{16}SAu SAM

High-resolution S2p spectra were acquired and are presented in Figure 3.11. Each spectrum was fit using one or more doublets ($S2p_{3/2}$ and $S2p_{1/2}$) of area ratio of 2:1, splitting of 1.2 eV, and a FWHM of 1.46. The S2p spectrum of DSDPPC on Si/SiO_x (Figure 3.11A) is more intense that of DSDPPC deposited on gold by LB (Figure 3.11B) because in the first case, the disulfide group is exposed at the SAM surface and in the later case, the sulfur is buried at the SAM/Au substrate interface. The long alkyl chains attenuate the sulfur signal.[33] The sulfur signal of the control *n*-C_{16}SAu is stronger than that of the DSDPPC monolayer, because there is one sulfur per alkyl chain, while in the DSDPPC monolayer, there is only one sulfur for every two chains. It was not possible to quantify the

sulfur using the XPS survey spectra because the S2p peaks are too weak. The S2p spectrum of DSDPPC on Si/SiO_x and DSDPPC on gold both exhibit two peaks, a more intense one between 160 and 165 eV and a much weaker one between 165 and 170 eV. The binding energy (BE) of the $S2p_{3/2}$ components of these two peaks given in Table 3.4.

The BEs of unreacted alkylthiols and disulfides typically range from 163-164 eV[34] and the BE of bulk DSDPPC was measured to be 163.0 ± 0.1 eV (on Si/SiO_x substrate, Figure 3.11A). The minor component present at 167.5-167.7 eV in the S2p spectra of DSDPPC (on Si/SiO_x or Au), which is absent in the spectrum of the *n*-C_{16}SAu SAM, is characteristic of oxidized species,[34] such as sulfoxides, sulfones or sulfonates, suggesting that a fraction of the DSDPPC film was oxidized either due to beam damage during the XPS measurements or oxidation at the A/W interface. This higher BE peak was not observed for all the samples analyzed (see Figure 5.2). The $S2p_{3/2}$ BE DSDPPC monolayer formed on gold is 162.5 eV, the same BE value obtained for our *n*-C_{16}SAu SAM is indicative of a gold-thiolate species.[35-39]

That the $S2p_{3/2}$ spectral line of the LB film of DSDPPC on Au is at the same BE, demonstrates that the $–SSCH_3$ group reacts with the gold surface during the LB deposition to form a gold-thiolate bond.

Table 3.4 BEs of the $S2p_{3/2}$ component of the S2p peak of DSDPPC on Si/SiO_x and on gold, and of a *n*-C_{16}SAu SAM.

	$S2p_{3/2}$ (eV)	$S2p_{3/2}$ – oxidized (eV)
DSDPPC on Si/SiO_x	163.0 ± 0.1 (86 %)[b]	167.5 eV (14 %)[b]
DSDPPC on Au	162.5 (83 %)[b]	167.7 eV (17 %)[b]
n-C_{16}SAu SAM	162.5	

[b] Relative atomic %

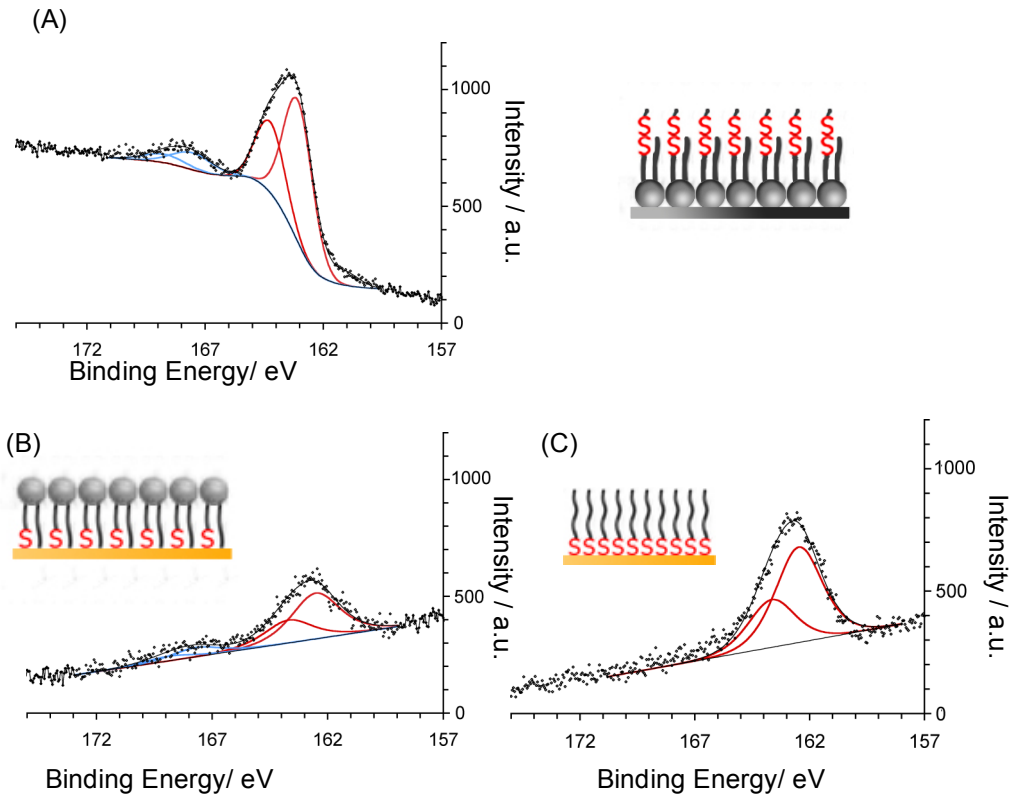

Figure 3.11 High resolution S2p spectra of a DSDPPC monolayer deposited by LB on (A) Si/SiO_x at π = 20 mN m^{-1} and (B) on Au at π = 32 mN m^{-1}. (C) S2p spectrum of a *n*-C16SAu SAM.

3.3.4.4 Cyclic Voltammetry

Reductive desorption can be used as a tool to detect the presence of a gold- thiolate surface species and to quantify its surface coverage.[40] The potential of the desorption peak (E_p) depends on the hydrocarbon chain length, the terminal functional group of the alkylthiolate, and the crystallinity of the gold substrate. Thiols and thiolates have low solubility in aqueous solution. It has been proposed that once desorbed, they remain physisorbed or close to the gold surface to then be redeposited during the oxidative cycle. The cyclic voltamograms of DSDPPC and *n*-C_{16}SH deposited on gold by SA from solution are presented in Figure 3.12. Reductive desorption further substantiates that the DSDPPC molecules form a gold-thiolate bond. A *n*-C_{16}SAu SAM was prepared as a reference sample. The cyclic voltammogram of the *n*-C_{16}SAu SAM is shown in Figure 3.12A. Only one reductive stripping peak is detected at E = -1.14 V indicative of one bound thiolate species. Readsorption peaks are also present in the anodic segment of the cyclic voltammogram because the *n*-C_{16}S is insoluble in aqueous alkaline solution and remains near the surface after desorption. The cyclic voltammogram of a DSDPPC SAM on gold is shown in Figure 3.12B. The self-assembled film was chosen for reductive desorption because XPS did not detect the presence of sulfur for this type of film. The presence of a desorption peak at E = -1.08 V, confirms the presence of a thiolate-gold bond. No readsorption peak is detected, probably due to loss or diffusion of material from the Au surface.

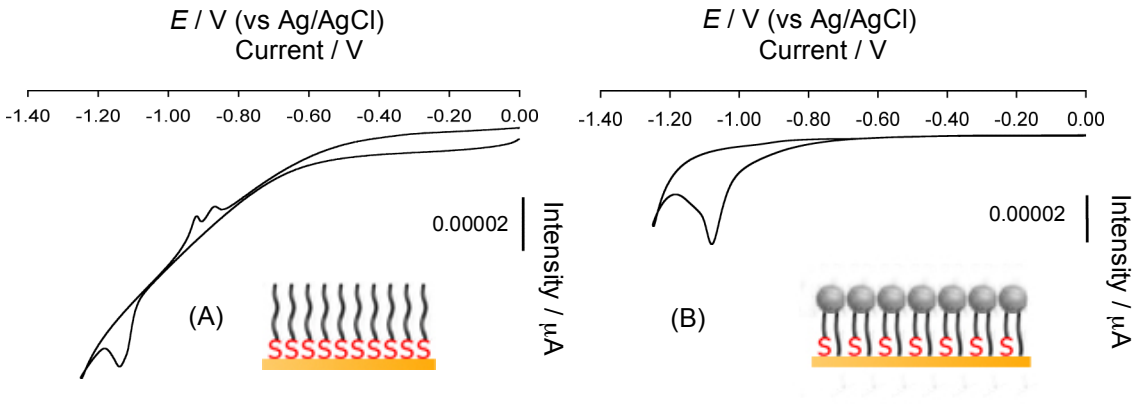

Figure 3.12 Cyclic voltammograms in 0.1 M KOH of (A) *n*-C_{16}SAu SAM and (B) DSDPPC –Au film formed by self-assembly from solution.

3.3.4.5 ATR-IR Spectroscopy

ATR-IR was used to compare the extent of chain ordering in DSDPPC monolayers deposited onto gold substrates using three different methods: (i) self-assembly (SA) in a 1 mM ethanolic solution for 1 h, (ii) self- assembly (SA) in a 1 mM ethanolic solution for 20 h or (iii) LB film deposition (Table 3.5 and Figure 3.13). The results obtained indicate that the DSDPPC SAMs on gold exhibit similar alkyl chain ordering whether the incubation lasted 1 or 20 h, while the film deposited by LB at 32 mN m^{-1} was the most disordered. SAMs with ordered alkyl chains are characterized by CH_2 antisymmetric (υ_{as}) and symmetric (υ_s) stretching frequencies of 2916-2918 and 2848-2850 cm^{-1}.[41-43] The CH_2 (υ_{as}) and (υ_s) values of 2921-2923 cm^{-1} and 2851-2852 cm^{-1}, however, indicate that the alkyl chains are disordered in the DSDPPC monolayers. The ATR-IR spectral region of 500-1800 cm^{-1} of DSDPPC in the powder and solid-supported monolayer forms are shown in Figure 3.13B. The spectra of DSDPPC films deposited on gold under different conditions are very similar. The carbonyl stretching band (υCO) appears at 1734 cm^{-1} and the band at 1467 cm^{-1} represents the CH_2 scissoring mode (δCH_2). The assymmetric stretching

frequency of phosphate (υ_{as} PO_2^-) is found at 1244 cm^{-1}, which suggests some degree of hydration of the phosphate headgroup. The PO stretching frequency of an unhydrated phosphate headgroup is around 1262 cm^{-1} and decreases with the addition of water to a value of 1238 cm^{-1}.[44,45] The presence of the carbonyl and phosphate stretching bands confirms the presence of phospholipids on the surface of the gold substrate.

Table 3.5 $\upsilon_{as}(CH_2)$ and $\upsilon_s(CH_2)$ values of DSDPPC films deposited on Au using different methods

	$\upsilon_{as}(CH_2)$ (cm^{-1})	$\upsilon_s(CH_2)$ (cm^{-1})
DSDPPC powder	2917	2850
SA (1 h)	2921	2851
SA (20 h)	2922	2851
LB film π = 32 mN m^{-1}	2923	2852

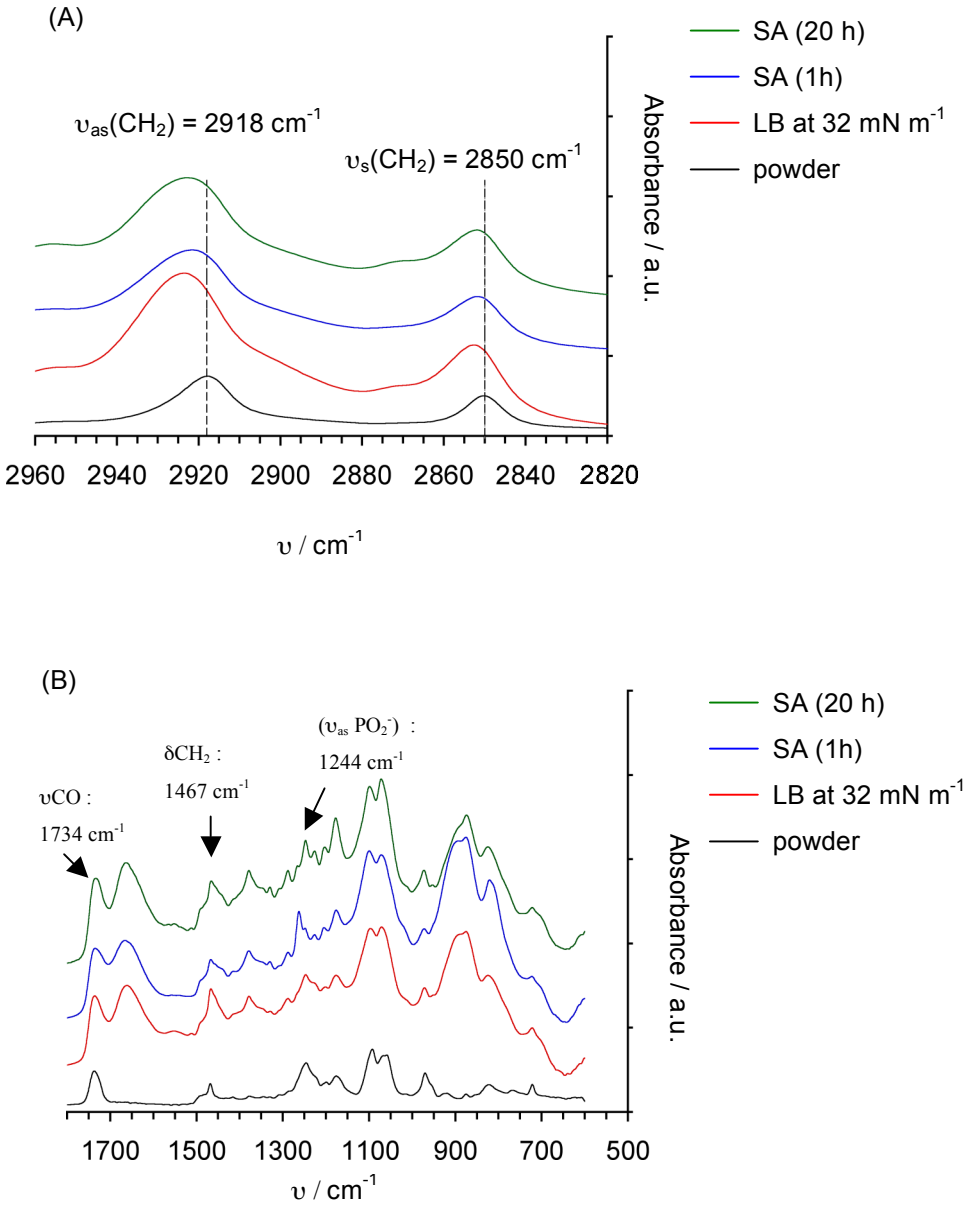

Figure 3.13 ATR-IR spectra of DSDPPC powder and monolayers deposited onto gold: (A) CH_2 stretching region and (B) 500 cm^{-1} to 1750 cm^{-1} region

3.4 Conclusions

The phase transition temperature of DPPC and DSDPPC were compared using DSC and UV-Vis spectroscopy. The pre-transition observed in DPPC MLVs was not observed in DSDPPC MLVs. The higher T_m of DSDPPC compared to that of DPPC (43.4 vs. 41.1 °C) can be explained through the addition of of a disulfide group in the DSDPPC molecule that would promote stabilizing interactions between the alkyl chains resulting in a higher T_m. To better understand these interactions, the ΔH were measured using a microDSC. A ΔH of 31 kJ mol^{-1} was obtained for DPPC, which corresponds to values reported in the literature. The ΔH of DSDPPC was measured to be 41.9 kJ mol^{-1} indicative of a larger difference in enthalpy between the liquid crystalline phase and the lamellar gel phase of DSDPPC compared to DPPC possibly due to a more disordered liquid crystalline phase of DSDPPC.

Langmuir films of modified phospholipids were compared to the natural lipids by their π-A isotherm and by BAM. The LE-C phase transition of DSDPPC and DPPC were 6 and 4 mN m^{-1} respectively. DSDLPC, like DLPC, remained in a fluid state throughout the compression of the film at 20.0 °C. Morphologies of DSDPPC monomolecular film were investigated by BAM. Unlike DPPC that forms a homogeneous film at π > 10 mN m^{-1}, DSDPPC forms phase separated condensed domains at 6 mN m^{-1} < π < 32 mN m^{-1}. At π larger than 32 mN m^{-1}, buckling of the monolayer is visible through the appearance of aggregates. These aggregates were imaged by AFM and showed defined steps in multiples of 3 nm, corresponding to the thickness of one monolayer of DSDPPC.

DSDPPC films were transferred onto mica or Si/SiO_x forming a physisorbed thin layer with disulfide groups exposed. AFM, XPS, ellipsometry and ATR-IR characterizations demonstrate the formation of DSDPPC monolayers with unreacted disulfide groups.

DSDPPC films were also formed on gold, this time leaving the phosphocholine head group exposed. XPS and reductive desorption of these films confirmed a covalent attachment between the gold substrate and the modified lipid through gold-thiolate species.

The self-assembly capacity of these novel lipids allows one to use them as platforms to study nanoscale phenomena, to create regular nanopatterns, and as possible biosensors.[46,47]

3.5 References

(1) Nuzzo, R. G.; Zegarski, B. R.; Dubois, L. H. *J. Am. Chem. Soc.* **1987**, *109*, 733.

(2) Mason, J. T.; Broccoli, A. V.; Huang, C.-H. *Anal. Biochem* **1981**, *113*, 96.

(3) Selinger, Z.; Lapidot, Y. *J. Lipid Res.* **1966**, *7*, 174.

(4) Runquist, E. A.; Helmkamp Jr, G. M. *Biochim. Biophys. Acta* **1988**, *940*, 10.

(5) Ihalainen, P.; Peltonen, J. *Langmuir* **2002**, *18*, 4953.

(6) Adejare, A.; Shen, J.; Ogunbadeniyi, A. M. *J. Fluorine Chem.* **2000**, *105*, 107.

(7) Bartlett, G. R. *J. Biol. Chem.* **1959**, *234*, 466.

(8) Sanchez, J.; Badia, A. *Thin Solid Films* **2003**, *440*, 223.

(9) Cherry, R. J.; Chapman, D. *J. Mol. Biol.* **1969**, *40*, 19.

(10) Marra, J.; Israelachvili, J. *Biochemistry* **1985**, *24*, 4608.

(11) Schmidt, R.; DeWolf, C. E. *Langmuir* **2004**, *20*, 3284.

(12) Yi, P. N.; MacDonald, R. C. *Chem. Phys. Lipids* **1973**, *11*, 114.

(13) Marsh, D. *CRC Handbook of Lipid Bilayers*; CRC Press, Inc.: Boca Raton, FL, 1990.

(14) Kaganer, V. M.; Mohwald, H.; Dutta, P. *Rev. Mod. Phys.* **1999**, *71*, 779.

(15) Gopal, A.; Lee, K. Y. C. *J. Phys. Chem. B* **2006**, *110*, 22079.

(16) Nandi, N.; Vollhardt, D. *Chem. Rev.* **2003**, *103*, 4033.

(17) Schief, W. R.; Touryan, L.; Hall, S. B.; Vogel, V. *J. Phys. Chem. B* **2000**, *104*, 7388.

(18) Sanchez, J.; Badia, A. *Chem. Phys. Lipids* **2008**, *152*, 24.

(19) Birdi, K. S.; Vu, D. T. *Langmuir* **1994**, *10*, 623.

(20) Nikomarov, E. S. *Langmuir* **1990**, *6*, 410.

(21) Rugonyi, S.; Smith, E. C.; Hall, S. B. *Langmuir* **2004**, *20*, 10100.

(22) Ybert, C.; Lu, W.; Moller, G.; Knobler, C. M. *J. Phys. Chem. B* **2002**, *106*, 2004.

(23) Pocivavsek, L.; Frey, S. L.; Krishan, K.; Gavrilov, K.; Ruchala, P.; Waring, A. J.; Walther, F. J.; Dennin, M.; Witten, T. A.; Lee, K. Y. C. *Soft Matter* **2008**, *4*, 2019.

(24) Baoukina, S.; Monticelli, L.; Risselada, H. J.; Marrink, S. J.; Tieleman, D. P. *Proc. Natl. Acad. Sci USA* **2008**, *105*, 10803.

(25) Weidemann, G.; Vollhardt, D. *Colloid Surf. A* **1995**, *100*, 187.

(26) Weidemann, G.; Vollhardt, D. *Thin Solid Films* **1995**, *264*, 94.

(27) Smith, G. S.; Majewski, J. Lipid Bilayers: Structure and Interactions. In *X-Ray and Neutron Scattering Studies of Lipid Monolayers and Single Bilayers*; Katsaras, J., Gutberlet, T., Eds.; Springer-Verlag: Heidelberg, 2001; pp 127.

(28) Helm, C. A.; Möhwald, H.; Kjaer, K.; Als-Nielsen, J. *Europhys. Lett.* **1987**, *4*, 317.

(29) Nagle, J. F.; Tristram-Nagle, S. *Biochim. Biophys. Acta* **2000**, *1469*, 159.

(30) Cevc, G.; Marsh, D. *Phospholipid Bilayers*; John Wiley & Sons: Toronto, 1987.

(31) Curtiss, L. A.; Nobes, R. H.; Pople, J. A.; Radom, L. *The Journal of Chemical Physics* **1992**, *97*, 6766.

(32) Van Wart, H. E.; Shipman, L. L.; Scheraga, H. A. *J. Phys. Chem.* **1974**, *78*, 1848.

(33) Bain, C. D.; Whitesides, G. M. *J. Phys. Chem.* **1989**, *93*, 1670.

(34) NIST X-ray Photoelectron Spectroscopy Database, Reference Database 20, Version 3.5, 2003.

(35) Laibinis, P. E.; Whitesides, G. M.; Allara, D. L.; Tao, Y. T.; Parikh, A. N.; Nuzzo, R. G. *J. Am. Chem. Soc.* **1991**, *113*, 7152.

(36) Bain, C. D.; Troughton, E. B.; Tao, Y. T.; Evall, J.; Whitesides, G. M.; Nuzzo, R. G. *J. Am. Chem. Soc.* **1989**, *111*, 321.

(37) Bain, C. D.; Biebuyck, H. A.; Whitesides, G. M. *Langmuir* **1989**, *5*, 723.

(38) Bourg, M.-C.; Badia, A.; Lennox, R. B. *J. Phys. Chem. B* **2000**, *104*, 6562.

(39) Castner, D. G.; Hinds, K.; Grainger, D. W. *Langmuir* **1996**, *12*, 5083.

(40) Badia, A.; Arnold, S.; Scheumann, V.; Zizlsperger, M.; Mack, J.; Jung, G.; Knoll, W. *Sensor Actuat. B-Chem.* **1999**, *54*, 145.

(41) MacPhail, R. A.; Strauss, H. L.; Snyder, R. G.; Elliger, C. A. *J. Phys. Chem.* **1984**, *88*, 334.

(42) Nuzzo, R. G.; Dubois, L. H.; Allara, D. L. *J. Am. Chem. Soc.* **1990**, *112*, 558.

(43) Snyder, R. G.; Strauss, H. L.; Elliger, C. A. *J. Phys. Chem.* **1982**, *86*, 5145.

(44) Wang, X.; Zheng, S.; He, Q.; Brezesinski, G.; Möhwald, H.; Li, J. *Langmuir* **2004**, *21*, 1051.

(45) Tsai, Y. S.; Ma, S. M.; Kamaya, H.; Ueda, I. *Mol. Pharmacol.*, *31*, 623.

(46) Cornell, B. A.; Braach-Maksvytis, V. L.; King, L. G.; Osman, P. D.; Raguse, B.; Wieczorek, L.; Pace, R. J. *Nature* **1997**, *387*, 555.

(47) Sackmann, E. *Science* **1996**, *271*, 43.

Chapter 4 Morphology of Mixed Monolayers of DSDPPC & DSDLPC

4.1 Introduction

After comparing the phase behaviour of single component systems of the natural and functionalized phospholipids, we compare the properties of binary mixtures in this chapter. DPPC (16 carbons) and DLPC (12 carbons) are both saturated dialkylphosphocholines possessing their main gel-to-liquid crystalline phase transition temperatures at 41 and -1 °C, respectively.[1] Since one of the components in this binary mixture is in the gel (solid) phase at the temperature studied andthe chain length difference between the two lipids is at least four carbons, phase separation in this mixture will occur.[2-5]

Multilamellar aqueous dispersions and giant unilamellar vesicles formed from DPPC/DLPC mixtures exhibit a region of solid/fluid phase co-existence between DPPC mole fractions of 0.25 to 0.35 and 0.80 to 0.85 at T = 20-25 °C.[1,6-8] Badia *et al.*[9,10] have shown in previous work that binary mixtures of DPPC/DLPC will phase separate at the A/W interface and lead to the formation of parallel lines when deposited onto mica under specific conditions using the LB film deposition technique.[9-11] This stripe pattern is generated by the film transfer process, as previously discussed in Chapter 2. By contrast, an array of randomly ordered circular domains of condensed phase DPPC is observed using LS deposition.[11] In this chapter, we examine mixed monolayers at the A/W interface and compare the phase structure of LB and LS films formed from mixtures of DPPC/DLPC with those formed from DSDPPC/DLPC and DPPC/DSDLPC mixtures using BAM imaging, field-emission gun scanning electron microscopy (FEGSEM), time-of-flight secondary ion mass spectrometry (TOF-SIMS), and AFM.

4.2 Experimental Section

4.2.1 Langmuir Monolayer Films

A standard KSV 3000 trough (surface area of 768 cm^2) equipped with a Pt Wilhelmy plate sensing device (KSV Instruments, Helsinki, Finland) and an Isotemp 1006D circulation bath (Fisher Scientific) was used. The subphase temperature was maintained at 20.0 ± 0.5 ºC.

Solutions consisting of binary mixtures of DPPC, DLPC, DSDPPC, and DSDLPC at 1 mM total lipid concentration were prepared using spectrograde chloroform. Monolayers were formed by spreading 90 - 100 μL of the appropriate solution on the water surface of the standard LB trough. The solvent was allowed to evaporate for 15 min. The phospholipid molecules were symmetrically compressed to the target pressure at a rate of 1 $Å^2$ $molecule^{-1}$ min^{-1}. The film was then transferred onto a substrate by Langmuir-Schaefer or Langmuir-Blodgett deposition after 20 min of stabilization at the target pressure. By LB deposition, the mica or Si/SiO*x* was pulled vertically upward from the water subphase through the A/W interface at a rate of 5 mm min^{-1} or 1 mm min^{-1}. By LS, the substrate was placed under the film, in the subphase, and the subphase was lowered by suction until the film deposited onto the substrate.

4.2.2 Surface Characterization Techniques

AFM and BAM imaging were performed as described in Section 2.2.3 and 3.2.6.

4.2.2.1 Field Emission Gun Scanning Electron Microscopy (FEGSEM)

Samples were imaged using a Hitachi S-4700 instrument. Secondary electron images were acquired at 2 kV, 10 μA, and 4.6 – 5.0 mm working distance.

4.2.2.2 Time of Flight Secondary Ion Mass Spectroscopy (TOF-SIMS)

TOF-SIMS studies were carried out using an ION-TOF SIMS IV (Münster, Germany). The instrument has an operating pressure of 7×10^{-9} Torr. Samples were bombarded with a pulsed ion source of liquid gallium ($^{69}Ga^{+}$), with an energy of 25 keV. The gun was operated with a 27 ns pulse width, 1.47 pA pulsed ion current for a dosage of 5×10^{13} ions cm^{-2}, just on the threshold level for static SIMS. Secondary ions were detected with a Reflectron time-of-flight analyzer, a multichannel plate, and a time-to-digital converter. Measurements were performed with a typical acquisition time of 100 s, at a thermal conductivity dectector (TCD) time resolution of 200 ps. An electon flood gun was used to neutralize the charges. Secondary ion spectra were acquired from an area of 40 × 40 μm. The mass resolution, $R = m/\Delta m$, was 8,000 on $^{29}Si^{+}$, where m is the target ion mass and Δm is the resolved mass difference at the peak half-width. All ion images were acquired over 200 x 200 or 500 x 500 μm, with 128 x 128 pixels (1 pulse per pixel), on at least at three different regions of the sample.

4.3 Results and Discussion

4.3.1 π-*A* Isotherms of Equimolar Mixtures

The π-*A* isotherms of equimolar mixtures of DPPC/DLPC,[10] DSDPPC/DLPC and DPPC/DSDLPC are presented in Figure 4.1. The DSDPPC/DLPC and DPPC/DSDLPC monolayers are more expanded than DPPC/DLPC. As in the case of DPPC/DLPC, the isotherm of the DSDPPC/DLPC mixture exhibits a distinct kink, near 13 mN m^{-1}, indicative of a LE-C transition. No such feature is evident for DPPC/DSDLPC, although lateral phase separation still occurs in this mixture, as shown in Figure 4.4. The onset area of each of the mixed monolayers lies between the onset areas of the pure phospholipids that compose the binary mixture (Table 4.1). The collapse pressures (π_c) of the mixtures occur at pressures similar to that of the lipid with the lowest π_c. For example, the π_c of

DSDPPC/DLPC is similar to that of DSDPPC at ~ 30 mN m^{-1} and the π_c of DPPC/DSDLPC is similar to that of DSDPLC at ~ 40 mN m^{-1} (Table 4.1). The collapse behaviour of the mixed monolayers is consistent with the lateral phase separation of the lipids to form phases that are enriched in one of the lipid components.

Table 4.1 Summary of onset areas (A_{onset}), surface pressure of the LE-C transition (π_{LE-C}), and collapse pressures (π_c) of pure and mixed lipid films

	A_{onset} (Å^2 molecule^{-1})	π_{LE-C} (mN m^{-1})	π_c (mN m^{-1})
DPPC (n=3)	92 ± 1	4 ± 1	57 ± 2
DSDPPC (n=5)	121 ± 2	5 ± 1	25 ± 2
DLPC (n=2)	108 ± 1	-	48 ± 1
DSDLPC (n=3)	135 ± 1	-	40 ± 1
DPPC/DLPC 1:1 (n=4)	100 ± 1	15 ± 1	50 ± 3
DSDPPC/DLPC 1:1 (n=1)	116	13	30
DPPC/DSDLPC 1:1 (n=1)	109	-	42

n = # of isotherms used to calculate the average

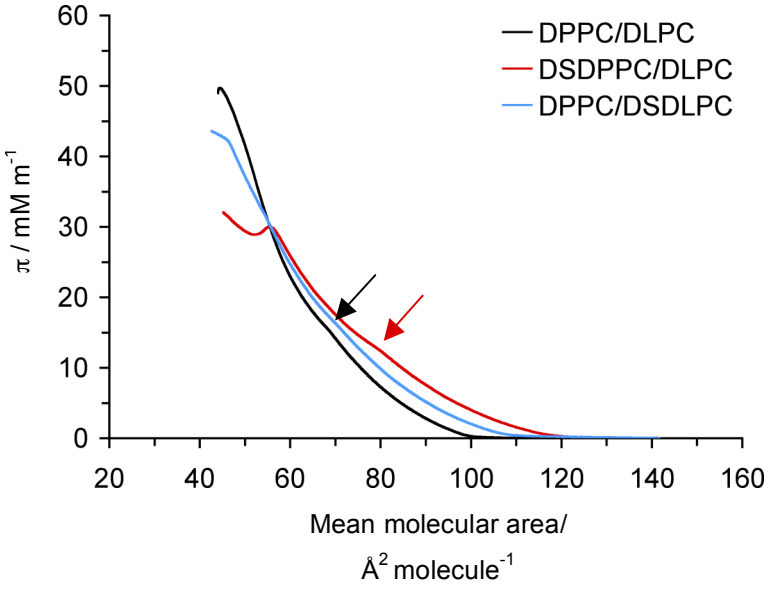

Figure 4.1 π-*A* isotherms of 1:1 (mol/mol) binary mixtures recorded on a pure water subphase at 20.0 °C on the KSV 2000 standard trough. The arrows indicate the LE-C phase transition.

The additivity rule is often applied to the molecular areas at a given pressure to determine the extent of miscibility of two molecules at the A/W interface. Monolayers of ideal heterogeneous mixtures (i.e. complete lateral phase separation) should present similar properties to the monolayers of the pure molecules. Hence, the mean molecular area of the mixture at a defined surface pressure should be equal to the sum of the molecular area that each pure molecule occupies at that surface pressure, according to the following equation:[12,13]

$$A_{1,2} = N_1A_1 + N_2A_2 \qquad \text{(Eq. 4.1)}$$

The additivity rule applies to ideally mixed systems and completely phase-separated systems. At low surface pressure (π = 3 mN m^{-1}), the calculated and experimental mean molecular areas (mma) for DPPC/DLPC 1:1, DPPC/DSDLPC 1:1, and DSDPPC/DSDLPC 1:1 are in good agreement. At 10 mN m^{-1} < π < 25 mN m^{-1}, the experimental molecular

areas of all three mixtures are larger by 5-10% than the calculated ones. This translates as additional intermolecular repulsive forces present in the mixtures.[12,13] These additional repulsive forces are negligible when the mixed monolayers are compressed above 25 mN m^{-1}. Therefore, at low surface pressure the molecules are perfectly mixed. At $10 < \pi < 25$ mN m^{-1}, lateral phase separation occurs, which results in a non-ideal mixing behaviour and a positive deviation from ideality. Then at $\pi \geq 25$ mN m^{-1}, lateral phase separation is complete and the mixtures behave ideally.

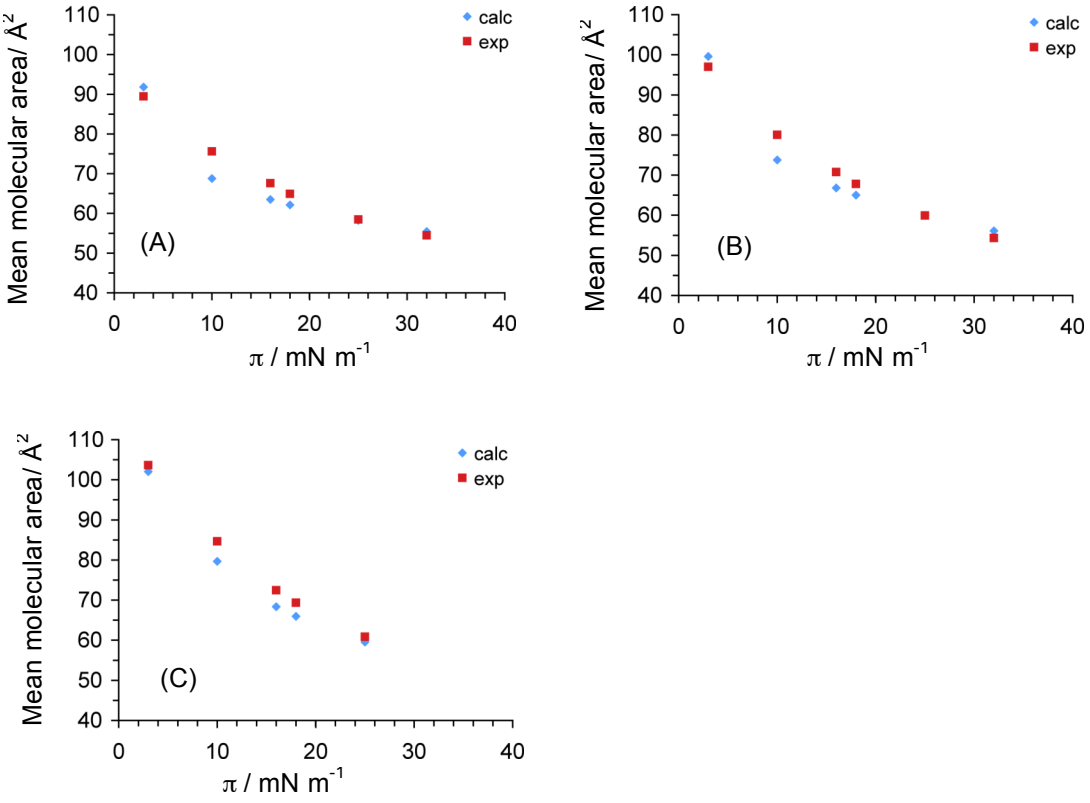

Figure 4.2 Calculated (calc) and experimental (exp) values of mean molecular area as a function of surface pressure for 1:1 (mol/mol) mixtures of (A) DPPC/DLPC, (B) DPPC/DSDLPC, and (C) DSDPPC/DSDLPC.

4.3.2 BAM Imaging of Equimolar Binary Mixtures

Mixed monolayers of equimolar composition were investigated by Brewster Angle Microscopy (BAM) imaging during lateral compression at the A/W interface. The binary mixtures of DPPC/DLPC (Figure 4.3) and DPPC/DSDLPC (Figure 4.4) exhibit similar condensed domain morphologies. Circular-shaped domains appear at ~ 11.8 mN m^{-1} for the unmodified lipid mixtures and at ~ 14.0 mN m^{-1} for the DPPC/DSDLPC mixture. At higher surface pressure, 30 mN m^{-1}, the quasi-circular domains transform into distinct flowers composed of 4 or 5 petals and do not grow further in size. At $\pi \geq 40$ mN m^{-1}, the diameter of condensed domains decreases suggesting that the DPPC molecules remix with the shorter chain lipids. Sanchez and Badia observed the same behaviour for LB films of DPPC/DLPC 1:1 (mol/mol) mixtures.[10] Our results are consistent with theirs, BAM images of DPPC/DLPC 1:1 at 32 mN m^{-1} exhibit large flower-like domains and at 40 mN m^{-1}, these domains are decreased in size. The AFM images acquired by Sanchez and Badia[10] of DPPC/DLPC 1:1 (mol/mol) show that the condensed domains shrink in diameter through the development of fine dendritic branches not resolvable by BAM (1 μm lateral resolution). The authors suggest that the remixing is due to a similar density of the condensed and LE phase at $\pi \geq 40$ mN m^{-1} which reduces the interfacial line tension, allowing for the more prolonged boundaries of the dendritic shapes or the disappearance of the flower-like domains.

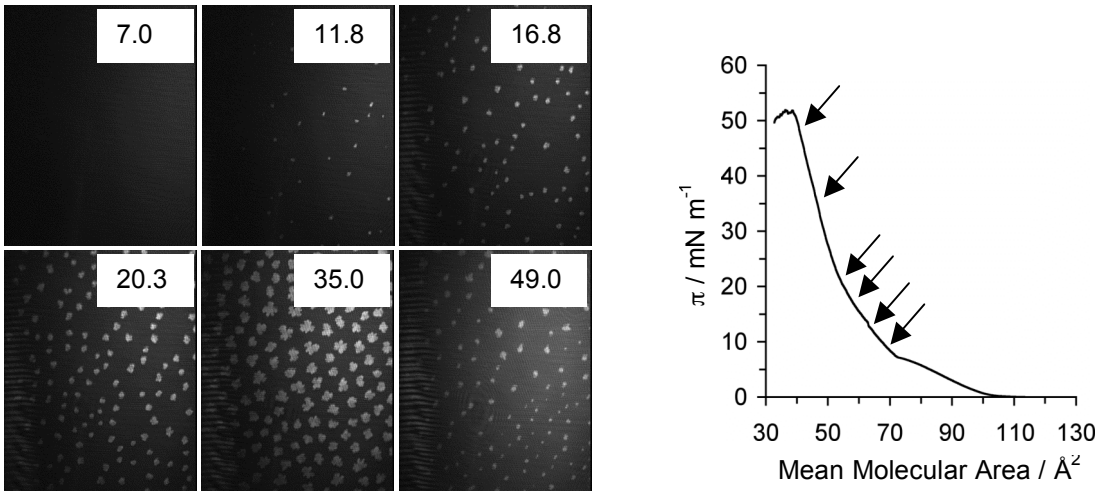

Figure 4.3 BAM images (538 μm x 430 μm) and corresponding π-*A* isotherm of DPPC/DLPC 1:1 mixture acquired at 20.0 °C on a pure water subphase. The arrows in the π-*A* isotherm correspond to the surface pressure of the images shown on the left.

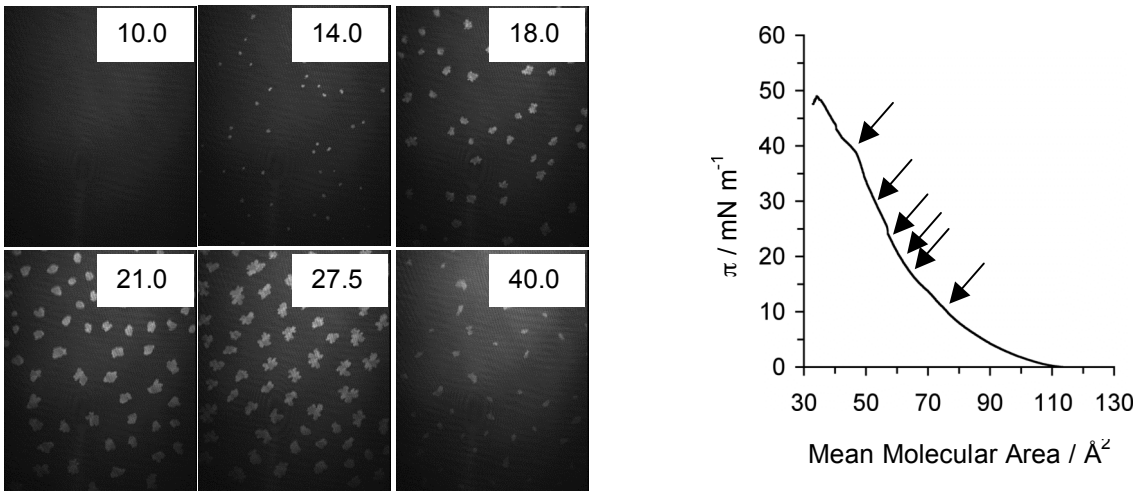

Figure 4.4 BAM images (538 μm x 430 μm) and corresponding π-*A* isotherm of DPPC/DSDLPC 1:1 mixture acquired at 20.0 °C on a pure water subphase. The arrows in the π-*A* isotherm correspond to the surface pressure of the images shown on the left.

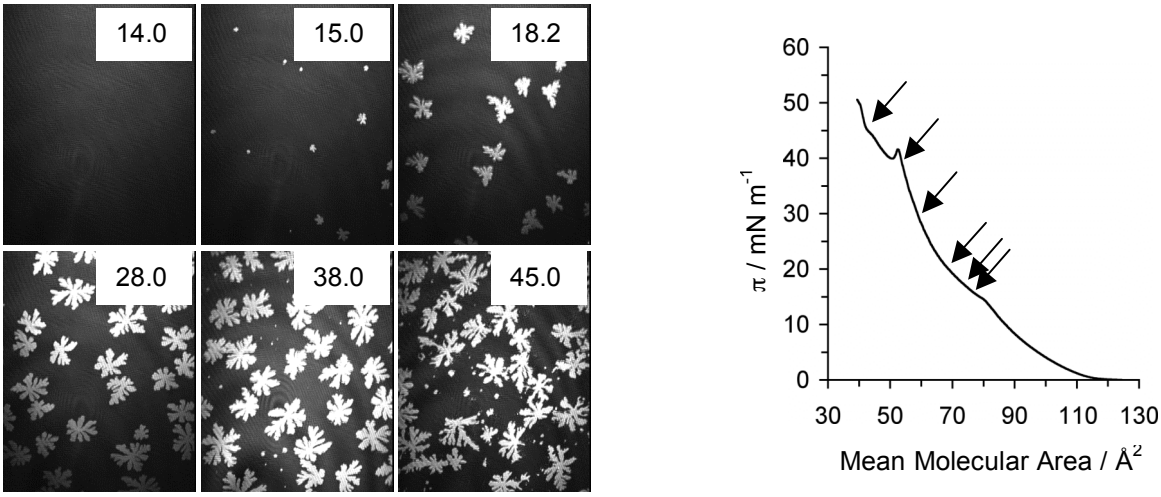

Figure 4.5 BAM images (538 μm x 430 μm) and corresponding π-*A* isotherm of DPPC/DSDLPC 1:1 mixture acquired at 20.0 °C on a pure water subphase. The arrows in the π-*A* isotherm correspond to the surface pressure of the images shown on the left.

Table 4.2 Summary of the domain areas in the binary mixtures imaged by BAM

	# of domains [a]	Domain size [b] (μm)	Size of largest domains (μm)
DPPC/DLPC	60	12 ± 2	24 ± 3
DPPC/DSDLPC	40	21 ± 4	35 ± 8
DSDPPC/DLPC	20	43 ± 7	71 ± 11

[a] At $\pi \approx 16$ - 18 mN m^{-1} (in 538 x 430 mm area)
[b] At $\pi \approx 16$ - 18 mN m^{-1}

BAM images of DSDPPC/DLPC are presented in Figure 4.5. Condensed domains appear around 14 mN m^{-1}. At the LB film transfer pressure of 18 mN m^{-1} typically used for this mixture to obtain the stipe pattern, dendritic-like or snowflake domains are much larger than for the two previous mixtures. As the surface pressure increases, the snowflakes grow

bigger. At high surface pressure ($\pi \geq 38$ mN m^{-1}), the condensed DSDPPC domains still occupy about 50% of the area and do not remix with the fluid lipid as per DPPC. Similar to pure DSDPPC monolayers (sections 3.3.2 to 3.3.4), the collapse pressures of DSDPPC/DLPC mixtures are sensitive to many experimental trough conditions. Monolayers compressed on the Nima trough collapse near 40 mN m^{-1} (Figure 4.5) compared to a collapse pressure near 30 mN m^{-1} on the KSV 2000 trough (Figure 4.1).

As a general trend observed, the condensed domain morphology of the binary mixtures investigated is dominated by the behaviour of the condensed lipid (Figures 3.5 and 3.6).

4.3.3 Langmuir-Schaefer Films of DSDPPC/DLPC

Other surface characterization techniques were also applied to the 1:1 binary mixture of DSDPPC/DLPC, specifically, FEGSEM, AFM and TOF-SIMS. Each technique is complementary to the others, providing different information about the mixed monolayer film. DSDPPC/DLPC 1:1 monolayer films were deposited by the LS method (i.e., horizontal deposition) to minimize the deformation of the condensed domain shape. Si/SiO_x was used as the supporting substrate (instead of mica) for all three characterization techniques because TOF-SIMS requires a conducting surface.

FEGSEM gives a large field of view with high lateral resolution (~ 5 nm), while the maximum scan size of 100 x 100 μm in AFM limits the field of view but provides the best lateral resolution (0.1 nm), as well as topographical information, or thickness differences between co-existing phases with a height resolution of 0.01 nm. Dendritic-like flowers are observed for the DSDPPC phase in both FEGSEM and AFM (Figures 4.6 and 4.7). The phase contrast observed in FEGSEM for DSDPPC/DLPC is also observed for DPPC/DLPC (image not shown) and is due to differences in the molecular packing densities of the condensed versus fluid phases rather than chemical differences.[14] AFM also shows the

presence of condensed microdomains in the surrounding matrix. The height difference between the DSDPPC condensed phase and the DLPC fluid phase background is 0.9 nm, as shown by the line section in Figure 4.7.

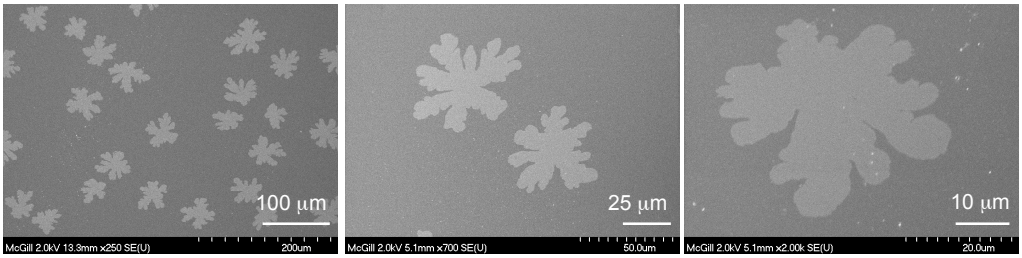

Figure 4.6 FEGSEM micrographs of LS films of DSDPPC/DLPC 1:1 on Si/SiO_x (π = 18 mN m^{-1}).

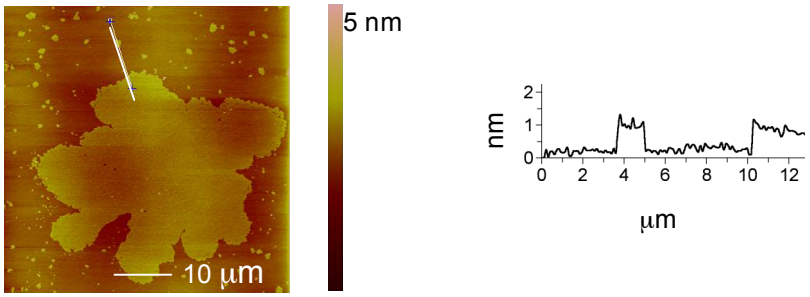

Figure 4.7 AFM of LS films of DSDPPC/DLPC (1:1) on Si/SiO_x and corresponding cross-section (π = 18 mN m^{-1}).

.

Time of flight-secondary ion mass spectrometry (TOF-SIMS) offers spatially resolved, chemical information not provided by SEM or AFM. TOF-SIMS is a chemical mapping surface technique with a penetration depth of 1-3 monolayers. The surface is bombarded with a gallion ion beam, which results in the ejection of secondary ions by sputtering from the surface. The elemental composition and chemical structure of the outer

layer are measured by the mass/charge ratio of the secondary ions and their time of flight between the sample and the detector. TOF-SIMS images of the SH, S and -SS- distributions across DPPC/DLPC and DSDPPC/DLPC (1:1) monolayers are shown in Figure 4.8. We clearly see that the -SS- groups are clustered in the quasi-circular condensed phase domains and no sulfur signal is detected in the DPPC/DLPC control. The TOF-SIMS maps confirm the validity of our assignment of the thicker flower-like domains of mixed monolayers to DSDPPC.

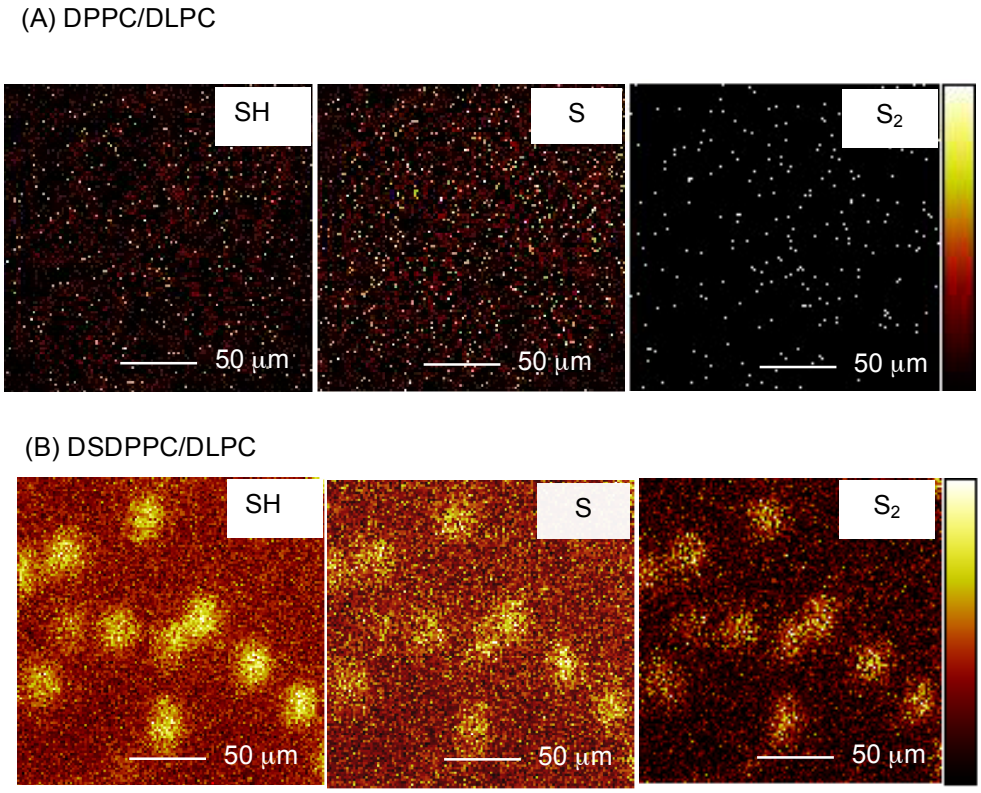

Figure 4.8 TOF-SIMS images (200 x 200 μm) of (A) DPPC/DLPC 1:1, π = 16 mN m^{-1}, and (B) DSDPPC/DLPC 1:1, π = 18 mN m^{-1} on Si/SiO_x by LS.

4.3.4 Langmuir-Blodgett Films of Equimolar Mixtures

Self-patterned arrays of linear features were previously prepared using the LB transfer of phase-separated binary mixtures of DPPC and DLPC.[9] The stripe patterns were explained in terms of a process involving initial self-association of like lipids (hydrophobic match) at the A/W interface during monolayer compression to give condensed microdomains of one lipid that are dispersed in a fluid matrix of the second lipid, followed by the self-organization and coalescence of the lipid domains at the three-phase contact line during LB deposition. The mechanism of stripe formation is described in Chapter 2.

In this section, chemically heterogeneous patterns formed by the ω-methyldisulfide-terminated analogues, DSDPPC and DSDLPC, are compared with those of the unmodified phospholipids. Langmuir monolayers formed from 3:1 or 1:1 (mol/mol) binary mixtures of DPPC/DLPC, DPPC/DSDLPC, and DSDPPC/DLPC were transferred onto mica or Si/SiO_x at surface pressures (π) equal to or greater than composition-dependent, LE-C transition pressures of the phospholipid mixtures. The transfer pressures are given in Table 4.3. Typical AFM images of the solid-supported films are shown in Figure 4.9. Patterns consisting of thicker parallel stripes (DPPC- or DSDPPC-enriched phase) surrounded by a thinner matrix (DLPC- or DSDLPC-enriched phase) are observed for all three mixtures. The condensed-phase stripe domains protrude above the LE or fluid background matrix by ~0.9 nm for DPPC/DLPC and DSDPPC/DLPC, and ~0.7 nm for DPPC/DSDLPC. The step-height difference measured by AFM between DPPC and DLPC corresponds well to the difference between half of a DPPC bilayer and half of a DLPC monolayer (0.85 nm).[1] The step-height difference between the condensed phase DSDPPC and the liquid expanded DLPC phase measured by AFM is lower than expected according to the thickness of DSDPPC obtained by ellipsometry (Table 3.3). Films of pure DSDPPC molecules formed at 18 mN m^{-1} and 32 mN m^{-1} are thickers than those of DPPC formed at comparable surface pressures possibly due to the $-SSCH_3$ chain of DSDPPC. When mixed with DLPC, the longer $–SSCH_3$ chain seems to be disordered enough to give a same step-height difference as DPPC/DLPC mixtures. This could be explained by less order of the protuding

–$SSCH_3$ chain when mixed with a lipid with a shorter chain compared to a homogeneous DSDPPC monolayer. DSDLPC chains order more in the presence of DPPC longer chains compared to the order found in pure DSDLPC film resulting in a smaller step-height between the condensed DPPC phase and the liquid expanded phase of DSDLPC than between DPPC and DLPC. A characteristic feature of all the patterns is that wider continuous stripes are periodically interspersed among a more closely spaced series of narrower broken stripes. Mixed monolayers of the 3:1 composition, containing more of the condensed-phase forming DPPC or DSDPPC versus the fluid-phase forming DLPC or DSDLPC, exhibit stripes that are approximately twice as wide as those of monolayers of equimolar composition. The mean stripe widths obtained from an analysis of the AFM images are given in Table 4.3. The center-to-center stripe spacing ranges from ~400 nm to ~3 μm. The stripe widths and spacings depend on the molar ratio of condensed phase to fluid phase phospholipid, film transfer pressure, and film transfer speed. Only a limited set of conditions was explored here, such that the narrowest DSDPPC stripe width of 145 nm reported in Table 4.3 should not be viewed as the lower limit of feature size that can be generated. Moraille and Badia previously obtained 60 nm-wide stripes from the LB transfer of a 0.15:0.85 DPPC/DLPC monolayer at high surface pressure.[9] A variety of patterns can also be obtained as described in Chapter 2. Micrometer-size, condensed circular domains co-exist with the stripes under the Langmuir monolayer formation and deposition conditions used in this work, as revealed by the larger field-of-view accessible in FEGSEM. In the 3:1 DSDPPC/DLPC monolayers, for example, there are typically 9 to 10 circular domains of ~10 to ~20 μm diameter in a 0.023 mm^2 area and the stripe motifs extend over areas ≥ 30 × 30 μm^2 DLPC (Figure 4.10B), while fewer (or no) domains are observed in the same size area for the 3:1 DPPC/DLPC (Figure 4.10A). Efforts to improve the regularity of the stripe motifs (i.e., uniformity of stripe widths and spacings) by varying the Langmuir monolayer formation and LB film deposition conditions were presented in Chapter 2.

The solid-supported monolayers generated herein have their ω-methyldithio (-SS-) groups exposed at the surface and their phosphocholine headgroups adsorbed to the mica or

Si/SiO_x. Assuming that DSDPPC and DSDLPC occupy roughly the same molecular areas in the stripes and background matrix of the phase-separated mixed monolayers as they occupy in the single component systems at a given film transfer pressure, we estimate 1.5 to 1.8 -SS- groups per nm^2 for the stripe domains of DSDPPC/DLPC and 0.96 to 1.1 -SS- groups per nm^2 for the background matrix of DPPC/DSDLPC.[15] These disulfide surface coverages should be taken as the theoretical or maximum values because the data presented in Figure 4.2 show a positive deviation between the experimentally determined mean molecular areas of binary mixtures and those calculated from the areas of the pure phospholipids using the additivity rule.[10]

Table 4.3 Average widths of the stripes in the mixed monolayer patterns.

Monolayer	$\pi_{\text{film transfer}}$ (mN m^{-1})	Width of continuous stripes[c] (nm)
DPPC/DLPC		
3:1 [a]	8	290 ± 140 (n = 119)
1:1 [b]	16	174 ± 73 (n = 92)
DPPC/DSDLPC		
3:1 [a]	12	480 ± 230 (n = 20)
1:1 [b]	18	170 ± 95 (n = 32)
DSDPPC/DLPC		
3:1 [a]	12	300 ± 160 (n = 181)
1:1 [b]	18	145 ± 60 (n = 73)

[a] Substrate withdrawal speed from A/W interface = 1 mm min^{-1}
[b] Substrate withdrawal speed from A/W interface = 5 mm min^{-1}
[c] Width of stripes measured from a random cross-section
n = number of lines width measurements, measurements done using at least three different images.

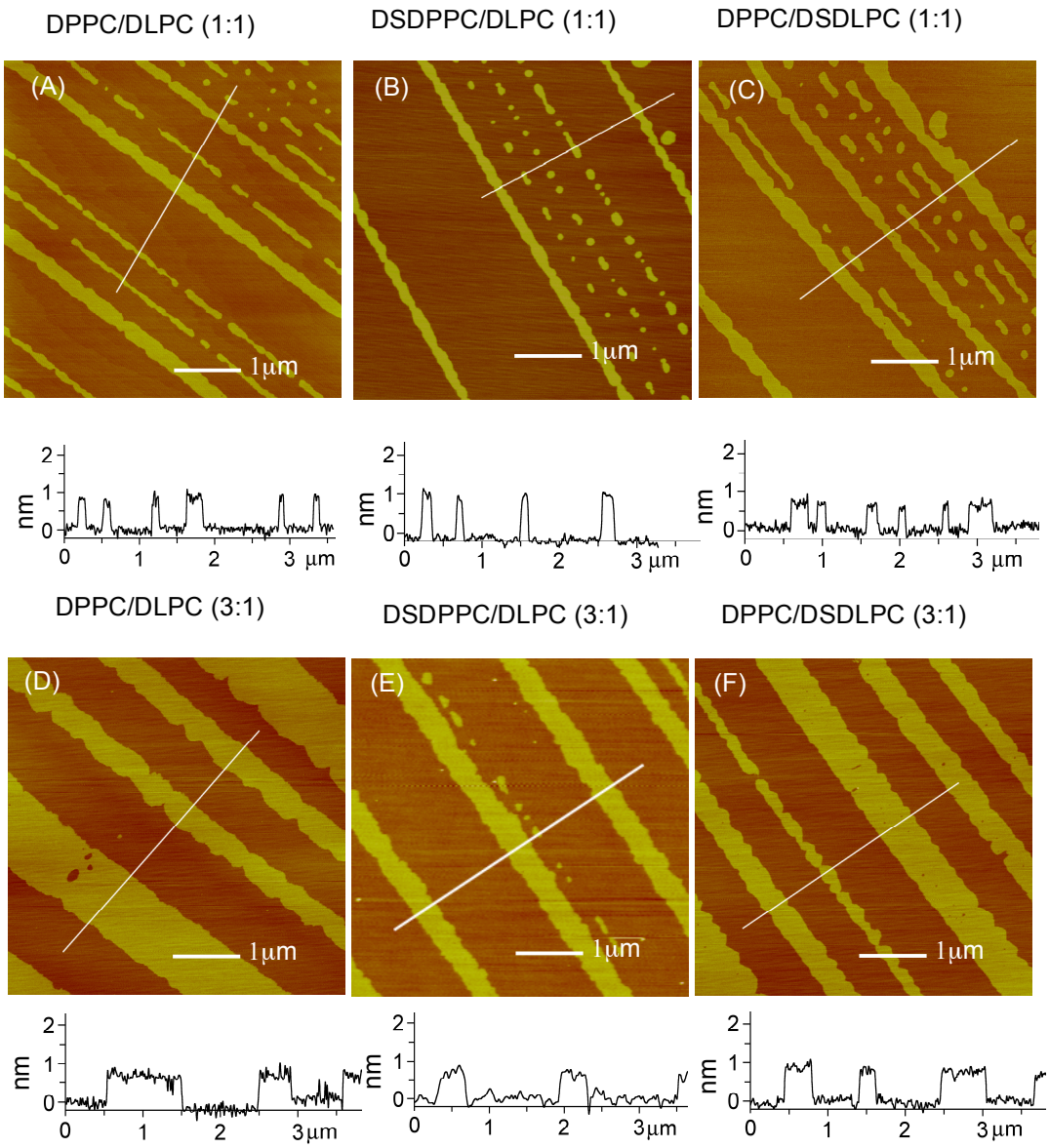

Figure 4.9 AFM images and line cross-sections of mica-supported LB films for 1:1 (mol:mol) mixtures of (A) DPPC/DLPC, (B) DSDPPC/DLPC, and (C) DPPC/DSDLPC and 3:1 (mol:mol) mixtures of (D) DPPC/DLPC, (E) DSDPPC/DLPC, and (F) DPPC/DSDLPC.

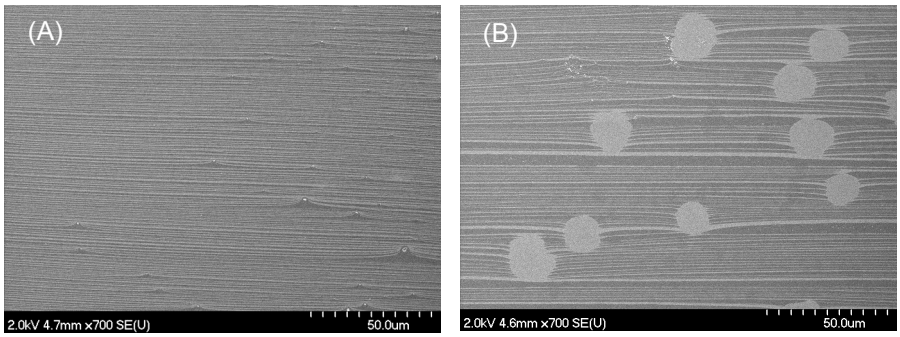

Figure 4.10 FEGSEM micrographs of LB films of (A) DPPC/DLPC and (B) DSDPPC/DLPC (3:1) on Si/SiO_x.

4.4 Conclusions

We have demonstrated the use of alkyl chain-derivatized phospholipids to laterally structure chemical functionalities into striped monolayers formed by the Langmuir-Blodgett or Langmuir-Schaefer transfer of phase-separated binary mixtures from the A/W interface onto solid substrates. Although the addition of a methyldisulfide group at one of the tail ends of DPPC and DLPC leads to differences in the phase behaviour at the A/W interface, a stripe pattern is obtainable by LB from mixtures of the unmodified and modified phospholipids. These chemically heterogeneous patterns pave the way to additional functionalization through the exposed disulfide groups and chemisorbed patterns on gold via S-Au adsorption.

4.5 References

(1) Marsh, D. *CRC Handbook of Lipid Bilayers*; CRC Press, Inc.: Boca Raton, FL, 1990.

(2) Sackmann. *FEBS Lett.* **1994**, *346*, 3.

(3) Mabrey, S.; Sturtevant, J. M. *Proc. Natl. Acad. Sci. USA* **1976**, *73*, 3862.

(4) Van Dijck, P. W. M.; Kaper, A. J.; Oonk, H. A. J.; De Gier, J. *Biochim. Biophys. Acta, Biomembr.* **1977**, *470*, 58.

(5) Lee, A. G. *Biochim. Biophys. Acta* **1977**, *472*, 285.

(6) Koynova, R.; Caffrey, M. *Chem. Phys. Lipids* **2002**, *115*, 107.

(7) Dietrich, C.; Bagatolli, L. A.; Volovyk, Z. N.; Thompson, N. L.; Levi, M.; Jacobson, K.; Gratton, E. *Biophys. J.* **2001**, *80*, 1417.

(8) Bagatolli, L. A.; Gratton, E. *Biophys. J.* **2000**, *79*, 434.

(9) Moraille, P.; Badia, A. *Langmuir* **2002**, *18*, 4414.

(10) Sanchez, J.; Badia, A. *Thin Solid Films* **2003**, *440*, 223.

(11) Badia, A.; Moraille, P.; Tang, N. Y. W.; Randlett, M.-E. *Int. J. Nanotechnol.* **2008**, *5*, 1371.

(12) Petty, M. C. *Langmuir-Blodgett Films. An Introduction*; Cambridge University Press: Cambridge, 1996.

(13) Gaines Jr., G. L. *Insoluble Monolayers at Liquid-Gas Interfaces*; Wiley: New York, 1966.

(14) Bittermann, A. G.; Jacobi, S.; Chi, L. F.; Fuchs, H.; Reichelt, R. *Langmuir* **2001**, *17*, 1872.

(15) Values were calculated from the molecular areas occupied by the pure phospholipids at the A/W interface at a given surface pressure.

Chapter 5 Self-Patterned Mixed Phospholipid Monolayers for the Spacially-Selective Deposition of Metals

5.1 Introduction

The alkyl tail-exposed disulfides of the solid-supported DSDPPC/DLPC or DPPC/DSDLPC monolayers open the possibility for the spatially-selective modification of the surface with metal and the construction of regular arrays of substrate-bound metallic wires or slits that are suited for studies of the relation between the width and spacing of the nanostructures and their surface plasmon properties,[1-3] electrical conductivity[4,5] or diffractive optics response.[6,7] Physical vapor deposition (PVD) of metal under vacuum was employed as a starting point because of its thermal compatibility with organic monolayer films. Alternate technologies such as chemical vapor deposition (CVD) and electroless deposition generally entail harsher conditions (i.e., thermal activation temperatures $\geq$ 200°C for CVD[8] and basic or acidic plating solutions for electroless deposition[9]) that are incompatible with phospholipid LB films.

5.2 Experimental Section

5.2.1 Materials

Refer to section 3.2.1 for the description of the materials used. Triton-X 100 (Ultrapure) was purchased from Sigma-Aldrich (St. Louis, MO).

5.2.2 Film Preparation

5.2.2.1 Langmuir-Blodgett Monolayer Film Preparation

Patterned LB films were prepared according to the method described in section 3.2.5.

5.2.2.2 Metal Vapor Deposition by Resistive Thermal Evaporation

Nominal metal thicknesses, ranging from 0.15 to 1.0 nm, were deposited at a rate of 0.1 Å s^{-1} onto the phospholipid-patterned mica or silicon using a VE-90 thermal evaporator equipped with a quartz crystal deposition monitor (Thermionics Vacuum Products, Port Townsend, WA). The metal evaporation process was initiated once a base pressure of < 5.5 x 10^{-7} Torr was attained and there was no cooling or heating of the substrates. The evaporation time ranged from 8 to 50 s, depending on the thickness of metal evaporated, and the maximal temperature attained near the rotating sample stage was 70 °C (evaporation source to sample distance of 38 cm). The deposited metal thicknesses reported in this article are the mass thicknesses indicated by the calibrated quartz crystal monitor.

5.2.2.3 Detergent Extraction

The solid-supported monolayer film temperature was lowered to 4 °C (measured with a thermocouple) by leaving the sample in the freezer for 10 min. The sample was then removed from the freezer, and 1 mL of an aqueous 1% v/v Triton X-100 solution (cooled to 4 °C before use) was used to cover a 1 cm^2 area. After 30 sec, the Triton X-100 drop was removed and the treated area was rinsed with water and blown dry with nitrogen. The sample was then imaged in air by AFM.

5.2.3 Characterization Techniques

XPS, FEGSEM, TOF-SIMS and AFM were performed according to the experimental conditions described in sections 3.2.6 and 4.2.2.

5.3 Results and Discussion

Resistive thermal evaporation was used to deposit different thicknesses of gold, silver, and copper onto the phospholipid monolayers. The atomic radii and corresponding

coverages of the different metals are given in Table 5.1. The nominal layer thicknesses of vapor-deposited metal reported are the average mass thicknesses indicated by a calibrated quartz crystal microbalance during metal evaporation. Gold-coated films were analyzed by XPS to confirm the presence of metal on the phospholipid surfaces and characterize the metal-disulfide interaction. FEGSEM and AFM were used to evaluate the spatial distribution of the metals on the surface of the mixed phospholipid patterns.[10]

Table 5.1 Atomic radii and nominal thicknesses of the thermally evaporated metals

	Atomic Radius (nm)	1 Monolayer (1 ML) (nm)	Nominal thickness of 0.15 nm (ML)	Nominal thickness of 0.25 nm (ML)
Gold (Au)	0.144	0.144	0.52	0.87
Silver (Ag)	0.144	0.288	0.52	0.87
Copper (Cu)	0.128	0.256	0.59	0.98

5.3.1 XPS Analysis

For all of the films analyzed, only the expected elements were observed: C, N, P, S, O, Si, and Au (Figure 5.1). We do not compare herein the expected atomic concentrations with those derived from XPS or report elemental ratios since the calculated atomic composition is sensitive to the XPS operating conditions, including the take-off angle, and the elemental distribution perpendicular to the surface, and variable angle measurements were not performed.[11] The presence of a doublet (Au4f) between 84 and 88 eV and peaks at ~335 and ~353 eV (Au4d) in the XPS survey scans following thermal evaporation confirmed the presence of Au on the mixed monolayer surfaces (Figure 5.1). High-resolution XPS scans were run on single-component monolayers in the condensed state

($\pi_{film\ transfer}$ = 20 mN m^{-1}) to increase the coverage of the ω-methyldithio groups at the DSDPPC monolayer surface and the intensity of the sulfur signal. The Au4f and S2p spectra lines were measured, as these are the core levels reported in studies of SAMs of alkanethiolates on planar gold substrates (RS-Au), alkanethiolate-capped Au nanoparticles, and polymeric Au(I)-thiolate complexes.[11-16] Typical $S2p_{3/2}$ binding energies (BEs) for non-bound *n*-alkylthiols (RSH) and *n*-alkyldisulfides (RSSR) range from 163 to 164 eV. Chemisorption of these two classes of organosulfur compound to gold substrates yields indistinguishable S2p spectra, indicating that both precursors form the same species on the surface.[13] The $S2p_{3/2}$ BE shifts to 162 eV,[11-16] a value indicative of a covalent gold-sulfur bond with thiolate-like character (i.e., the charge per S is about -0.2*e*)[15]. Although the photoelectron peak intensities of the $Au4f_{7/2}$ and $4f_{5/2}$ core levels are in some cases attenuated by the overlying SAM (long alkyl chain), their BEs remain at values expected for Au^0 after chemisorption of the thiol or disulfide.[11-15] The BE values obtained from a deconvolution of the high-resolution spectra of DPPC and DSDPPC with or without a 1 ML (0.30 nm) Au coating are presented in Table 5.2

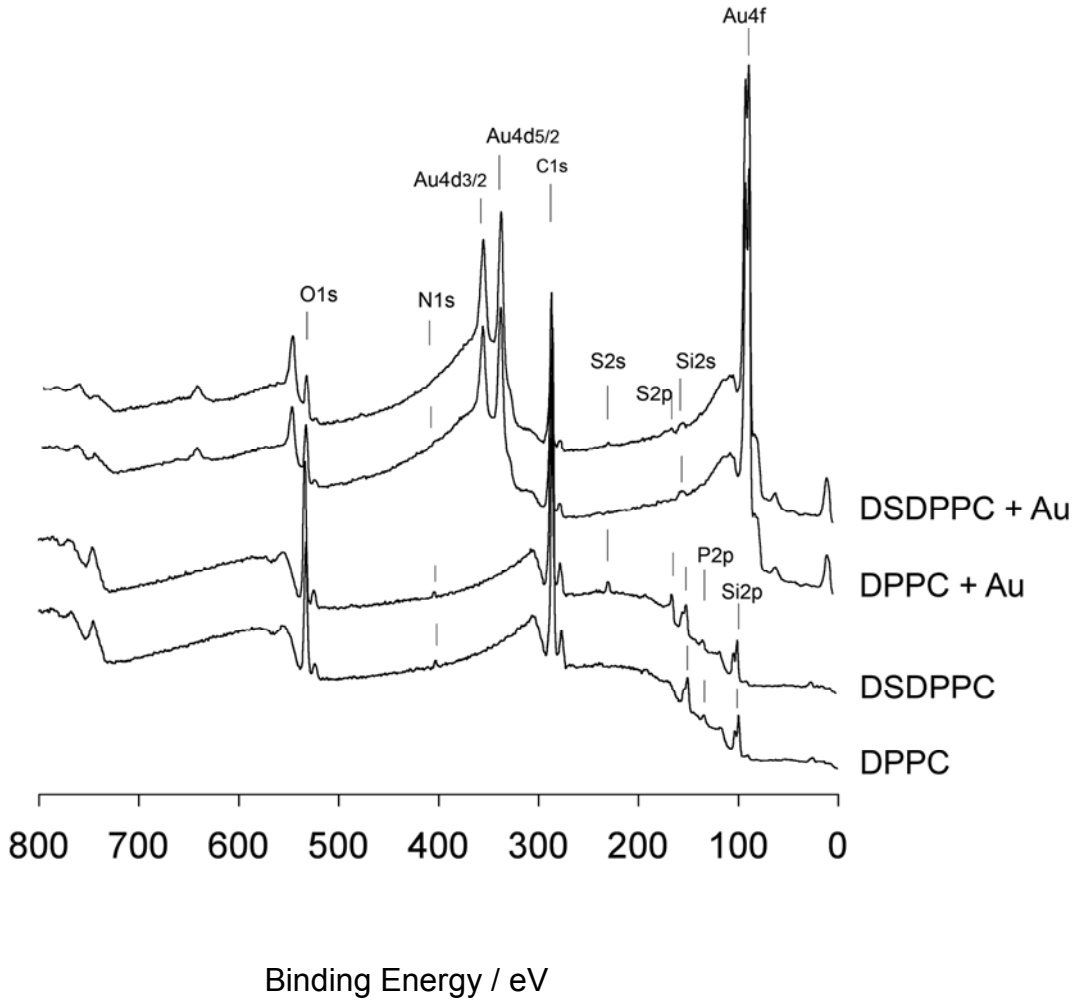

Figure 5.1 XPS Survey spectra of DPPC, DSDPPC, DPPC + 1 ML (0.30 nm) Au and DSDPPC + 1 ML (0.30 nm) Au.

Table 5.2 Binding energies from high-resolution XPS spectra of DPPC and DSDPPC with and without a 1 ML (0.30 nm) coating of Au.

Si/SiO_x-supported monolayer[a]	Binding energy (eV)	
	$Au4f_{7/2}$	$S2p_{3/2}$
DPPC + 1 ML Au (n = 1)	84.0	-
DSDPPC (n = 2)	-	163.0 ± 0.1
DSDPPC + 1 ML Au (n = 3)	83.9 ± 0.2	161.8 ± 0.6 (66 ± 10 %)[b] 163.4 ± 0.6 (34 ± 10 %)[b]

[a] $\pi_{\text{film transfer}}$ = 20 mN m^{-1}
[b] Relative atomic % for 2 contributions
n = number of sample analyzed

The Au4f spectra were fitted using one doublet with splitting of 3.7 eV (Figure 5.2A and B). The $Au4f_{7/2}$ BEs of 83.9-84.0 eV correspond to Au^0. As in the case of RS-Au SAMs, there is neither a Au(I)-associated peak (BE ≈ 84.3 eV)[15], nor is there evidence for more than one Au state in the spectrum of the Au-coated DSDPPC. The S2p spectrum of DSDPPC (Figure 5.2C) shows an asymmetric peak, which could be fitted using a doublet of area ratio of 2:1 and splitting of 1.2 eV (i.e., the spin-orbital-coupled doublet of this core level is unresolved under the acquisition conditions employed). The $S2p_{3/2}$ BE of 163.0 eV is well within the range of values reported for free thiols and disulfides. The S2p spectrum of the Au-coated DSDPPC is shown in Figure 5.2 D. The presence of a Au overlayer attenuates the spectral intensity. The S2p peak can be fit reasonably well, despite the noise in the spectrum, as two doublets with area ratios of 2:1 and splittings of 1.2 eV. The $S2p_{3/2}$

BEs are 161.8 and 163.4 eV. These values are attributable to a gold-bound thiolate species and to unbound disulfide moieties. The dissociative addition of DSDPPC to Au can yield Au-SCH_3 (assuming a stable surface CH_3S-Au species can form)[17] and Au-SDPPC. Our XPS data (S2p, C1s) does not allow us to establish whether both gold-thiolates are formed or whether Au-SDPPC is the predominant species.[18,19]

Future characterization work will make use of spontaneous desorption time-of-flight mass spectrometry for identification of the gold-bound surface species.[20]

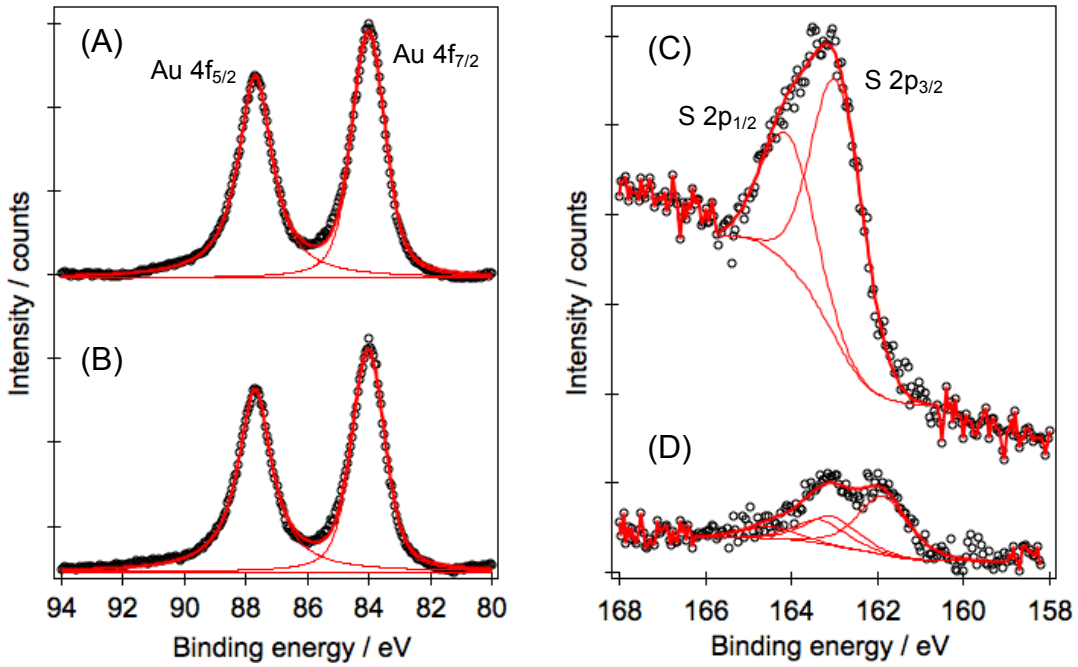

Figure 5.2 High resolution XPS spectra. Au 4f doublet for (A) DPPC and (B) DSDPPC + 1 ML of Au. S2p spectra of (C) DSDPPC, and (D) DSDPPC + 1ML of Au

The relative area contribution of the bound thiolate peak to the $S2p_{3/2}$ signal suggests that ~66% of the sulfurs are bound to Au.[21] It is unlikely that the non-bound population (~34%) is CH_3SSCH_3 byproduct from a preferential reaction of -SDPPC with Au as this highly volatile compound (vapor pressure of 3.8 kPa at 20 °C)[22], if formed,

should be pumped off the surface in the vacuum chambers of the metal evaporator (base pressure ≈ 10^{-7} Torr) and XPS instrument (≈ 10^{-9} Torr). The signal at 163 eV is most likely due to non-reacted DSDPPC. The presence of free methyldithio groups cannot be ascribed to an insufficient quantity of evaporated Au (i.e., 1 ML) on the DSDPPC surface given that the Au:S ratio is ~4:1,[23] and that Au/S stoichiometries of 3:1, 2:1, and 1:1 are necessary to fulfill the range of Au (surface):S ratios reported for RS-Au SAMs on extended (planar) and finite (nanoparticle) surfaces.[15,24] The incomplete reaction may be due to the formation of Au clusters, as opposed to a continuous monoatomic layer, on the DSDPPC surface (vide infra Figure 5.6), with only the Au atoms in direct contact with the underlying DSDPPC surface reacting with the -SS- groups. However, differences in reactivity between the solid (disulfide)/gas (Au) configuration used herein and the solid (Au)/solution (disulfide) configuration typically used for the self-assembly of RSH or RSSR on metals cannot be excluded. In summary, XPS establishes that there is reaction of the solid DSDPPC film surface with the evaporated Au atoms to form a gold-thiolate species.

5.3.2 FEGSEM Imaging

Various reports have demonstrated the secondary electron mode of FEGSEM to be extremely sensitive at low acceleration voltages to variations in surface composition and structure.[25] The contrast observed in micrographs is due to spatial variations in the surface work function and secondary electron emission between the different molecular components. Figure 5.3 shows FEGSEM images of Si/SiO_x-supported monolayers. The 3:1 mixtures were used for FEGSEM because the larger stripes (i.e., mean widths of 300 - 500 nm) are better resolved. The condensed stripe domains and LE background matrix appear as parallel bands of different contrast. The secondary electron emission intensity of the larger circular domains of condensed phospholipid was used to identify the linear regions of the image that are condensed phase stripes and those that are the fluid phase background. The light gray circular domains and stripes (high emission intensity) in the micrographs of the bare monolayers (Figure 5.3A-C) are attributable to the condensed phase of DPPC or

DSDPPC and the surrounding dark regions (low emission intensity) are the DLPC- or DSDLPC-containing fluid matrix.

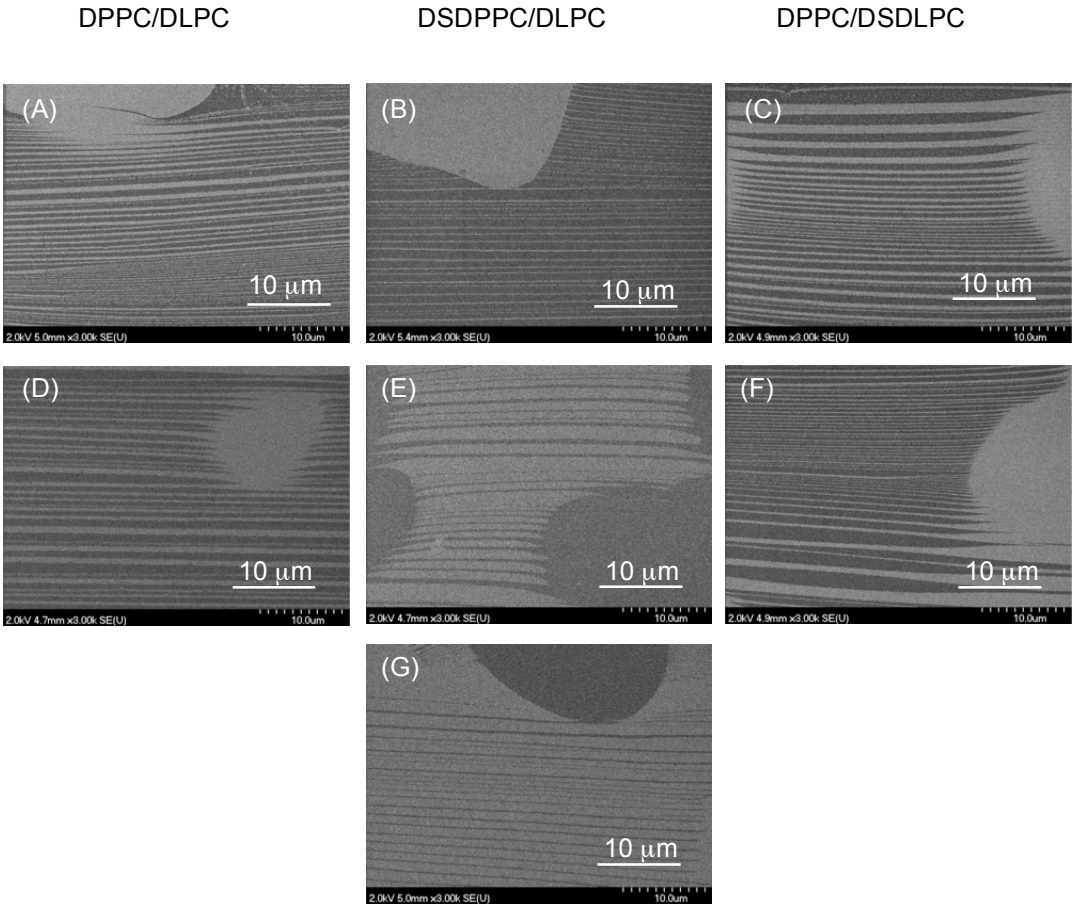

Figure 5.3 FEGSEM micrographs of Si/SiO_x- supported LB monolayers formed from 3:1 mixtures. (A) DPPC/DLPC, (B) DSDPPC/DLPC, and (C) DPPC/DSDLPC. (D) DPPC/DLPC, (E) DSDPPC/DLPC, and (F) DPPC/DSDLPC coated with 0.87 ML (0.25 nm) of Au. (G) DSDPPC/DLPC coated with 2 ML (0.60 nm) of Au.

This assignment is consistent with previous work in which Bitterman *et al*.[26] imaged chemically homogeneous phospholipid monolayers with domains of varying molecular

packing density and found that regions with higher packing density (condensed phase) emit more secondary electrons and exhibit a higher intensity in FEGSEM images than areas of lower packing density (LE phase). That the same contrast is observed for the chemically homogeneous DPPC/DLPC monolayer and the chemically heterogeneous DSDPPC/DLPC and DPPC/DSDLPC films indicates that the secondary electron emission intensity is dominated by the molecular packing density under the given operating conditions. Figure 5.3D-F are the micrographs after the evaporation of 0.87 ML (0.25 nm) of Au. An inversion of contrast is observed in the case of DSDPPC/DLPC (Figure 5.3E vs. 5.3B), which persists after the evaporation of 2 ML (0.60 nm) of Au (Figure 5.3G). The DSDPPC-enriched circular domains and stripes are darker (lower intensity) than the surrounding DLPC-containing matrix. No such contrast inversion occurs in the chemically homogeneous DPPC/DLPC monolayer (Figure 5.3D vs. 5.3A), which should be uniformly covered with gold.[27] The gold coating attenuates the secondary electron emission from the DSDPPC-enriched domains, rendering it weaker than that of the DLPC background. Two different effects can cause the observed signal attenuation: (i) the preferential location of the evaporated gold in the reactive DSDPPC regions, with or without formation of a Au-thiolate bond between some of the Au atoms and the methyldithio endgroups or (ii) formation of Au-thiolate species on the DSDPPC domains of a fully gold-covered surface. We will return to the likely origin of the FEGSEM contrast later on in the discussion. No attenuation of the DSDLPC background matrix with respect to the DPPC domains is evident in the complementary DPPC/DSDLPC system because the secondary emission intensity is already low in the absence of deposited gold (Figure 5.3F vs. 5.3C).

5.3.3 TOF-SIMS Imaging

DPPC/DLPC and DSDPPC/DLPC (1:1) monolayers coated with 0.52 ML of gold were characterized by TOF-SIMS. The mapping of PO_2, PO_3, S and Au is presented in Figure 5.4. As expected, the sulfur signal is absent in the DPPC/DLPC film and present in the condensed domains of DSDPPC/DLPC. The PO_3 signal is fairly homogeneous in the DPPC/DLPC monolayer. A very faint decrease in phosphate intensity is observed in parts of the film (circled area in Figure 5.4A). The PO_3 signal in the DSDPPC/DLPC film is not homogeneous, and an absence of PO_3 is detected in the condensed domains (see domain correlation with S signal). TOF-SIMS is a surface analysis tool (1-3 monolayer depth profile), any element buried too far from the interface will not be detected. When 0.52 ML of gold is deposited onto the monolayers, the PO_3 signal in the condensed domains is shielded by the presence of a thicker layer of gold, supporting the fact that a preferential adsorption of gold occurs onto the condensed domains containing the –SS- functionality. Shielding of the PO_3 signal also occurs in the DPPC/DLPC monolayers but it is barely noticeable, suggesting that the gold deposits in a more homogeneous fashion over the monolayer and the absence of PO_3 can simply be due to the condensed domains being slightly thicker than the fluid background. Gold is detected homogeneously over the DPPC/DLPC and DSDPPC/DLPC monolayers because the lateral resolution of TOF-SIMS is > 100 nm and as seen in Figure 4.5, condensed lipd domains are found between the larger ones.

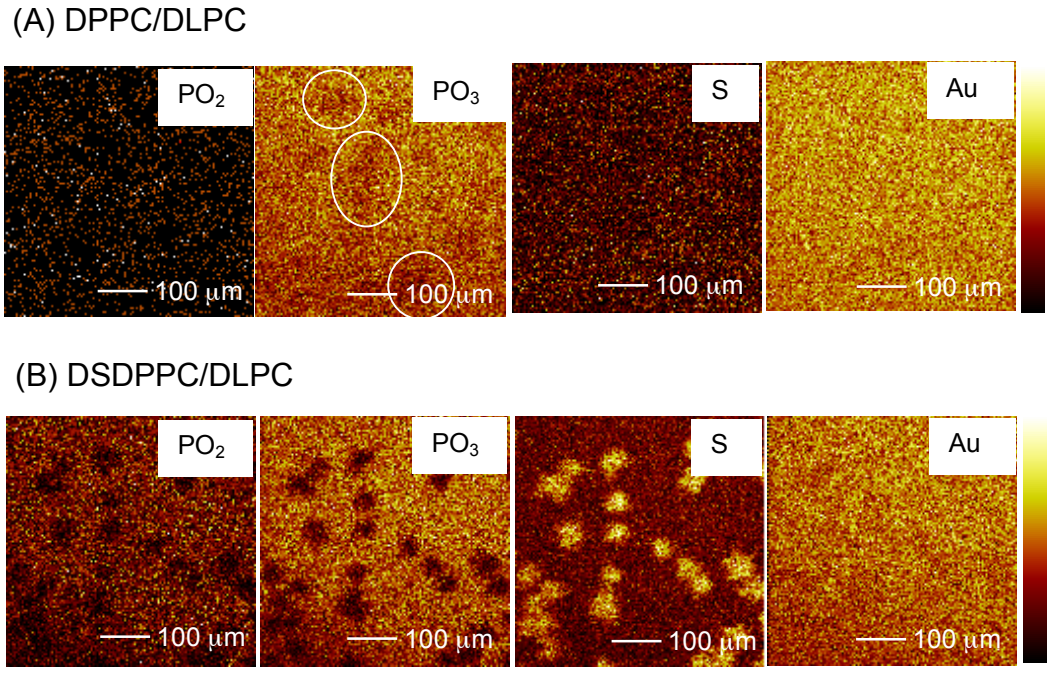

Figure 5.4 TOF-SIMS images (500 x 500 μm) of 1:1 (mol/mol) monolayers supported on Si/SiO_x of (A) DPPC/DLPC circled area show lower PO_3 intensity, and (B) DSDPPC/DLPC covered with 0.52 ML of Au.

5.3.4 AFM Imaging

To rationalize the differences in image contrast observed in FEGSEM for the different gold-coated monolayer surfaces, the stripe-to-background matrix step height (Δh) and film morphology were analyzed by tapping-mode AFM. Figure 5.5 shows topography images of 1:1 mixed monolayer films after deposition of 0.52 ML (0.15 nm) of Au. The stripe-to-background height difference ($\Delta h \approx 0.9$ nm) remains the same for the non-functionalized DPPC/DLPC pattern (Figure 5.5A), consistent with a homogeneous distribution of Au across the surface. In the case of the DSDPPC/DLPC template, where the -SS- moieties are located in the stripe domains (Figure 5.5B), Δh increases by 0.3 nm, suggesting the preferential (but not necessarily exclusive) accumulation of gold onto the

stripes. When the -SS- groups are localized in the background matrix phase (DPPC/DSDLPC), there is no obvious change in step height (within the standard deviation) after the evaporation of 0.5 ML of Au (Figure 5.5C).

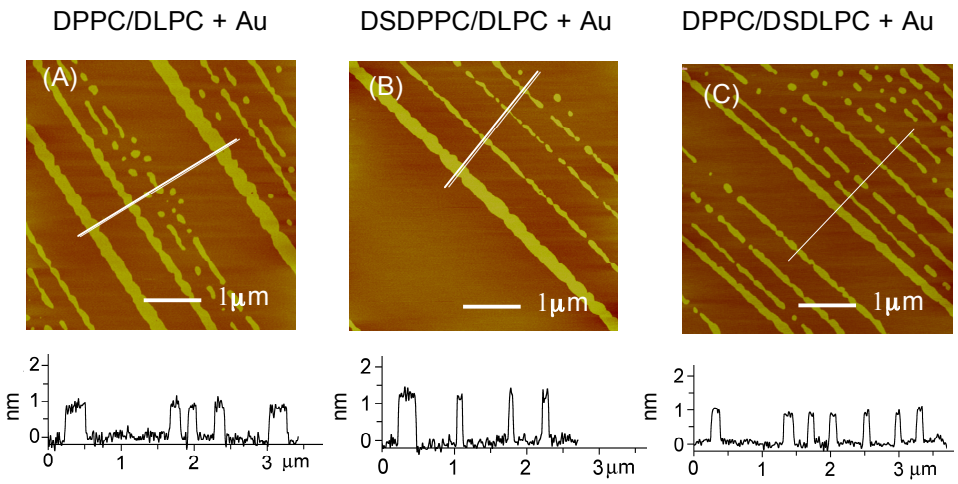

Figure 5.5 AFM images and line sections of 1:1 mixtures of (A) DPPC/DLPC, (B) DSDPPC/DLPC, and (C) DPPC/DSDLPC coated with 0.52 ML (0.15 nm) of Au.

However, cold detergent extraction of the unprotected lipid phase reveals that the Au is concentrated at the DSDLPC matrix (vide infra Figure 5.7). Because of the more disordered fluid nature of the background phase, the selectivity of the Au deposition onto DPPC/DSDLPC could not be evaluated through AFM measurements of the step height.

The deposition of silver and copper onto the 1:1 DSDPPC/DLPC pattern was also investigated (Table 5.3). Both metals behaved like gold at submonolayer coverages - an increase in the step height is observed when 0.5 to 0.6 ML of metal is thermally evaporated onto the DSDPPC/DLPC pattern. In all cases, the increase in Δh of 0.3 - 0.5 nm is larger than the nominal thickness of metal evaporated (i.e., 0.15 nm).

Table 5.3 AFM-measured step heights on DSDPPC/DLPC (1:1) monolayers before and after metal evaporation.

Average layer thickness of evaporated metal[a] (nm)	Step height (nm)		
	Au	Ag	Cu
0	0.90 ± 0.07	0.90 ± 0.07	0.90 ± 0.07
0.15	1.22 ± 0.10	1.36 ± 0.10	1.28 ± 0.08
0.25	1.26 ± 0.10	1.16 ± 0.11	0.96 ± 0.09

[a] As indicated by a quartz crystal microbalance during thermal evaporation

Cluster-like features are clearly visible on the DSDPPC stripes in high-resolution topography, and in some cases phase, images of metal-coated DSDPPC/DLPC films (Figure 5.6E, G, I). No such features are discernable on the metal-coated DPPC stripes (Figure 5.6C). These clusters presumably form via reaction of the metal vapor with the -SS- moieties, followed by metal-metal aggregation. Due to the surface roughness of the underlying DSDPPC stripes and AFM tip convolution effects (tip radius of curvature $\lesssim$ 10 nm), it was not possible to obtain accurate cluster sizes.

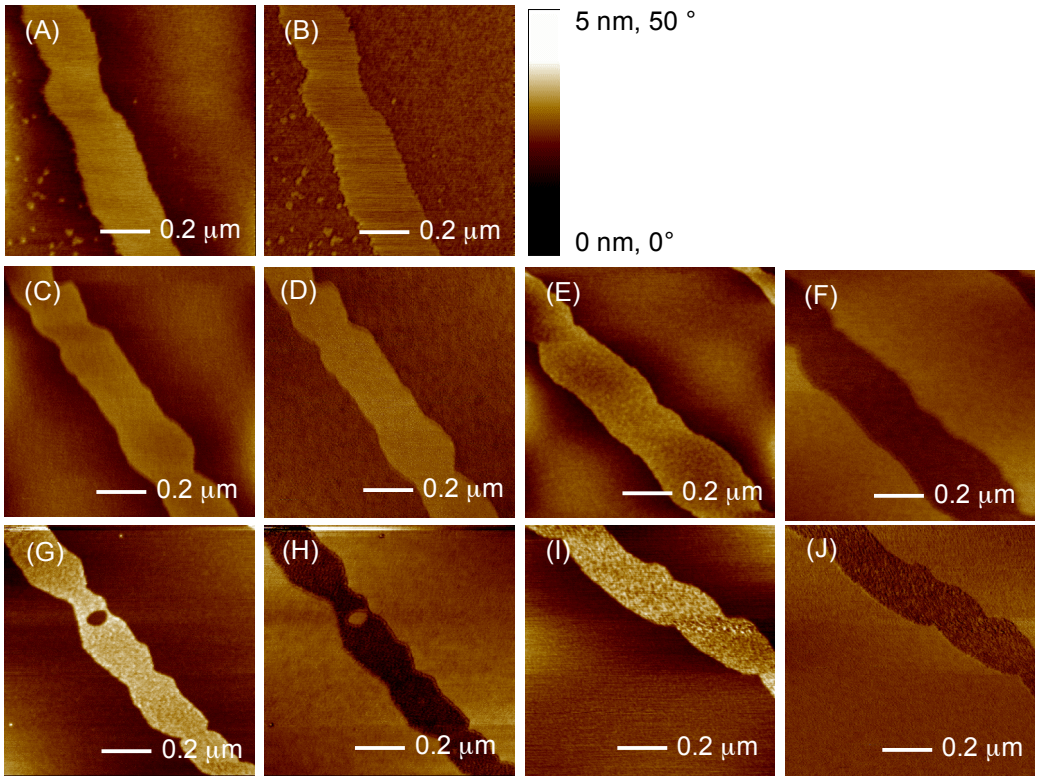

Figure 5.6 AFM images of (1:1) mixed monolayers. DSDPPC/DLPC (A) topography and (B) phase; DPPC/DLPC + 0.52 ML (0.15 nm) Au (C) topography and (D) phase; DSDPPC/DLPC + 0.52 ML of Au (E) topography and (F) phase; DSDPPC/DLPC + 0.87 ML (0.25 nm) Ag (G) topography and (H) phase; DSDPPC/DLPC + 0.52 ML (0.13 nm) Cu (I) topography and (J) phase.

The phase imaging mode of tapping mode AFM was used to further characterize the metal-coated patterns. Phase imaging goes beyond topography to detect spatial variations in mechanical and chemical properties. The phase images of the bare DPPC/DLPC[28] and DSDPPC/DLPC monolayers (Figure 5.6B) exhibit a positive shift of ~2.5º over the stripes compared to the background phase. A positive phase shift indicates that the stripes are stiffer than the background, consistent with the solid-like nature of DPPC and DSDPPC (stripes) compared to the fluid-like DLPC (background matrix),[28] The unmodified DPPC stripes of the DPPC/DLPC monolayer, for which the topography images indicate a uniform distribution of metal across the surface, retain their positive shift (2.5º) after metal evaporation (Figure 5.6D). By contrast, images of DSDPPC/DLPC, onto which 0.5 - 0.9 ML of Au or Ag or 0.6 ML of Cu are evaporated, consistently show a reversed phase contrast over the stripes. A negative phase shift ranging between 2 to 7° is observed over the DSDPPC stripes vs. the background DLPC phase (Figure 5.6F, H, J), suggesting that their mechanical and/or chemical properties have been selectively altered by the deposition of an ultrathin metal layer.

5.3.4.1 Cold Detergent Extraction

Evidence for the spatial localization of the metal deposits was sought using cold detergent (Triton X-100) extraction. Cold non-ionic detergent is commonly used in biology to solubilize and remove lipids from cell membranes.[29,30] We reasoned that the presence of metal deposit should prevent the underlying phospholipid from being removed from the mica surface by the detergent. The bare (uncoated) monolayer patterns are destroyed by the detergent treatment. The DPPC/DLPC monolayer covered with 0.5 ML of Au is unaffected by treatment with cold Triton X-100. The stripe-to-background step height remains the same after detergent treatment (Figure 5.7A vs. 5.5A), indicating that the evenly distributed Au layer acts as a protective barrier against the detergent. Figure 5.7B shows a DSDPPC/DLPC monolayer covered with 0.5 ML of Au following cold detergent extraction. The Δh increases from 1.2 ± 0.1 nm (before, Figure 5.5B) to 3.6 ± 0.5 nm (after,

Figure 5.7B), a value consistent with the thickness of a bare DSDPPC monolayer, 3 nm (measured by AFM in section 3.3.1), plus the thickness of Au on top of the stripes, 0.3 nm (i.e., Δh increase following Au evaporation).

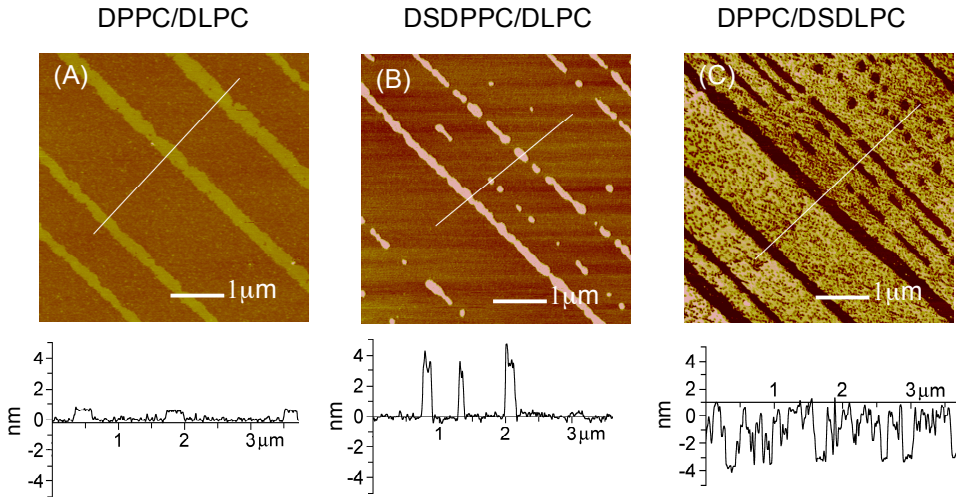

Figure 5.7 AFM images and line cross-sections of 1:1 mixtures of (A) DPPC/DLPC, (B) DSDPPC/DLPC, and (C) DPPC/DSDLPC coated with 0.52 ML (0.15 nm) of Au followed by Triton X-100 extraction.

This increase in step height, from 1.2 to 3.6 nm, is therefore attributable to the removal, by the detergent, of the unprotected DLPC phase from the laterally-differentiated monolayer film, leaving the gold-covered DSDPPC stripes untouched. Similarly, when the gold-covered DPPC/DSDLPC monolayer is treated with Triton X-100, the unprotected DPPC is removed from the pattern, resulting in linear grooves and circular holes of ~ 4 nm depth, as shown in Figure 5.7 C.

We proceeded to use the Δh measured after cold detergent extraction of DSDPPC/DLPC monolayers coated with increasing Au thicknesses as an indicator of the extractable (i.e., non-coated or poorly coated) DLPC phase (Figure 5.8 and 5.9). The step

height decreased from ~3.6 nm for 0.5 ML Au to ~2.2 nm for 1.0 ML Au. For 2.1 ML of evaporated Au, the step height of ~1.5 nm is close to the value of ~1.2 nm measured before detergent treatment. This trend points to an increasing coverage of Au on the DLPC matrix. There is clearly no preferential accumulation of Au on the stripes at coverages of vapor-deposited metal ≥ 1 ML.

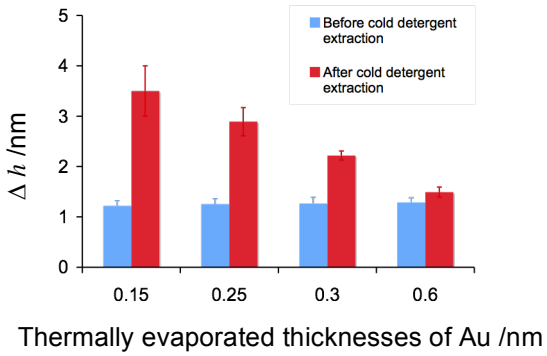

Figure 5.8 Bar graph of step-height differences before and after cold detergent extraction.

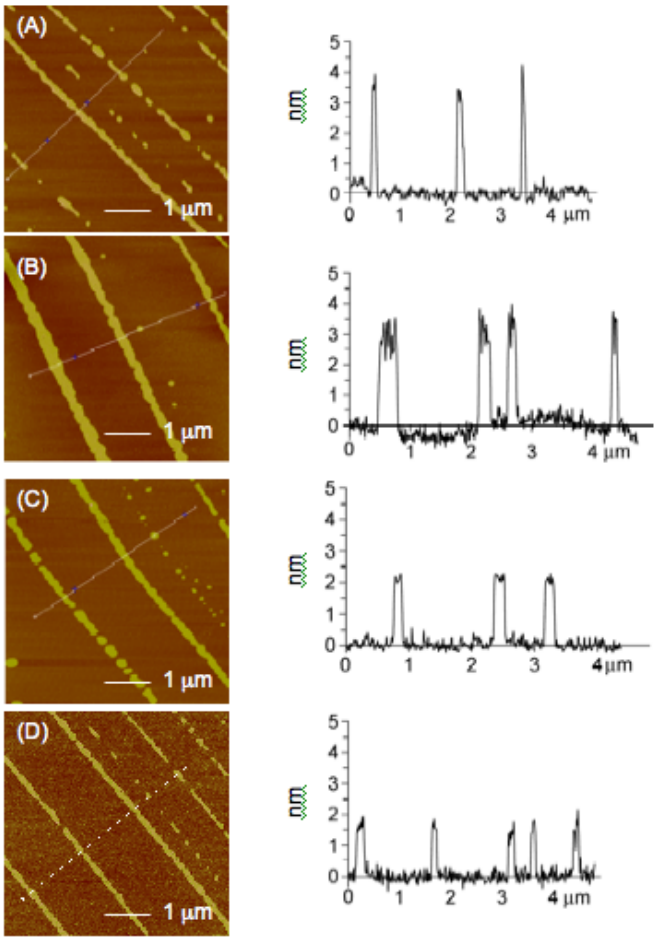

Figure 5.9 AFM images (5 µm x 5 µm) and line sections of DSDPPC/DLPC (1:1) coated with (A) 0.52 ML (0.15 nm) of Au, (B) 0.87 ML (0.25 nm) of Au, (C) 1 ML (0.30 nm) of Au and (D) 2 ML (0.60 nm) of Au after cold detergent extraction.

5.3.4.2 Selectivity of the Metal Deposition Versus Evaporated Metal Thickness

Having established some preference of the metal for the ω-methyldithio-containing regions at sub-ML coverages, we proceeded to determine the quantity of metal that could be thermally evaporated before the observed selectivity is lost. Plots of Δh vs. the nominal thickness of Au evaporated onto 1:1 DPPC/DLPC and DSDPPC/DLPC patterns are shown in Figure 5.10. As expected for the uniform adsorption of metal across the unmodified DPPC/DLPC surface, Δh is constant at 0.9 ± 0.1 nm for evaporated Au thicknesses from 0 to 2.1 ML (0.60 nm). For DSDPPC/DLPC, Δh increases by ~ 0.29 nm on going from 0 to 0.28 ML (0.08 nm) of Au and remains at ~ 0.3 nm up to 2.1 ML (0.60 nm) of Au. The data presented in Figure 5.10 implies that the selectivity of the Au for the DSDPPC stripes is already lost above ~ 0.28 ML (0.08 nm), the smallest quantity of Au that can be reliably deposited using our metal evaporator.

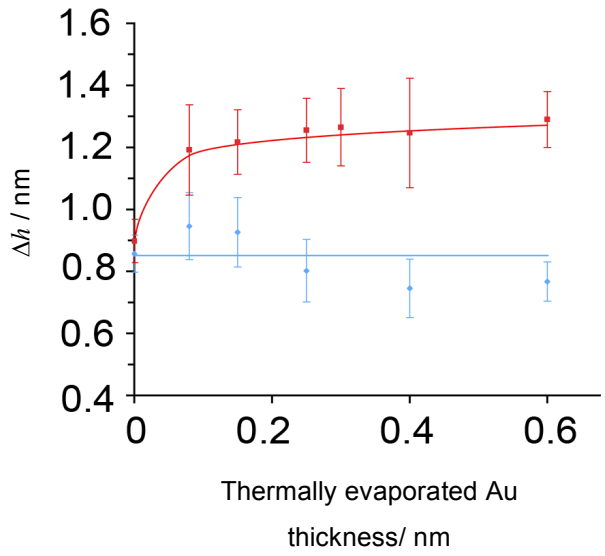

Figure 5.10 Step height (Δh) vs. the nominal thickness of Au evaporated onto 1:1 DPPC/DLPC (blue) and DSDPPC/DLPC (red) patterns. Line and curve serve as guides to the eye.

If the stoichiometry of Au:S ratio is 1:1, an equimolar DSDPPC/DLPC mixture (i.e., assuming 1.8 -SS-/nm^2 and 42% area coverage by the stripes) will saturate at an average thickness of 0.1 ML or 0.03 nm which would explain the lost of selectivity at 0.28 ML. Similar results were obtained for Ag and Cu (Table 5.4), although these metals were not studied in as much detail as Au. The DSDPPC/DLPC step height decreases as the nominal evaporated metal thickness increases from 0.15 to 0.25 nm, indicating a clear loss of preference of Ag and Cu on the DSDPPC pattern. The non-selective nature of the metal deposition demonstrated by the cold detergent extraction experiment and AFM measurements of the step height at evaporated Au thicknesses of 1 ML and 2 ML suggest that the contrasts observed for the metal-coated DSDPPC/DLPC in FEGSEM (Figure 5.3E, G) and AFM phase imaging (Figure 5.6) originate from the formation of a metal-thiolate species on the reactive DSDPPC domains rather than reflecting the absence of metal in the DLPC background

The very limited selectivity in metal vapor deposition observed with the chemically-differentiated phospholipid-based pattern is in marked contrast with the highly selective aggregation of metals reported for ultrathin diblock copolymer films based on the preferential wetting of one block, polystyrene (PS) versus another, poly(methylmethacrylate) (PMMA) or poly(2-vinylpyridine) (P2VP), by metal. This differential wetting leads the diffusing metal atoms to aggregate inside domains of the block for which there are favorable, non-covalent polymer/metal interactions. For PS-b-P2VP films consisting of hemi-spherical PS micelles of 150 nm diameter, 9 nm height, and 350 nm lateral spacing in a P2VP matrix, ~5 nm or 29 ML of titanium (Ti) could be thermally evaporated on the diblock copolymer film surface before the preferential accumulation of the Ti on the PS micelles ceased.[31] For PS-b-PMMA films comprised of cylindrical domains of 50 nm lateral spacing, nearly 100% selectivity of the Ag for the PS domains is observed by transmission electron microscopy (TEM) at an evaporated thickness of 12 nm (42 ML).[5] In the case of a structured monolayer surface consisting of 800 nm-wide DPPC stripes (advancing water contact angle = 47 ± 1º) separated by 200 nm-wide mica channels (advancing water contact angle = 8 ± 1º), the thermal evaporation

of 2-3 nm (7-10 ML) of Ag resulted in a preferential adsorption to the hydrophilic channels. [32, 33] It is clear from the step heights measured before and after metal evaporation for DPPC/DLPC that the inherent contrast in the surface energies of the liquid-expanded (~ 31 mJ m^{-2}) and condensed (~23 mJ m^{-2}) phospholipid phases does not lead to the preferential wetting by metal of the surrounding matrix (LE) versus the stripes (condensed).[34] It is the affinity of the metal for the sulfur that steers the diffusing Au atoms to the surface-exposed disulfide groups of the mixed monolayer. However, once a significant number of the available disulfides have reacted and/or are covered with metal, there is little (or no) physico-chemical preference for the incoming metal atoms to deposit on the surface of the metal clusters versus the unfunctionalized phospholipid phase, and the selectivity of the deposition is lost.

5.4 Conclusions

By using mixtures of DSDPPC/DLPC or DPPC/DSDLPC, metal-reactive -$SSCH_3$ groups were localized in either the condensed stripe domains or fluid background matrix. XPS shows that the surface -$SSCH_3$ groups react with the vapor-deposited metal atoms to form a metal-thiolate species. The AFM step height and cold detergent extraction results presented are consistent with a preferential adsorption of Au, Ag, and Cu atoms onto the -$SSCH_3$ enriched areas of the stripe patterns at submonolayer coverages of the metal.

Our work however demonstrates that the selective metallization of patterned organic monolayer surfaces via reaction of metal vapor with organosulfur groups is not a viable route to fabricating continuous metal nanostructures. For fundamental studies in areas such as surface plasmon optics and electronic transport, thicker, continuous metal deposits are generally required.[2, 5, 35, 36] This would involve the selective deposition of at least 10 nm of metal on the DSDPPC or DSDLPC areas of the mixed pattern. In related work with mixed SAMs of different surface reactivity (-SH vs. -CH_3) formed by microcontact printing, C. Winter *et al*.[37] found organometallic chemical vapor deposition

(OMCVD) to be much more effective in the area-selective deposition and growth of gold layers (~25 nm thick) than thermal evaporation. Future work will thus focus on OMCVD of precursors that decompose/vaporize at T < 100°C under vacuum or atmospheric pressure (i.e., compatibility with the thermally-sensitive phospholipid monolayers) and have been shown to deposit on thiol-terminated SAMs, for example $[(CH_3)_3]PAuCH_3$,[37] Hg,[38] and Al[39]. The use of these chemically-differentiated mixed monolayers as primary patterns for the area-selective adsorption of Au and Ag nanoparticles, that are transformable into continuous nanostructures by oxygen plasma treatment, will also be pursued as an avenue to fabricating nanopatterned metal structures.[40]

5.5 References

(1) Jara, A.; Arias, R. E.; Mills, D. L. *Phys. Rev. B* **2010**, *81*, 085422.

(2) Stewart, M. E.; Anderton, C. R.; Thompson, L. B.; Maria, J.; Gray, S. K.; Rogers, J. A.; Nuzzo, R. G. *Chem. Rev.* **2008**, *108*, 494.

(3) Lee, K.-L.; Wang, W.-S.; Wei, P.-K. *Plasmonics* **2008**, *3*, 119.

(4) Chai, J.; Wang, D.; Fan, X.; Buriak, J. M. *Nature Nanotechnol.* **2007**, *2*, 500.

(5) Lopes, W. A.; Jaeger, H. M. *Nature* **2001**, *414*, 735.

(6) Bailey, R. C.; Nam, J.-M.; Mirkin, C. A.; Hupp, J. T. *J. Am. Chem. Soc.* **2003**, *125*, 13541.

(7) Goh, J. B.; Loo, R. W.; Goh, M. C. *Sensor Actuat. B-Chem.* **2005**, *106*, 243.

(8) Lu, P.; Walker, A. V. *Langmuir* **2007**, *23*, 12577.

(9) Mallory, G. O.; Hajdu, J. B. *Electroless Plating: Fundamentals and Applications*; American Electroplaters and Surface Finishers Society: Orlando, FL, 1990.

(10) We do not presently have access to a TOF-SIMS and Scanning Auger Microscope with sufficient lateral resolution (< 100 nm) to perform compositional mapping of our functionalized stripe patterns.

(11) Bain, C. D.; Troughton, E. B.; Tao, Y. T.; Evall, J.; Whitesides, G. M.; Nuzzo, R. G. *J. Am. Chem. Soc.* **1989**, *111*, 321.

(12) Castner, D. G.; Hinds, K.; Grainger, D. W. *Langmuir* **1996**, *12*, 5083.

(13) Bain, C. D.; Biebuyck, H. A.; Whitesides, G. M. *Langmuir* **1989**, *5*, 723.

(14) Laibinis, P. E.; Whitesides, G. M.; Allara, D. L.; Tao, Y. T.; Parikh, A. N.; Nuzzo, R. G. *J. Am. Chem. Soc.* **1991**, *113*, 7152.

(15) Bourg, M.-C.; Badia, A.; Lennox, R. B. *J. Phys. Chem. B* **2000**, *104*, 6562.

(16) NIST X-ray Photoelectron Spectroscopy Database, Reference Database 20, Version 3.5, 2003.

(17) Nuzzo, R. G.; Zegarski, B. R.; Dubois, L. H. *J. Am. Chem. Soc.* **1987**, *109*, 733.

(18) Heister, K.; Allara, D. L.; Bahnck, K.; Frey, S.; Zharnikov, M.; Grunze, M. *Langmuir* **1999**, *15*, 5440.

(19) The self-assembly of asymmetric *n*-dialkyl disulfides (R_1SSR_2), where $R_1 << R_2$, under typical solution conditions gives large deviations from the expected 1:1 R_1S-:R_2S- surface composition. The SAMs formed consist predominantly of the longer chain R_2S-Au species, due to a surface/solution exchange mechanism which results in an almost complete substitution of the adsorbed shorter chains of the SAMs by the longer ones. On the basis of this previous work, one would expect the di-C_{16} chain phospholipid thiolate to be the predominant gold-bound species. Nevertheless, a similar thiolate exchange/substitution process may not be operative in the DSDPPC-Au system because a heterogeneous solid/gas, as opposed to solid/solution, reaction is involved here and there is no external reservoir of DSDPPC available for thiolate exchange. For this reason, the S2p spectrum may reflect contributions from both Au-SCH_3 and Au-SDPPC.

(20) Aliganga, A. K. A.; Duwez, A.-S.; Mittler, S. *Org. Electron.* **2006**, *7*, 337.

(21) 1 ML of Au was also evaporated on a DSDPPC monolayer transferred at higher surface pressure (32 mN m^{-1}). No significant difference in the extent of the surface reaction was observed: 62% bound thiolate (161.8 eV) and 38% unbound sulfur (163.3 eV).

(22) Service du répertoire toxicologique, Commission de la santé et de la sécurité du travail (CSST), Workplace Hazardous Materials Information System: http://www.reptox.csst.qc.ca/Produit.asp?no_produit=166371&nom=Dimethyl+disulfide (accessed May 19, 2010).

(23) At a film transfer pressure of 20 mN m^{-1}, DSDPPC occupies a molecular area of 0.50 ± 0.03 nm^{-2}, so that the surface concentration of -SS- groups in the monolayer is 2.0 ± 0.1 nm^{-2}. The surface coverage of Au atoms in 1 ML is 15.4 nm^{-2}, yielding a mean Au:S ratio of 3.8:1.

(24) Luedtke, W. D.; Landman, U. *J. Phys. Chem.* **1996**, *100*, 13323.

(25) Srinivasan, C.; Mullen, T. J.; Hohman, J. N.; Anderson, M. E.; Dameron, A. A.; Andrews, A. M.; Dickey, E. C.; Horn, M. W.; Weiss, P. S. *ACS Nano* **2007**, *1*, 191.

(26) Bittermann, A. G.; Jacobi, S.; Chi, L. F.; Fuchs, H.; Reichelt, R. *Langmuir* **2001**, *17*, 1872.

(27) There is no evidence that the Au atoms penetrate through the more liquid-like DLPC phase and accumulate on top of the solid-like DPPC domains.

(28) Badia, A.; Moraille, P.; Tang, N. Y. W.; Randlett, M.-E. *Int. J. Nanotechnol.* **2008**, *5*, 1371.

(29) Moraille, P.; Badia, A. *Langmuir* **2003**, *19*, 8041.

(30) Rinia, H. A.; Snel, M. M. E.; van der Eerden, J. P. J. M.; de Kruijff, B. *FEBS Lett.* **2001**, *501*, 92.

(31) Spatz, J. P.; Eibeck, P.; Mößmer, S.; Möller, M.; Herzog, T.; Ziemann, P. *Adv. Mater.* **1998**, *10*, 849.

(32) Chen, X.; Lenhert, S.; Hirtz, M.; Lu, N.; Fuchs, H.; Chi, L. *Acc. Chem. Res.* **2007**, *40*, 393.

(33) Gleiche, M.; Chi, L.; Gedig, E.; Fuchs, H. *ChemPhysChem* **2001**, *2*, 187.

(34) Berger, C. E. H.; van der Werf, K. O.; Kooyman, R. P. H.; de Grooth, B. G.; Greve, J. *Langmuir* **1995**, *11*, 4188.

(35) Chai, J.; Buriak, J. M. *ACS Nano* **2008**, *2*, 489.

(36) Xu, Q.; Bao, J.; Capasso, F.; Whitesides, G. M. *Angew. Chem., Int. Ed.* **2006**, *45*, 3631.

(37) Winter, C.; Weckenmann, U.; Fischer, R. A.; Kashammer, J.; Scheumann, V.; Mittler, S. *Chem. Vap. Depos.* **2000**, *6*, 199.

(38) Aliganga, A. K. A.; Wang, Z.; Mittler, S. *J. Phys. Chem. B* **2004**, *108*, 10949.

(39) Lu, P.; Demirkan, K.; Opila, R. L.; Walker, A. V. *J. Phys. Chem. C* **2008**, *112*, 2091.

(40) Minelli, C.; Hinderling, C.; Heinzelmann, H.; Pugin, R.; Liley, M. *Langmuir* **2005**, *21*, 7080.

Chapter 6 General Conclusions and Suggestions for Future Work

6.1 General Conclusions

This PhD thesis had the following objectives:

(i) improve the stripe pattern regularity in terms of the uniformity of the stripe width and spacing and identify the experimental parameters that control the stripe width,

(ii) generate chemically heterogeneous stripe patterns, and

(iii) template the deposition of metals onto the chemically heterogeneous stripe patterns to produce metallic nanostructures.

Limited control over the pattern features was achieved by varying the lipid composition, surface pressure at which the monolayer film was transferred from the A/W interface to solid substrates, and the substrate withdrawal speed. By varying the experimental conditions, five different morphologies were obtained: films of only broken stripes, broken stripes with vertical channels, a mixture of broken and continuous lines, mainly continuous lines, and micrometer-size domains coexisting with lines and/or broken lines (Figure 6.1). Two parameters seem to affect the stripe pattern. First, the optimal size of condensed domains to seems to be about 20 μm in diameter. The domain size can be varied using different χ_{DPPC} or by transferring the film at different surface pressures. Second, the film transfer speed will greatly affect the morphology of stripe pattern. Film collected at 1 mm min^{-1} results in stripes wider than films collected at speeds of 20 mm min^{-1}.

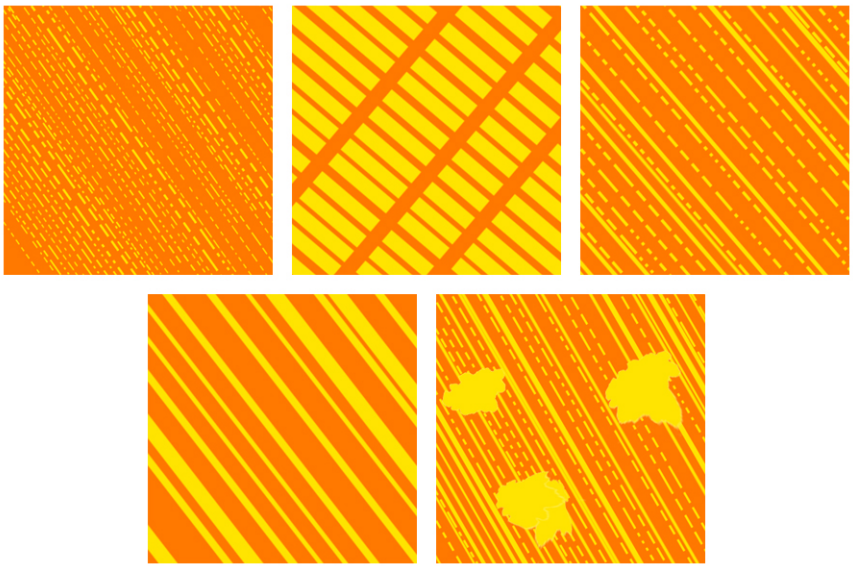

Figure 6.1 Schematic representation of the film morphologies obtained by the LB transfer of a DPPC/DLPC monolayer under different experimental conditions.

In each type of morphology, a significant variation in the feature dimensions remains. These type of nanostructured patterns do not have the perfection required for applications in the semiconductor industry but could be useful for proof-of-concept studies or the study of fundamental molecular interactions at the nanoscale. For example, alignment and elongation of biomolecules can occur on nanopatterned surfaces.[1,2]

DPPC/DLPC nanostructured films are only physically differentiated. To extend the templating possibilities of the pattern, DSDPPC and DSDLPC were chosen as modified lipid analogues to generate chemically differentiated mixed monolayers. The stripe pattern strongly depends on the phase properties of the lipid used in the binary mixture. DSDPPC has a methyldisulfide group tagged at the end of one of its alkyl chains, making the chains asymmetric. The presence of this bulkier $–SSCH_3$ group affects the physical properties and

interfacial behaviour of DSDPPC compared to DPPC. DSDPPC MLVs have a T_m higher than that of DPPC. Higher T_m values reflect a higher stability of the aggregates suggesting that the additional -$SSCH_3$ group promote favorable interactions. At the A/W interface, the modified lipids (DSDPPC and DSDLPC) are in a more expanded state, but have similar phase properties than their unmodified counterparts: DSDPPC undergoes a LE-C phase transition and DSDLPC remains in a fluid state. DSDPPC is significantly different from DPPC in two respects: its ability to form a homogeneous condensed phase film and its collapse behaviour. Liquid expanded and condensed phase coexistence in DSDPPC monolayers persists from the onset of the LE-C surface pressure transition until the film collapse. The collapse of the DSDPPC monolayer occurs at a lower surface pressure than that of DPPC. After the collapse, as the barriers continue the film compression, the surface pressure of the film keeps increasing; suggesting that the aggregates formed during the collapse remain associated to the monolayer and contribute to the increase in surface pressure.

Films of the modified and unmodified lipids were transferred onto Si/SiO_x to determine their respective film thicknesses by ellipsometry. It was difficult to obtain the film thickness of a DSDPPC monolayer in the condensed state because either there is liquid-expanded phase remaining (underestimated film thickness measured at 18 mN m^{-1}) or multilayer aggregates are present (overestimated film thickness above film collapse). AFM imaging of the DSDPPC aggregates, formed due to buckling of the film at pressures higher than that of film collapse, showed stacked monolayers of 3 nm thickness.

The deposition of DSDPPC films on gold was also achieved using the LB technique, forming a covalently bound film. XPS analysis revealed the characteristic S2p peak at a BE of 162.5 eV of gold-thiolate species. Gold-supported DSDPPC films were also formed by self-assembly from solution and characterized by reductive electrochemical desorption. The presence of a gold-thiolate species is confirmed by a single desorption peak at E = -1.08 V. Contrary to alkylthiols, DSDPPC did not readsorb during the anodic segment, suggesting that DSDPPC may form soluble aggregates that diffuse away from the electrode.

DSDPPC and DSDLPC were then mixed with unmodified lipids to form chemically differentiated monolayer patterns. DPPC/DSDLPC monolayers exhibit very similar phase morphology to that of DPPC/DLPC at the A/W interface. The appearance of DPPC-rich domains occurs at surface pressures around 16 to 18 mN m^{-1}, and these condensed domains reach a maximum size of about 30 μm in diameter. At high surface pressures (i.e., above 40 mN m^{-1}), DPPC remixes into the DLPC- or DSDLPC-rich fluid phase due to a reduced interfacial line tension. On the other hand, DSDPPC/DLPC monolayers exhibit large flower-like domains (70 μm in diameter) with a dendritic tendency and do not remix with DLPC at high surface pressures. Regardless of these differences in the condensed domain structures between DPPC/DLPC and DSDPPC/DLPC equimolar mixtures, a pattern of parallel lines was obtained by LB deposition for DSDPPC/DLPC. Mica or Si/SiO_x could be used as a substrate onto which a pattern of stripes is deposited via the LB technique. The use of Si/SiO_x, a semi-conductor, expands the repertoire of techniques that can be used to characterize the phospholipid films.

Thermally evaporated gold selectively deposits on the methyldisulfide-terminated stripes or background matrix, through a Au-S interaction which was characterized by XPS. A saturated Au coverage of the stripes is reached at an evaporated film thickness of *ca*. 0.1 nm (0.28 ML) and selectivity is lost at thicknesses > 0.1 nm. Thermal evaporation of silver and copper also results in the preferential deposition of metal on the methyldisulfide-terminated regions of the pattern.

The metal layer (0.52 ML) that selectively deposits onto the stripes or background matrix is too thin to be used in applications such as plasmon optics and electronic transport because these require thicker deposits of continuous metal nanostructures.[3-6] In our quest to characterize and spatially localize this very thin metal layer, it quickly became clear that it is very difficult to perform chemical mapping of nanostructures using current surface analytical techniques. Very few analytical instruments, such as a nano SIMS,[7] can provide such information. In the push towards miniaturization, there is a definite need for the

development of new or improved surface analytical tools that are capable of resolving nanostructures that are submonolayer to one monolayer thick.

6.2 Suggestions for Continued Research

To increase the thickness of the metal layer that can be deposited onto the disulfide-modified patterns, OMCVD of an organometallic precursor could be used. Winter *et al.*[8] were able to perform OMCVD of methyl(trimethylphosphine)gold(I) $[(CH_3)_3P]AuCH_3$, onto micropatterns of ω-functionalized alkylthiols and a metal layer thickness of at least 30 nm could be obtained without loss of selectivity. $[(CH_3)_3P]AuCH_3$, is a volatile organic compound that decomposes at a temperature (70 °C) that is compatible with our lipid films. To increase the thickness of the selectively deposited gold layer on our stripe patterns, OMCVD of $[(CH_3)_3P]AuCH_3$ should be attempted.[8]

Other types of patterns can be investigated with these amphiphilic thiolipids. It has been demonstrated that mixtures of DSPC/DLPC completely phase separate into a morphology of circular DSPC condensed domains.[9] DSDLPC, the C12 modified lipid could be used in place of the DLPC. Using LS film deposition on gold, the surrounding DSDLPC matrix would be covalently bound to the surface and physisorbed DSPC could simply be washed off, followed by a backfill using an alkylthiol (Scheme 6.1). LS deposition of amphiphilic thiols would be an alternative to microcontact printing.

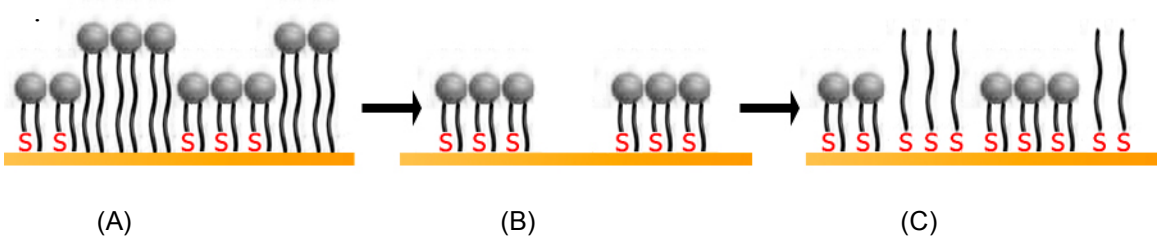

Scheme 6.1 Schematic representation of (A) a phase separated mixture of unmodified and functionalized phospholipid films transferred by LS onto gold, (B) a monomolecular film after selective removal of the physisorbed lipids, and (C) a chemically heretogeneous pattern of a covalently bound film after back-filling with an alkanethiol.

A popular methodology for the synthesis of stable metal nanoparticles involves capping the nanoparticle surface with a monolayer of alkylthiol. Monolayer-protected nanoparticles are of interest in many applications, but the challenge lies in rendering these biocompatible and water-soluble. DSDPPC-protected nanoparticles would be water soluble and biocompatible due to the phosphocholine head group.[10-12]

Lipids modified with a methyldisulfide at the end of one of their alkyl chains open endless possibilities in terms of surface modification. Owing to its disulfide functional group, the lipid can form a stable covalent bond with metals. It has been demonstrated in this thesis that DSDPPC behaves like alkylthiols and alkyldisulfides, since it can form SAMs on gold through a gold-thiolate bond. DSDPPC can be viewed as an alkyldisulfide with a phosphocholine terminal group. This phosphocholine head group is very interesting because it is where enzymatic reactions occur in lipid bilayers. DSDPPC monolayers covalently bound to gold provide a stable platform to study enzymatic reactions. Enzymes

are also incredible molecules capable of performing chemical reactions under mild conditions at high specificity. PLD (phospholipase D) could be used to modify only the DSDPPC domains.[13,14]

The development of nanoscale structures requires the continual investigation of molecules capable of self-assembly. These studies are an integral part of this pivotal "small revolution" of today's generation.

6.3 References

(1) Johansson, F.; Carlberg, P.; Danielsen, N.; Montelius, L.; Kanje, M. *Biomaterials* **2006**, *27*, 1251.

(2) Yim, E. K. F.; Reano, R. M.; Pang, S. W.; Yee, A. F.; Chen, C. S.; Leonga, K. W. *Biomaterials* **2005**, *26*, 5405.

(3) Stewart, M. E.; Anderton, C. R.; Thompson, L. B.; Maria, J.; Gray, S. K.; Rogers, J. A.; Nuzzo, R. G. *Chem. Rev.* **2008**, *108*, 494.

(4) Chai, J.; Buriak, J. M. *ACS Nano* **2008**, *2*, 489.

(5) Chai, J.; Wang, D.; Fan, X.; Buriak, J. M. *Nature Nanotechnol.* **2007**, *2*, 500.

(6) Xu, Q.; Bao, J.; Capasso, F.; Whitesides, G. M. *Angew. Chem., Int. Ed.* **2006**, *45*, 3631.

(7) Boxer, S. G.; Kraft, M. L.; Weber, P. K. *Annu. Rev. Biophys.* **2009**, *38*, 53.

(8) Winter, C.; Weckenmann, U.; Fischer, R. A.; Kashammer, J.; Scheumann, V.; Mittler, S. *Chem. Vap. Depos.* **2000**, *6*, 199.

(9) Sanchez, J.; Badia, A. *Chem. Phys. Lipids* **2008**, *152*, 24.

(10) Murphy, C. J.; Gole, A. M.; Stone, J. W.; Sisco, P. N.; Alkilany, A. M.; Goldsmith, E. C.; Baxter, S. C. *Acc. Chem. Res.* **2008**, *41*, 1721.

(11) Templeton, A. C.; Wuelfing, W. P.; Murray, R. W. *Acc. Chem. Res.* **2000**, *33*, 27.

(12) Daniel, M.-C.; Astruc, D. *Chem. Rev.* **2004**, *104*, 293.

(13) Ulbrich-Hofmann, R. *Eur. J. Lipid Sci. Technol.* **2003**, *105*, 305.

(14) Dippe, M.; Mrestani-Klaus, C.; Schierhorn, A.; Ulbrich-Hofmann, R. *Chem. Phys. Lipids* **2008**, *152*, 71.